Applied Computational Electromagnetics Society

Journal

July 2011 Vol. 26 No. 7

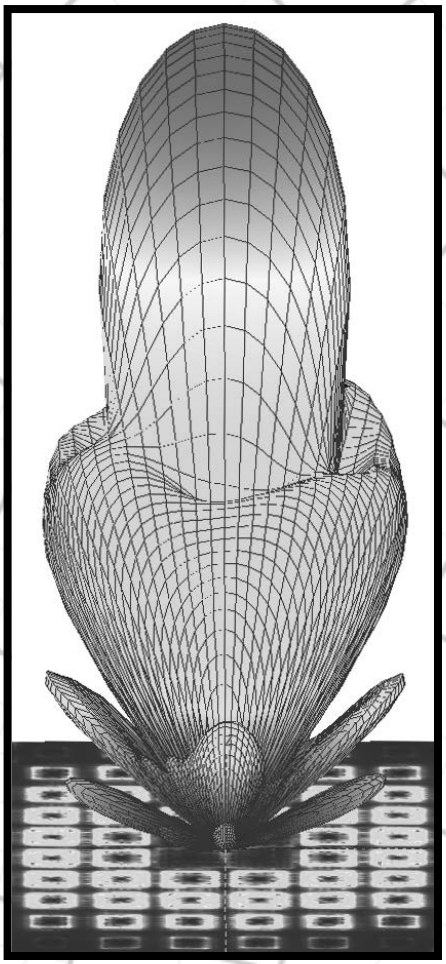

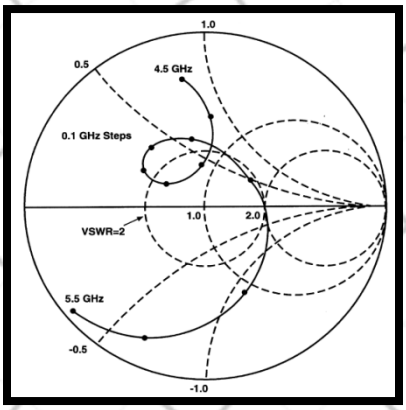

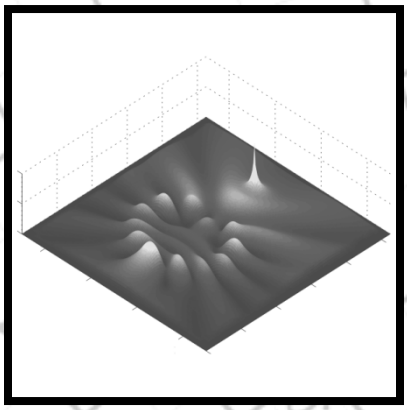

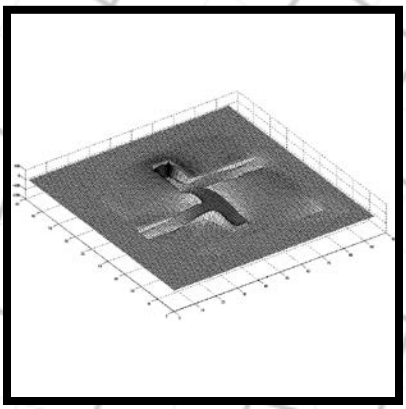

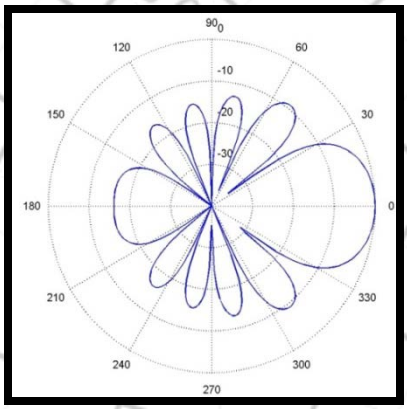

ISSN 1054-4887

GENERAL PURPOSE AND SCOPE: The Applied Computational Electromagnetics Society ***(ACES)*** Journal hereinafter known as the ***ACES Journal*** is devoted to the exchange of information in computational electromagnetics, to the advancement of the state-of-the art, and the promotion of related technical activities. The primary objective of the information exchange is to inform the scientific community on the developments of new computational electromagnetics tools and their use in electrical engineering, physics, or related areas. The technical activities promoted by this publication include code validation, performance analysis, and input/output standardization; code or technique optimization and error minimization; innovations in solution technique or in data input/output; identification of new applications for electromagnetics modeling codes and techniques; integration of computational electromagnetics techniques with new computer architectures; and correlation of computational parameters with physical mechanisms.

SUBMISSIONS: The ***ACES Journal*** welcomes original, previously unpublished papers, relating to applied computational electromagnetics. Typical papers will represent the computational electromagnetics aspects of research in electrical engineering, physics, or related disciplines. However, papers which represent research in applied computational electromagnetics itself are equally acceptable.

Manuscripts are to be submitted through the upload system of ***ACES*** web site http://aces.ee.olemiss.edu See "Information for Authors" on inside of back cover and at ***ACES*** web site. For additional information contact the Editor-in-Chief:

Dr. Atef Elsherbeni
Department of Electrical Engineering
The University of Mississippi
University, MS 386377 USA
Phone: 662-915-5382
Email: atef@olemiss.edu

SUBSCRIPTIONS: All members of the Applied Computational Electromagnetics Society are entitled to access and download the ***ACES Journal*** any published journal article available at http://aces.ee.olemiss.edu. Printed issues of the ***ACES Journal*** are delivered to institutional members. Each author of published papers receives a printed issue of the ***ACES Journal*** in which the paper is published.

Back issues, when available, are $50 each. Subscription to ***ACES*** is through the web site. Orders for back issues of the ***ACES Journal*** and change of address requests should be sent directly to ***ACES*** office at:

Department of Electrical Engineering
The University of Mississippi
University, MS 386377 USA
Phone: 662-915-7231
Email: aglisson@olemiss.edu

Allow four weeks advance notice for change of address. Claims for missing issues will not be honored because of insufficient notice, or address change, or loss in the mail unless the ***ACES*** office is notified within 60 days for USA and Canadian subscribers, or 90 days for subscribers in other countries, from the last day of the month of publication. For information regarding reprints of individual papers or other materials, see "Information for Authors".

LIABILITY. Neither ***ACES***, nor the ***ACES Journal*** editors, are responsible for any consequence of misinformation or claims, express or implied, in any published material in an ***ACES Journal*** issue. This also applies to advertising, for which only camera-ready copies are accepted. Authors are responsible for information contained in their papers. If any material submitted for publication includes material which has already been published elsewhere, it is the author's responsibility to obtain written permission to reproduce such material.

APPLIED COMPUTATIONAL ELECTROMAGNETICS SOCIETY JOURNAL

July 2011
Vol. 26 No. 7
ISSN 1054-4887

The ACES Journal is abstracted in INSPEC, in Engineering Index, DTIC, Science Citation Index Expanded, the Research Alert, and to Current Contents/Engineering, Computing & Technology.

The illustrations on the front cover have been obtained from the research groups at the Department of Electrical Engineering, The University of Mississippi.

JULY 2011 REVIEWERS

Ahmed Abdelrahman
Mohamed Abouzahra
Manuel Arrebola
Guido Ala
Mohamed Bakr
Rajeev Bansal
Sami Barmada
Adalbert Beyer
William Coburn
Veysel Demir
Yiming Deng
Alistar Duffy
Atef Elsherbeni
Ali Farahbakhsh
Mario Fernandez
Christophe Fumeaux
Peng Gao
Josefa Gomez
Tuan-Yung Han
Mousa Hussein
Shambhu Jha
Nikolaos Kantartzis
Ozlem Kilic
Senthil Kumaran
Mun Soo Lee
Angelo Liseno
Haixin Liu
Giampiero Lovat
Alexei Maradudin
Anthony Martin
Zahera Mekkioui
M. Mouloud
Ivor Morrow
Yoginder Negi
Tao Peng
Andrew Peterson
Jeffrey Pursel
Vince Rodriguez
Usman Saeed
Antonio Espirito Santo
Harvey Schuman
Laura Smith
Ren Sheng Sun
Yuan Sun
Fikret Tokan
Theodoros Tsiboukis
Yasuhiro Tsunemitsu
Ahmet Turk
Hui Wang
Rui Wang
Su Yan

THE APPLIED COMPUTATIONAL ELECTROMAGNETICS SOCIETY

JOURNAL

Vol. 26 No. 7 July 2011

TABLE OF CONTENTS

A Wideband U-Slot Loaded Modified E-Shape Microstrip Patch Antenna and Frequency Agile Behavior by Employing Different Height Ground Plane and Ribbon Type Switches

Rahul Bakshi and Satish K. Sharma

Department of Electrical and Computer Engineering
San Diego State University, 5500 Campanile Drive
San Diego, CA, USA, 92182-1309
rahulbakshi1984@gmail.com, ssharma@mail.sdsu.edu

Abstract ─ This paper presents investigation results on a wideband U-slot loaded modified E-shape (USLMES) microstrip patch antenna with frequency agile behavior by employing different height ground plane and ribbon type copper switches. The USLMES patch is excited using the notch feed mechanism by a 50 Ω coaxial probe outside the patch surface so that coaxial probe does not contribute significantly to the peak-cross-polarization levels. The parametric study results are presented for the wideband patch antenna design and important parameters have been noted. The proposed wideband patch antenna offers impedance (S_{11} = −10 dB) and 3dB gain bandwidths of at least 35% (3.09GHz to 4.42GHz) with stable radiation patterns and acceptable cross-polarization levels. The effect of ground plane height variation not only alters operating frequency, but also, Gain and impedance bandwidth. Frequency agility is also achieved from 3.02GHz to 4.95 GHz by turning different combination of switches ON/OFF. The prototype antennas were fabricated and experimentally verified for both wideband patch performance and frequency agility by implementing different ground plane heights. The simulated performance is in reasonable agreement with the measured results.

Index Terms ─ Frequency agile behavior, ground plane height, ribbon type switches, USLMES microstrip patch, wideband antenna.

I. INTRODUCTION

With the increasing growth of modern wireless communication systems, wide usage of resources and hardware implementation on circuit board has become imperative. This has put challenging demands on the antenna designs. In this context, much attention has been given to the frequency agile or frequency reconfigurable patch antennas because they offer multiband and wideband operations, while keeping the antenna radiation pattern almost invariant. Reconfigurable antennas have been designed by incorporating switching components like PIN diodes switches [1-3], RF-MEMS switches [4-6] and varactor diodes [7] on the antenna's geometry. In most of the above, it is seen that placement of a number of switches on the antenna radiating edges deteriorates its performance. Moreover biasing of the loaded diodes between the patch and ground plane requires complex circuitry which limits the freedom of reconfiguration to a few percent. The frequency reconfiguration based on the ON/OFF states of the switches/diodes, also, limits reconfigurable states to one or two discreet frequencies [7]. Therefore, the need for a wideband response to the frequency reconfiguration or agility is very much desirable.

Ground plane reconfiguration has been studied in [8-10] and offers a simple frequency detuning technique as compared to the above. It avoids complex circuitry, biasing of external components and operates on the inherent characteristics of the patch itself. Frequency agility is achieved by altering the height of the ground plane, but this requires high levels of electrostatic actuation to

Submitted On: June 20, 2010
Accepted On: August 23, 2010

vary the ground plane height. The limitations are repeatability, very limited ground plane height variation and complex fabrication of the reconfigurable ground plane structures. Techniques such as, U-slot loaded patch [11, 12], impedance matching network based patch [13], E-

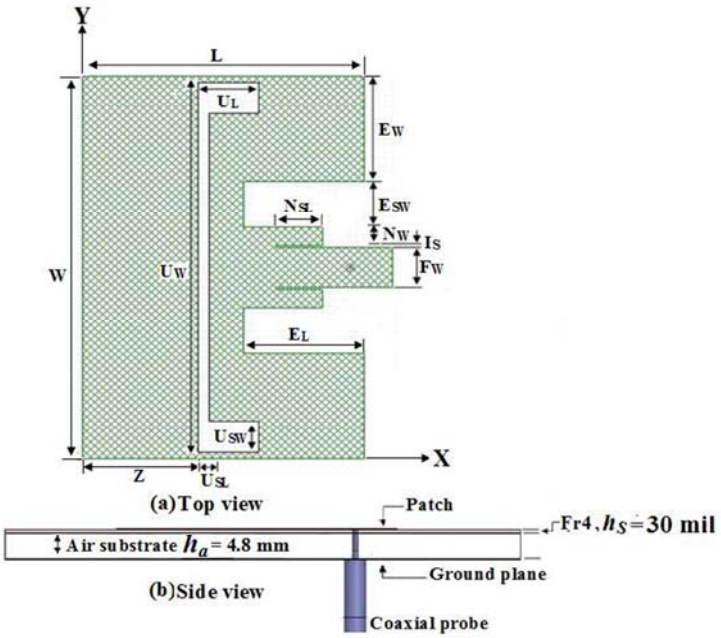

Fig. 1. Geometry of a U-slot loaded modified E-shape (USLMES) wideband patch antenna. (a) Top view, and (b) side view. Final patch design parameters based on the parametric study are: L = 40mm, W = 60mm, E_W =16.6mm, E_L = 17.2mm, E_{SW} = 7.2mm, N_W = 2.9mm, I_S = 0.2mm, N_{SL} = 6.5mm, F_W = 6.2mm, F_P = 6mm, U_W= 58mm, U_L= 8.6mm, U_{SW} = 5mm, h_a = 4.8mm, h_S = 0.761 mm.

shape patch antennas [14, 15] and multi-layer stacked structures [16] have been investigated to increase the impedance bandwidth of the microstrip patch antenna. The U-slot loaded patch antenna presented in [11] has impedance bandwidth around 30%. The E-shape patch investigated in [14], also, offers around 30% bandwidth which uses coaxial probe feeding. Another E-shape patch investigated in [15] offers 19.5% bandwidth with transmission line feed.

However, here in this paper, we present investigation results on the effect of employing variable height ground plane and copper ribbon switches on the frequency agile behavior of a proposed wideband U-slot loaded modified E-shape (USLMES) microstrip patch antenna. The proposed antenna offers an impedance bandwidth of at least 35% with relatively smaller ground plane. Further, care has been taken to include the coaxial probe outside the patch area to avoid high cross-polarization generation due to the coaxial probe. The patch is printed on a low cost FR-4 substrate which is a real microwave substrate hence soldering of the coaxial probe is easier than when done on a foam substrate. Between the patch substrate layer and the ground plane lies different thicknesses of the foam substrate. The U-slot loaded modified E-shape (USLMES) microstrip patch antenna was designed first using Ansoft Designer ver 3.5 with infinite ground plane and later on optimized as 3D finite structure including ground plane and substrate size using the Ansoft HFSS ver. 11.0 and CST's Microwave Studio ver. 2009 [17-18].

II. U-SLOT LOADED MODIFIED E-SHAPE PATCH ANTENNA

A. Antenna geometry

The geometry of the proposed USLMES notch fed patch on a microwave substrate FR-4 (ε_r =4.4, tan δ =0.02) of thickness h_s = 0.761 mm placed on a foam substrate (ε_r =1.06) of thickness h_a = 4.8mm excited by a notch fed through a 50Ω coaxial probe is shown in Fig. 1. The microwave substrate FR-4 is employed for ease of fabrication and SMA soldering to the patch surface.

The imperative parameters which were optimized extensively to bring matching level with respect to S_{11} <−10dB are E-shape patch wings width (E_W), length of the E-wing (E_L), E-slot width (E_{SW}), notch width (N_W), inset slot width (I_S), feed width (F_W), U-slot width (U_W), U-slot wing width (U_{SW}) and U-slot length (U_{SL}).

A thorough parametric study was conducted to attain optimized values for the design parameters. The USLMES shows a wideband response from 3.09GHz to 4.42GHz (operating bandwidth) exhibiting 35.41% impedance bandwidth with final achieved values.

B. Parametric study results

To understand the effect of USLMES patch antenna parameters on its impedance bandwidth, individual design parameter are varied, one at a time, or a set of parameters, while keeping all other parameters invariant. The simulations were generated using the Ansoft Designer and are shown in Fig. 2(a-h). Ansoft Designer models infinite substrate while ground plane can be of finite size. For all the simulation, impedance bandwidth is defined for S_{11} = −10dB.

i. Fig. 2(a) shows the effect of varying the U-slot edge distance (Z) to the USLMES edge. The distance Z is varied from 11.4mm to 16.4mm. At Z= 11.4mm, the USLMES shows dual band response with first band operating in 3.05GHz to 3.2GHz (4.80% bandwidth) and second in 3.90GHz to 4.35GHz (10.90% bandwidth). A further increase of distance to Z=12.4mm shows dual band response from 3.05GHz to 3.25GHz (6.34% bandwidth) and 3.80GHz to 4.37GHz (13.95% bandwidth). At distance Z=16.4mm, the USLMES shows a wideband response from 3.09GHz to 4.42GHz exhibiting 35.41% impedance bandwidth.

ii. Fig. 2(b) shows the effect of varying U-slot width U_W from 46mm to 58mm. At width U_W = 46mm, the USLMES shows dual band response with first band operating in 2.90GHz to 3.18GHz (9.21% bandwidth) and second in 3.75GHz to 4.52GHz (18.62% bandwidth). Increasing U-slot width to U_W = 50mm again shows dual band response with decrease in first band bandwidth (3.0GHz to 3.25GHz, 8% bandwidth) and increase in second band bandwidth (3.65GHz to 4.48GHz, 20.41% bandwidth). A further increase in slot width to U_W = 56mm shows a wideband performance (3.08GHz to 4.43GHz, 35.91% bandwidth) but touches the S_{11}= −10dB line near 3.5GHz. Therefore on further investigation, U-slot width of U_W = 58mm is selected showing wideband response (3.09GHz to 4.42GHz, 35.41% bandwidth).

iii. The effect of varying the U-slot wing width is shown in Fig. 2(c). The U-slot wing width U_{SW} is varied from 3mm to 8mm. It is seen to exhibit dual band response at U_{SW} = 8mm starting 3.02GHz to 3.3GHz (8.86% bandwidth) and 3.6GHz to 4.45 GHz (21.11% bandwidth). With further decrease in U-slot wing width to U_{SW} = 7 mm, USLMES shows a wideband response from 3.05GHz to 4.43GHz (36% bandwidth) but is seen touching the S_{11}= −10dB line at 3.5GHz. The above problem is rectified at U-slot wing width U_{SW} = 5mm offering band operating in 3.09GHz to 4.42GHz (35.41% bandwidth) with better bandwidth performance at U_{SW} = 3mm (34.89%) also.

iv. Fig. 2(d) shows the effect of varying the U-slot length U_{SL} from 2.0mm to 1.6mm. By varying the U-slot length U_{SL}, the bandwidth increases from 33.65% (3.2GHz to 4.50GHz) to 35.41% (3.09GHz to 4.42GHz).

v. Fig. 2(e) shows the effect of varying the USLMES patch wings width E_W and notch width N_W. While investigating the above two parameters, the E_{SW} is kept constant at 7.2mm. Therefore E_W is varied from E_W = 14mm to 16.6mm and N_W from 5.5mm to 2.9mm. At E_W = 14mm, N_W = 5.5mm, USLMES excites higher order modes at higher frequency, therefore on further increasing wing width E_W = 16.6mm and reducing N_W to 5.5mm, a wideband response is seen operating in 3.09GHz to 4.42GHz (35.41% bandwidth).

vi. Fig. 2(f) shows the effect of varying the feed width F_W and inset slot width I_S from 5.2mm to 6.2mm and 0.70mm to 0.20mm, respectively. The USLMES shows dual band response at F_W = 5.2mm, I_S = 0.70mm operating in 3.08GHz to 3.18GHz (3.50%

bandwidth) and 3.6GHz to 4.55GHz (23.31% bandwidth). USLMES continues to show dual band response at F_W = 5.4mm, I_S = 0.6mm operating in 3.08GHz to 3.19GHz (3.50% bandwidth) and 3.58GHz to 4.53GHz (23.42% bandwidth). Further increasing feed width F_W to 6.2mm and reducing inset slot width I_S to 0.2mm, wideband response is achieved operating in 3.09GHz to 4.42GHz (35.41% bandwidth).

vii. The effect of varying the USLMES patch length E_L from 16mm to 18 mm is shown in Fig. 2(g). The impedance bandwidth increases from 31.96% (3.18GHz to 4.39GHz) at E_L = 16mm to 33.82% (3.12GHz to 4.39GHz) at E_L= 16.4mm. A further increase of USLMES wing length to E_L= 17.2 mm increases the impedance bandwidth to 35.41% (3.09GHz to 4.42GHz) which is better than impedance bandwidth of 34.41% (3.08GHz to 4.36GHz) at E_L= 18mm. Therefore E_L = 17.2 mm is the best value for the bandwidth of the proposed USLMES.

viii. Fig. 2(h) shows the effect of varying the finite ground plane size for S_{11} = −10dB. The dual band response at G = 65×65mm^2 operating in 3.02GHz to 3.30GHz (8.86% bandwidth) and 3.6GHz to 4.43GHz (20.67% bandwidth) is optimized to wideband response at G = 100 ×120 mm^2 operating in 3.09GHz to 4.42GHz (35.41% bandwidth).

Table 1: Final USLMES patch design parameters

PARAMETERS	VALUES
USLMES wings width, E_W	16.6 mm
USLMES wings length, E_L	17.2 mm
Notch width, N_W	2.9 mm
Inset slot width, I_S	0.2 mm
Inset slot length, N_{SL}	6.5 mm
Feed width, F_W	6.2 mm
U-Slot length, U_{SL}	1.6 mm
U-Slot distance to USLMES patch edge (Z)	16.4 mm
U-Slot Width , U_W	58 mm
U-Slot wing width , U_{SW}	5.0 mm
Ground plane (X×Y mm^2)	100×120 mm^2

The other design parameters did not show any significant effect on the impedance bandwidth and are kept unchanged throughout the parametric study. Table 1 shows the design parameters of the final proposed USLMES patch antenna.

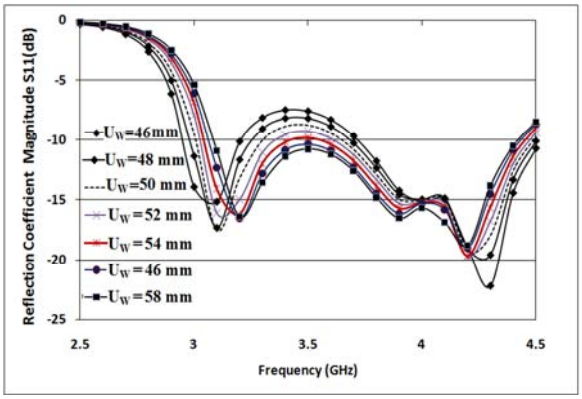

(a)

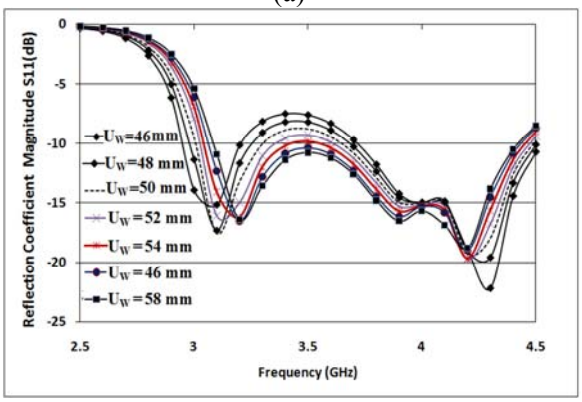

(b)

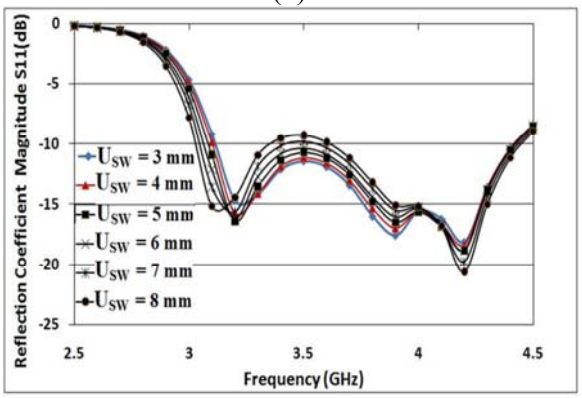

(c)

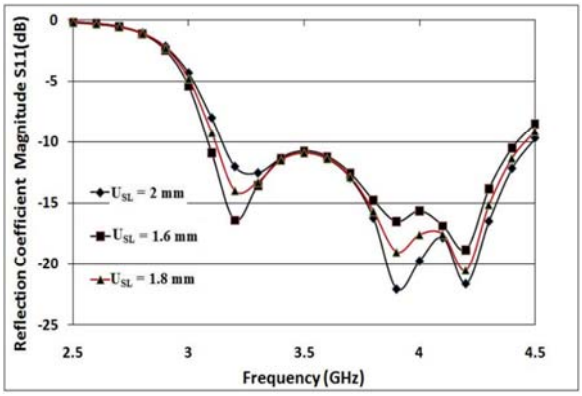

(d)

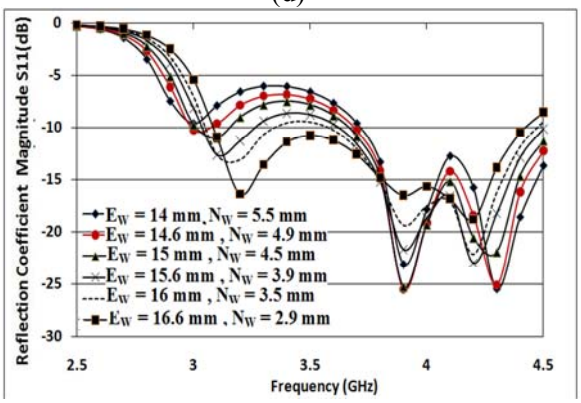

(e)

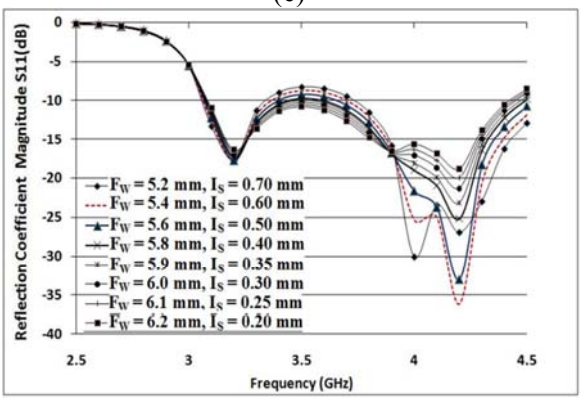

(f)

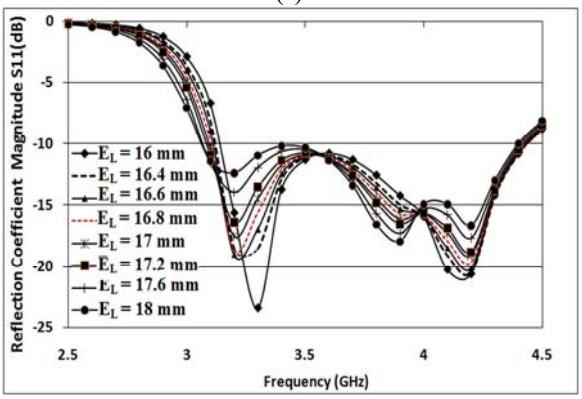

(g)

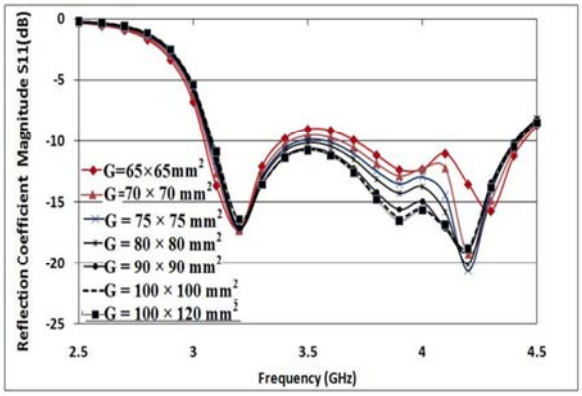

(h)

Fig. 2. Effect of different USLMES parameters on its reflection coefficient (S_{11}) performance while keeping other parameters constant. (a) Z, (b) U_W, (c) U_{SW}, (d) U_{SL}, (e) E_W and N_W, (f) F_W and I_S, (g) E_L, (h) G.

III. FREQUENCY AGILE BEHAVIOR OF PROPOSED WIDEBAND PATCH

A. Ground plane height variation

The simulation results for this part of the study were generated using the Ansoft Corporation's finite element method (FEM) based on the high frequency structure simulator (HFSS) which models all finite dimensions including the substrate and ground plane. The simulation considers interaction of SMA placement close to the antenna, which in this case is outside of the patch.

Figure 3 shows the simulation results for the USLMES when investigated for different air-gap heights between the FR-4 substrate and the ground plane. The structure initially operates (w.r.t. S_{11} = −10dB) at 4.2GHz at h_a = 2.8mm height. With the increase in air-gap height (h_a) to 3.2mm, the frequency shifts to the lower end and operates at 3.4 GHz showing dual band performance with the first band operating in 3.26GHz to 3.6GHz (9.91% BW) and the second band operating in 3.91GHz to 4.34GHz (10.42% BW). As the height h_a is increased further to 4.8mm, the frequency shifts more towards the lower end and operates as wideband antenna achieving 35% bandwidth (3.09GHz to 4.40GHz). By further increase in height to 6.4mm, the lower end frequency shifts to 3.0GHz with operational bandwidth of 34.71% (3.0GHz to 4.26GHz). With further increasing the air-gap (h_a) to 7.8mm, the USLMES resonates

between 3.26GHz to 3.75GHz offering 13.98% impedance bandwidth. Thus, the effect of employing different height ground plane reinstates reconfigurable or frequency agile operational bands with single, dual and wideband responses.

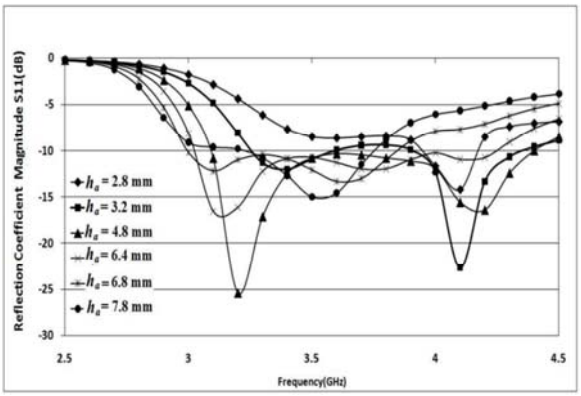

Fig. 3. Reflection coefficient S_{11} (dB) versus frequency (GHz) for the USLMES with different air-gap height variations.

Table 2 summarizes the effect of ground plane height variation on the frequency agile behavior of USLMES. Figure 4 shows the broadside gain at (θ=0^o) for the USLMES patch for different air-gap height variations. The gain remains above 5dBi throughout the operational band for all the cases. The best case from the air gap height study is the reference case with h_a = 4.8m, where the realized gain stays above 7dBi throughout the frequency bandwidth from 3.09GHz to 4.42GHz. A slight drop in gain at 4.4GHz is attributed to the increase in the cross-polarization level. It can, also, be seen that antenna possess wideband gain response even though it exhibited multiband or single wideband impedance matching response as shown in Fig. 3. Thus, the antenna can be reconfigured for a specific frequency range from 3GHz to 4.42GHz by employing a variable height ground plane. The mechanism to implement a variable height ground plane with the desired air-gap variation from 2.8mm to 7.8mm is a challenging task. This can be realized using the methods explored in [19-20], but comes at the price of complex fabrication and little air-gap variation which will not be sufficient. Therefore, at this point, electronic method for varying the ground plane has not been completed and will be the subject for future studies. However, to prove the finding, three different antennas with three different air-gaps were fabricated and experimentally tested.

Table 2: Frequency response for USLMES under different heights

S. No	Air Gap Heights (mm)	Percentage Bandwidth (%)	Band	Frequency of Operation (GHz)
1	2.8	4.43	single	3.92 –4.20
2	3.2	10.21, 12.30	dual	3.25−3.60, 3.89-4.40
3	4.8	35.41	wideband	3.09 –4.42
4	6.4	34.52	wideband	3.02 –4.28
5	6.8	25.32	wideband	3.00 −3.87
6	7.8	13.25	wideband	3.24 −3.70

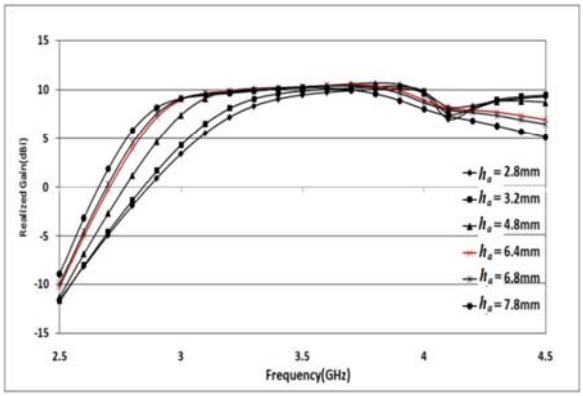

Fig. 4. Realized broadside gain (dBi) versus frequency (GHz) for the USLMES patch with different air-gap height variations.

B. Copper ribbon type switches

The reference USLMES presented above is modified further to incorporate switches. Two conductive arms are incorporated inside the E-patch slot width area to compensate switches of 1.8mm × 1.8mm dimensions. These are numbered as switch 4, switch 5, switch 6, and switch 7. All the USLMES parameters remain the same as mentioned in the previous section. Three switches are, also, incorporated inside the U-slot which is seen affecting the frequency reconfigurable characteristics of the USLMES under turning ON/OFF conditions. The other parameters of USLMES are the same as described in the previous section. The reference ULSMES has h_a = 4.8mm.

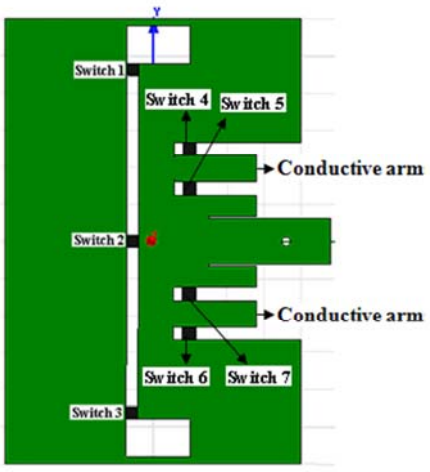

Fig. 5. Modified USLMES patch with copper type ribbon switches incorporation**.**

Figure 5 shows the modified geometry of USLMES with two conductive arms loaded with switches 4, 5, 6, and 7. The U-slot is, also, loaded with three switches 1, 2, and 3. The switches play an important role to change the resonant frequency according to different combinations of turning ON and OFF. Figure 6 shows the reflection coefficient magnitude of the reference USLMES with different combination of switches in operation. Initially all the switches 1, 2, 3, 4, 5, 6, and 7 are OFF (Case 1) and the USLMES shows impedance bandwidth of 8.86% with band operating in 3.02GHz to 3.3GHz. With the turning ON of the switches 1, 3, 4, 5, 6, and 7 (Case 2), the modified USLMES shows dual band performance with the first band operating in 3.3GHz to 3.55GHz (8.82% impedance bandwidth) and the second band operating in 3.85GHz to 4.65GHz (18.82% impedance bandwidth). At this point, the switches # 1 and # 3 are turned OFF and switch # 2 is turned ON with switches 4, 5, 6 and 7 (Case 3). The USLMES shows resonance below S_{11} = −10dB from 3.60GHz to 4.95GHz (31.57% impedance bandwidth). Thus, the combination of 7 switches incorporated on the geometry of modified USLMES contributes to operation in different frequency band and can be reconfigured for various applications between 3.02GHz to 4.95GHz. During the frequency reconfiguration, radiation properties almost remained similar to the original antenna, hence not included here for the sake of brevity.

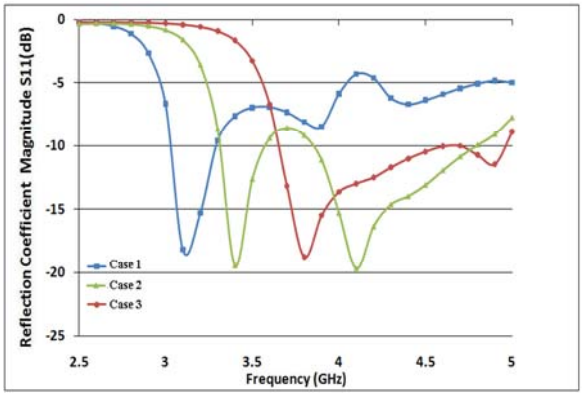

Fig. 6. Simulated reflection coefficient magnitude S_{11} (dB) versus frequency (GHz) for reference USLMES patch for different combination of switches turned ON/OFF.

IV. EXPERIMENTAL VERIFICATIONS

The U-slot loaded modified E-shape (USLMES) microstrip patch antenna was fabricated and measured for both wideband patch performance and frequency agility by implementing different ground plane heights in the Antenna and Microwave Lab at San Diego State University. The lab houses an Anritsu's vector network analyzer (model # 37269D), LPKF milling machine and anechoic chamber with the capability to measure both far-field and spherical near-field based radiation patterns. The copper ribbon switches based patch antennas (Case 1, Case 2, and Case 3) were not fabricated to avoid additional fabrication cost till the actual switch study is completed, which will be published at a later date.

Figure 7 shows the photograph of one of the fabricated patch antennas on FR-4 substrate of h_s = 0.761mm. This offers easy soldering of the coaxial probe with the patch than when antenna is directly etched on the foam substrate. Further, the coaxial probe is out of the patch surface, which helps in lowering the cross-polarization levels.

A. Frequency agile behavior verification

For the experimental verification purposes, three different USLMES patch prototypes were fabricated with air-gaps h_a = 3.2mm, 4.8mm and 6.4mm and tested using network analyzer. Their reflection coefficient results are shown in Fig. 8.

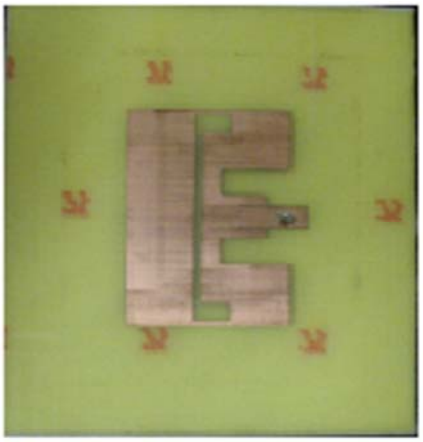

Fig. 7. Photograph of the U-slot loaded modified E-shape (USLMES) patch fabricated on FR-4 substrate of 0.761mm thickness.

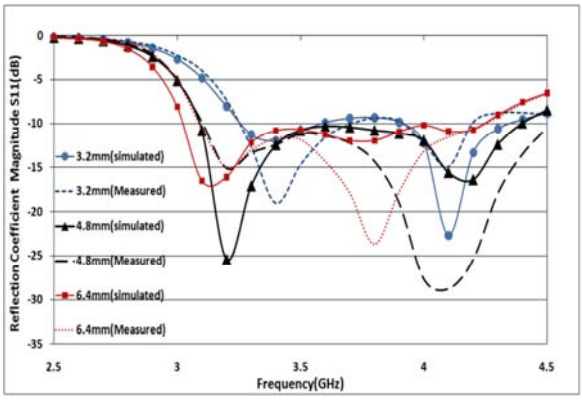

Fig. 8. Measured and simulated reflection coefficient magnitude S_{11} (dB) versus frequency (GHz) for three fabricated USLMES patches.

The simulated S_{11} for the USLMES patch with 3.2mm air-gap height shows dual band performance with the first band operating in 3.26GHz to 3.6GHz (9.91% bandwidth) and the second band operating in 3.91GHz to 4.34GHz (10.42% bandwidth). The measured S_{11} results show reasonable agreement with the first band operating in 3.26GHz to 3.71GHz (12.91% bandwidth) and the second band 3.91GHz to 4.2 GHz (7.15% bandwidth). The USLMES with 4.8mm (reference, Fig. 1(a-b)) air-gap height has simulated frequency band from 3.09 GHz to 4.42GHz offering 35% impedance bandwidth. In comparison to this, the measured S_{11} covers the above band and extends to 4.60GHz (38% bandwidth). The simulated S_{11} for the 6.4mm air-gap patch starts from 3.0GHz and ends at 4.26 GHz, whereas the measured S_{11} starts at 3.09GHz and ends at 4.26GHz offering 35% impedance bandwidth. Therefore, the simulated and measured S_{11} agree reasonably well over the operational frequency bands. Slight disagreement in the S_{11} for the three cases is attributed to the uneven foam surfaces between the FR-4 and the ground plane. In addition, the losses associated with the dielectric and the conductors are not generally considered accurately in simulations, hence offers slightly reduced matching bandwidth than the measured results. Finally, it can be seen that the ground plane height variation offers frequency agility over a wide bandwidth. Basically, an antenna with dual band with reasonable bandwidths and/or with single wideband can be realized based on the communication needs by ground plane height variation. As mentioned earlier, for real-time ground plane height variation providing the desired agility, one needs additional methods, however, by mechanical height variation; one can still get the frequency agility.

B. Wideband USLMES patch antenna

The proposed USLMES wideband patch antenna with h_a = 4.8mm was, also, tested for its radiation patterns and gain performance. Additionally, the HFSS generated impedance matching was re-verified using the CST's Microwave Studio tool, in addition to the measurements, which is shown in Fig. 9. The return loss results using the HFSS and CST tools agree well (3.09 GHz to 4.4GHz, 35%), whereas the measured data shows slightly wider matching bandwidth of 38% (3.09 GHz to 4.60 GHz). Slight disagreement in the S_{11} for the three cases is attributed to the uneven foam surfaces between the FR-4 and the ground plane and the losses associated with the dielectric and the conductors as discussed in the previous section.

The simulated and measured gain radiation patterns for the proposed (reference case) USLMES patch antenna is shown in Fig. 10(a, c, e) and Fig. 10(b, d, f), respectively, for the frequencies 3.14GHz, 3.5GHz and 4.4GHz within the matching bandwidth. The simulated and measured co-polarization gain and peak cross-polarization levels are compared in Table 3 at 3.14GHz, 3.50GHz, and 4.40GHz. It can be seen that measured data agrees reasonably well with simulation ones except towards the higher frequency end. The 3dB beam widths at 3.14GHz, 3.5GHz, and 4.40GHz are 58.54^o, 58.12^o, and

69.80°, respectively. Further, Fig. 11 shows the comparison of the simulated and measured broadside realized gain for the proposed antenna.

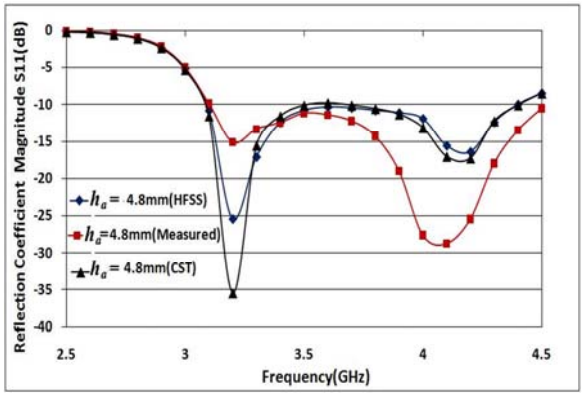

Fig. 9. Simulated and measured reflection coefficient magnitude S_{11} (dB) versus frequency (GHz) for the reference wideband USLMES patch with h_a = 4.8mm.

Table 3: Comparison of simulated and measured gain and peak cross-polarization level

Frequency (GHz)	**Sim. Co-Polar. Gain (dBi)**	**Sim. Cross-Polar. Level (dB)**	**Measured Co-Polar. Gain (dBi)**	**Measured Cross-Polar. Level (dB)**
3.14	9.50	27.64	9.55	20.40
3.50	10.64	29.858	10.07	21.70
4.40	9.31	7.08	7.65	11.59

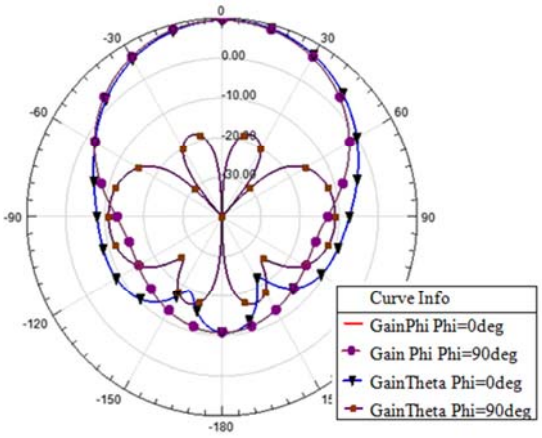

(a)

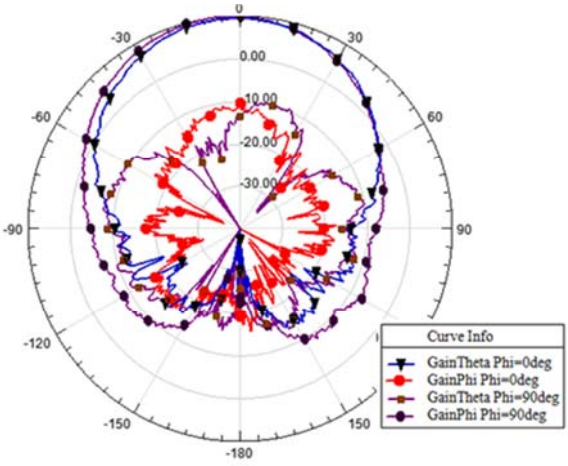

(b)

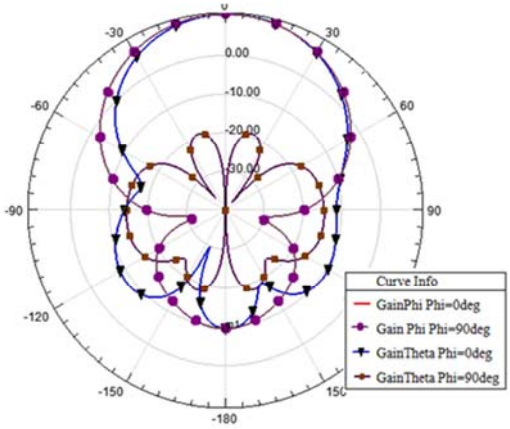

(c)

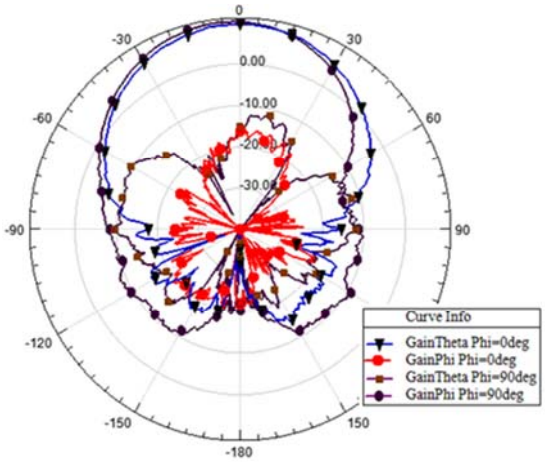

(d)

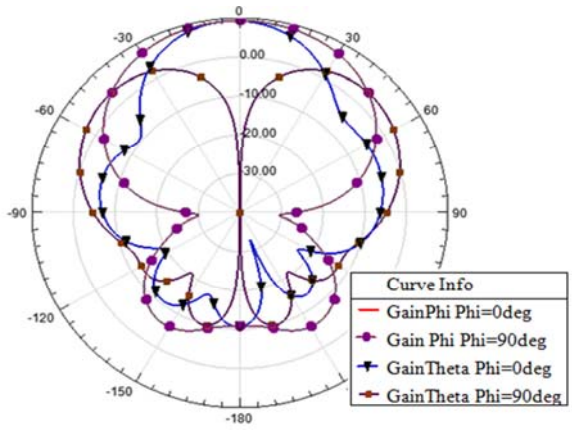

(e)

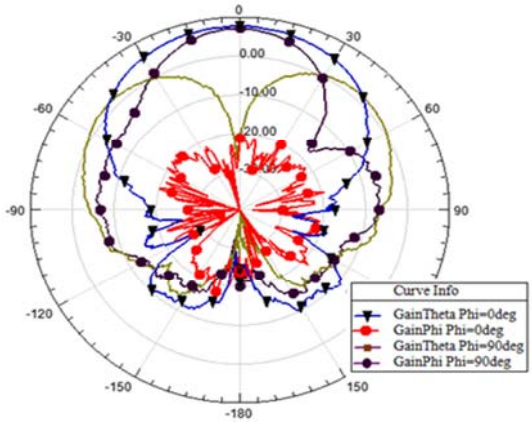

(f)

Fig. 10. Simulated (a, c, e) and measured (b, d, f) gain radiation patterns at 3.14GHz, 3.5GHz, and 4.4GHz, respectively.

The measured results comply with the simulated results affirmatively. The gain drop at 4.4GHz can be attributed to comparatively high cross-polarization than with lower frequencies which arises due to large electrical length of the antenna towards the end of the frequency. With the increase in electrical size, unwanted higher mode can generate causing cross-polarization to go up; however, the cross-polarization level is still very good for most of the wireless communications. Further, the antenna shows 3dB gain bandwidth similar to the impedance matching bandwidth.

V. CONCLUSION

A U-slot loaded modified E-shape (USLMES) microstrip patch antenna is presented that offers simulation impedance bandwidth of 35% while measured bandwidth approaches 38%.

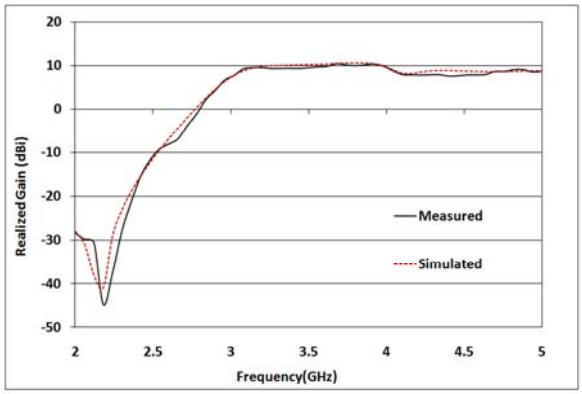

Fig. 11. Comparison of the simulated and measured broadside realized gain (dBi) vs. frequency (GHz) for the proposed (h_a = 4.8mm) USLMES patch antenna.

Additionally, the gain variation is within 3 dB over the impedance bandwidth. This paper also focused on ground plane height control to investigate the frequency agility for a proposed wideband antenna. It can be observed that both dual band and single wideband antennas can be realized by controlling the air-gap between the FR-4 supported patch and the ground plane. The investigations presented considered the mechanical or individual height variations, but it can be made real time, once, a simpler mechanism for electronic variation of ground plane is implemented such that desired levels of air-gap variations could be obtained. This is a matter of future study. Similarly, the effect of incorporating copper conductor ribbon type switches were also studied by modifying the USLMES patch further. It showed frequency agility over the operation bandwidth. These antennas can find an application in 3.5GHz Wi-Fi wireless communication devices as radiating elements for the base station antennas.

ACKNOWLEDGMENT

The work was carried out under the National Science Foundation (NSF)'s CAREER grant # ECCS-0845822. Authors would also like to thank Nathan Labadie for his help in CST simulations and Robert A. Moody for his help in the antenna measurements.

REFERENCES

[1] Y. J. Sung, T. U. Jang, and Y.-S. Kim, "A Reconfigurable Microstrip Antenna for Switchable Polarization," *IEEE Microwave*

and Wireless Components Letters, vol. 14, no. 11, pp. 534-536, 2004.

[2] D. H. Schaubert, F. G. Farrar, A. Sindoris, and S. T. Hayes," Microstrip Antennas with Frequency Agility and Polarization Diversity," *IEEE Transactions on Antennas and Propagation*, vol. 29, no. 1, pp. 118-123, 1981.

[3] F. Yang and Y. Rahmat-Samii, "A Reconfigurable Patch Antenna using Switchable Slots for Circular Polarization Diversity," *IEEE Microwave and Wireless Components Letters*, vol. 12, no. 3, pp. 96-98, 2002.

[4] S. Liu, M.-J. Lee, C. Jung, G.-P. Li, and F. De Flaviis, "A Frequency-Reconfigurable Circularly Polarized Patch Antenna by Integrating MEMS Switches," *IEEE Antennas and Propagation Society International Symposium*, Washington DC, USA vol. 2A, pp. 413-416, July 2005.

[5] W. H. Weedon, W. J. Payne, and G. M. Rebeiz, "MEMS-Switched Reconfigurable Antennas," *IEEE AP-S Int. Symp,* Boston, MA, USA, vol. 3, pp. 654–657, July 2001.

[6] C. Jung, M. Lee, G. P. Li, and F. De Flaviis, "Reconfigurable Scan Beam Single-Arm Spiral Antenna Integrated with RF-MEMS Switches," *IEEE Trans. Antennas Propag.,* vol. 54, pp. 455–463, 2006.

[7] Z. Jin and A. Mortazawi, "An L-Band Tunable Microstrip Antenna using Multiple Varactors," *IEEE Antennas and Propagation Society International Symposium*, Columbus, OH, USA, vol. 4, pp. 524- 527, June 2003.

[8] L. Shafai, S. K. Sharma, L. Shafai, M. Daneshmand, and P. Mousavi "Phase Shift Bandwidth and Scan Range in Microstrip Arrays by the Element Frequency Tuning," *IEEE Transactions on Antennas and Propagation*, vol. 54, no. 5, May 2006.

[9] L. Zhou, S. K. Sharma, and S. Kassegne, "Reconfigurable Microstrip Rectangular Loop Antennas using RF MEMS Switches," *Microwave and Optical Technology Letters (MOTL),* vol. 50, no. 1, pp. 252-256, Jan 2008.

[10] C. Shafai, L. Shafai, R. Al-Dahleh, Dwayne D. Chrusch, and S. K. Sharma, "Reconfigurable Ground Plane Membranes for Analog/Digital Microstrip Phase Shifters and Frequency Agile Antenna," *The 2005 International Conference on MEMS, NANO, and Smart Systems (ICMENS)*, Banff, Alberta, Canada, pp. 287-289, July 2005.

[11] K. F. Lee, K. M. Luk, K. F. Tong, S. M. Shum, T. Huynh, and R. Q. Lee, "Experimental and Simulation Studies of the Coaxially Fed U-Slot Rectangular Patch Antenna," *Proc. Inst. Elec. Eng.*, pt. H, vol. 144, pp.354–358, Oct. 1997.

[12] V. Natarajan and D. Chatterjee, "Comparative Evaluation of Some Empirical Design Techniques for CAD Optimization of Wideband U-Slot Microstrip Antennas," *ACES Journal,* vol. 20, no. 1, pp. 50-69, 2005.

[13] H. F. Pues, and A. R. Van de Capelle, "An Impedance-Matching Technique for Increasing the Bandwidth of Microstrip Antennas," *IEEE Trans. Antennas Propag.*, vol. 37, no. 11, pp. 1345–1354, 2006.

[14] F. Yang, X.-X. Zhang, X. Ye, and Y. Rahmat-Samii, "Wide-Band E Shape Patch Antennas for Wireless Communications," *IEEE Transactions on Antennas and Propagation,* vol. 49, no. 7, July 2001.

[15] Y. Ge, K. P. Esselle, and T. S. Bird "E Shape Patch Antennas for High Speed Wireless Networks," *IEEE Transactions on Antennas and Propagation*, vol. 52, no. 12, December 2004.

[16] I. Bahl, P. Bhartia, R. Garg, and A. Ittipiboon, *Microstrip Patch Antenna Handbook*, Artech House, 2001.

[17] Ansoft Corporations *Designer* and *High Frequency Structure Simulator (HFSS)*.

[18] Computer Simulation Tool (CST)'s *Microwave Studio*, 2009.

[19] C. Shafai, S. K. Sharma, L. Shafai, and D. Chrusch, "Microstrip Phase Shifters using Ground-Plane Reconfiguration," *IEEE Transactions on Microwave Theory and Techniques*, vol. 52, no. 1, pp. 144-153, January 2004.

[20] C. Shafai, S. K. Sharma, J. Yip, L. Shafai, and L. Shafai, "Microstrip Delay Transmission Line Phase Shifters by Actuation of Integrated Ground Plane Membranes," *IET Journal on Microwaves, Antennas and Propagation (IET MAP),* vol. 2, no. 2, pp. 163-170, March 2008.

Satish Kumar Sharma received his Ph.D. degree from the Institute of Technology, Banaras Hindu University, in 1997 in Electronics Engineering. From December 1993 to February 1999, he was a Research Scholar in the Department of Electronics Engineering, Institute of Technology, Banaras Hindu University. From March 1999 to April 2001, he was a Postdoctoral Fellow in the Department of Electrical and Computer Engineering, University of Manitoba. He was a Senior Antenna Engineer with InfoMagnetics Technologies Corporation in Winnipeg, Canada, from May 2001 to August 2006. Simultaneously, he was also a Research Associate at the University of Manitoba from June 2001 to August 2006. In August 2006, he joined San Diego State University (SDSU) as an Assistant Professor in the Department of Electrical and Computer Engineering. Since August 2010, he is an Associate Professor at SDSU. Dr. Sharma received the National Science Foundation's prestigious faculty early development (CAREER) award in 2009. Currently, he serves as an Associate Editor of the IEEE Transaction on Antennas and Propagation journal. He is a full member of the USNC/URSI, Commission B, Senior Member of the IEEE (Antennas and Propagation Society) and a Member of ACES since year 2010.

Combined Field and Circuit Theories in Squirrel-Cage Induction Motors Based on Micro-T Circuit Model

L. Qaseer, F. de León, and S. Purushothaman

Department of Electrical and Computer Engineering
Polytechnic Institute of New York University, Brooklyn, NY 11417, USA
lqaseer@poly.edu, fdeleon@poly.edu, sujitp@ieee.org

Abstract ─ This paper presents an equivalent circuit derived directly from Maxwell's equations in a manner to show the amalgamation of field models and the circuit theory. A micro-T equivalent circuit is obtained from the solution of Maxwell's equations for a cylindrical representation of a squirrel cage induction motor. First, a general form of the field solution is obtained using transfer matrices. A variable transformation is then applied, which makes it possible to derive a circuit for each annular region in the motor. By joining the equivalent circuits in cascade, a complete equivalent circuit for the motor is obtained. The voltages and currents in the equivalent circuit relate directly to the field quantities within the actual motor. Accuracy of the method is verified with comparisons against finite elements and a commercial motor design program.

Index Terms ─ Eddy currents, electromagnetic induction, equivalent circuits, induction motors.

I. INTRODUCTION

Multiregion traveling wave problems in electrical machines have been treated in detail by a number of authors; see for example [1-11]. A traveling wave is usually produced by a polyphase winding, which acts upon a series of laminar regions. A region is defined, for the purposes of this paper, as an area in the motor in which the material is uniform in nature, having boundaries of simple cylindrical shape. When any of the regions is conducting, eddy currents are induced and forces tangential to the plane of the region are established. If the field quantities at the region interfaces are known, these forces can be calculated. Typical problems include linear induction motors [1], rotating induction motors [2-5], drag-cup servomotors [6], liquid metal induction pumps and generators [7], and armature reaction losses in solid poles [8-11].

The theory of induction motors is usually presented in one of two ways: either the motor is represented by a Steinmetz equivalent circuit [12], or analytical expressions are derived from the electromagnetic field theory [2-4], [13]. As of yet there is no general method enabling one to derive an equivalent circuit directly from a field solution. Of course, it is always possible to set up an analogue model of differential equations [14], but the number of elements required for accurate modeling can be very large.

As the number of regions is increased, the algebraic complexity of the field solution becomes prone to errors. Additionally, if the motor model is altered by adding extra regions, it is necessary to repeat the complete field analysis. The micro-T equivalent circuits developed in this paper have the form of cascaded transmission lines; therefore, it is possible to consider any number of regions without recurring to lengthy analyses. The micro-T circuit offers a direct relationship between field quantities in the motor voltages and currents in the equivalent circuit (see Fig. 1).

The use of an equivalent circuit can give deep

Submitted On: January 11, 2011
Accepted On: April 18, 2011

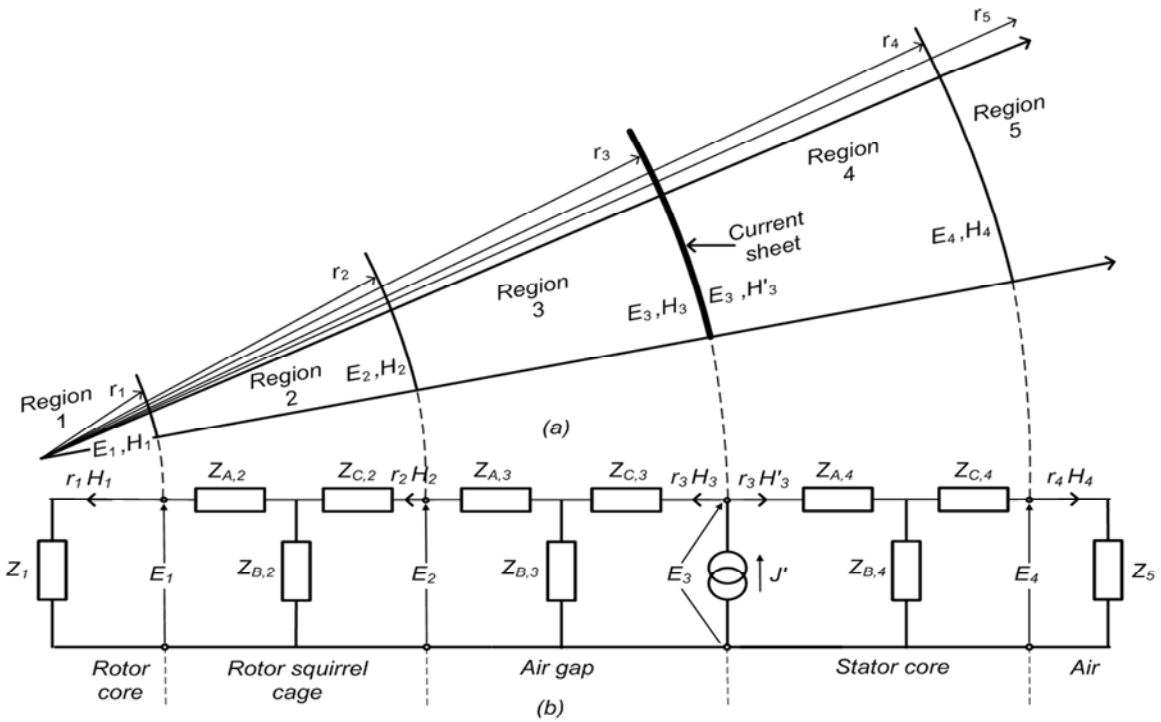

Fig.1. (a) Cross-sectional sextant through a multi-layer squirrel cage induction motor. (b) Basic equivalent circuit for a five-region squirrel cage induction motor.

insight into the behavior of the motor. Engineers are trained to interpret equivalent circuits, and once the circuit elements have been obtained, the amount of calculations required for a given set of conditions is relatively small. The motor model can be made more detailed when adding extra regions by inserting extra terms in the equivalent circuit at the appropriate points.

The combination of field and circuit theories has been used in other areas; see for example [15 and 16]. In [15], a hybrid electromagnetic-circuit is used for the simulation of microwave devices together with nonlinear lumped circuits. A circuit-oriented, finite-element solution is proposed in [16] to analyze travelling wave coupled problems. The micro-T circuit theory has been used in [17] and [18] to analyze induction heating problems.

The contributions of this paper are: the application of the micro-T theory to the solution of the electromagnetic field distribution in squirrel cage induction motors; the derivation of a terminal equivalent circuit from the solution of Maxwell's equations in the motor.

The equivalent circuit of this paper gives information not only on the terminal performance of the motor, but allows looking at the behavior of the electromagnetic field in the different layers. The accuracy of the method has been verified with finite elements simulations and with the equivalent circuit on a real motor.

II. MATHEMATICAL MODEL

A general multiregion problem is analyzed. Figure 1a shows a sextant of a motor comprising of N (=5) concentric cylinders. The excitation is an infinitesimally thin and axially infinite current sheet at radius r_g. It is further assumed that displacement currents and magnetic saturation are negligible.

Three field quantities which are acting at the region boundaries will be considered in this analysis. These are the electric field strength E which is directed axially along the interface, the magnetic field strength H which is directed circumferentially along the interface, and the third one is the flux density B normal to the interface in the radial direction. The analysis using these field components is performed to obtain field quantities at the region boundaries. After these field quantities are known, the equivalent circuit is then derived and the power flow through the interfaces, torque, output power, rotor losses, and rotational force are obtained.

The intermediate stage between the field

solution and the final equivalent circuit is represented in a transmission line form [17]. The *E* and *H* values on either side of a region are linked by a transfer matrix [19-20]. Therefore each bounded region in the model shown in Fig. 1 can be represented by a corresponding transfer matrix equation.

The circuit model of this paper is derived from the analytical solution of Maxwell's equations. The following geometrical simplifications have been made: (1) the stator windings (including slots and teeth) have been substituted by a current sheet; (2) the squirrel cage has been substituted by a conductive equivalent layer. The first assumption prevents the accurate representation of the stator winding resistance while the second assumption produces a larger than normal magnetizing current. Both limitations can be potentially eliminated with the use of homogenous equivalent media [20]. This, however, is beyond the scope of this paper, but we intend to continue our research in that direction.

III. THEORETICAL ANALYSIS

A. Field theory solution of a general region

It is assumed that the winding produces a perfect sinusoidal traveling wave. The line current density may be represented as

$$J_z = \mathrm{Re}\left\{\hat{J}\ e^{j(\omega t - p\varphi)}\right\} \tag{1}$$

where $\hat{J}$, ω and p are the amplitude of line current density, angular frequency, and the number of pole pairs. The field produced will link all cylindrical regions from 1 to *N*. Maxwell's equations are solved accordingly. As a first step in the analysis, the field components of a general region are derived, assuming that all fields vary as $\exp(\omega t - p\phi)$, and omitting this factor from all field expressions that follow (we work only with the amplitudes of the travelling wave functions). Then, Maxwell's equations for any region in the model are:

$$\nabla \times \hat{H} = \hat{J}, \tag{2}$$

$$\nabla \times \hat{E} = -j\omega\hat{B}, \tag{3}$$

with

$$\hat{J} = \sigma\hat{E}, \tag{4}$$

and

$$\hat{B} = \mu\hat{H}. \tag{5}$$

The boundary conditions are

1) The radial component of the flux density is continuous across a boundary.
2) The circumferential component of magnetic field strength is continuous across a boundary, but one must consider the effects of the current sheet as shown in sub-section B.

Taking the *r*-component from both sides of (3) yields

$$E_z = \frac{\omega}{p}\left(rB_r\right), \tag{6}$$

and taking only the Φ-component from both sides of (3) yields

$$\frac{\partial E_z}{\partial r} = j\omega\mu H_\varphi. \tag{7}$$

Using (2) and (4) and taking the *z*-component from both sides gives

$$\sigma E_z = \frac{1}{r}\frac{\partial}{\partial r}\left(rH_\varphi\right) + j\frac{p}{r}H_r. \tag{8}$$

Equation (8) can be written, after rearranging, in the following form

$$r^2\frac{\partial^2 E_z}{\partial r^2} + r\frac{\partial E_z}{\partial r} - \left(\alpha^2 r^2 + p^2\right)E_z = 0. \tag{9}$$

The solution is given by

$$E_z = C_1 I_p\left(\alpha r\right) + C_2 K_p\left(\alpha r\right), \tag{10}$$

where I_p and K_p are the modified Bessel functions of order p and of general complex argument, C_1 and C_2 are constants to be evaluated from boundary conditions, and $\alpha^2 = j\omega\mu\sigma$ where μ and σ represent the absolute permeability and conductivity and ω is replaced by $s\omega$ in the above equation for a region moving with slip s.

From (3), (5), and (10) we have

$$H_\varphi = \frac{\alpha}{j\omega\mu}\left[C_1 I_p'\left(\alpha r\right) + C_2 K_p'\left(\alpha r\right)\right]. \tag{11}$$

For non-conducting regions or regions moving at synchronous speed, the governing partial differential equation is

$$r^2\frac{\partial^2 E_z}{\partial r^2} + r\frac{\partial E_z}{\partial r} - p^2 E_z = 0, \tag{12}$$

and the solution is given by

$$E_z = C_1 r^{-p} + C_2 r^{p}. \tag{13}$$

Therefore,

$$H_\varphi = -\frac{p}{j\omega r\mu}\left(C_1 r^{-p} - C_2 r^{p}\right). \tag{14}$$

B. Field calculations at region boundaries

Figure 2a shows a general region n, where $E_{z,n}$ and $H_{\Phi,n}$ are the field components at the upper boundary of region n, and $E_{z,n-1}$ and $H_{\Phi,n-1}$ are the equivalent values at the lower boundary of the same region. Considering a conducting region whose slip is different from zero, from (10) and (11)

$$E_{z,n} = C_1 I_p(\alpha_n r_n) + C_2 K_p(\alpha_n r_n), \tag{15}$$

$$H_{\varphi,n} = \frac{\alpha_n}{j\omega\mu_n}\left[C_1 I'_p(\alpha_n r_n) + C_2 K'_p(\alpha_n r_n)\right]. \tag{16}$$

Equivalent expressions for $E_{z,n-1}$ and $H_{\Phi,n-1}$ can be found by replacing r_n in the above equations by r_{n-1}. Similar argument applies for a non-conducting region using (13) and (14). Now for regions $1< n < N$ we have:

$$\begin{bmatrix} E_{z,n} \\ H_{\varphi,n} \end{bmatrix} = [T_n] \cdot \begin{bmatrix} E_{z,n-1} \\ H_{\varphi,n-1} \end{bmatrix}, \tag{17}$$

where $[T_n]$ is the transfer matrix [19], [22] for region n and is given by

$$[T_n] = \begin{bmatrix} a_n & b_n \\ c_n & d_n \end{bmatrix}. \tag{18}$$

The expressions for a_n, b_n, c_n, and d_n are given in the Appendix. Knowing the values of E_z and H_Φ at the inner boundary of a region, the values of E_z and H_Φ at the outer boundary can be obtained from this simple transfer matrix relation. At the boundaries where no excitation current sheet exists, E_z and H_Φ are continuous; thus for example, if two contiguous regions have no current sheet at the common boundary, knowing E_z and H_Φ at the inner boundary of the external region, E_z and H_Φ at the outer boundary of the inner region can be calculated by successive use of the underlying two transfer matrices. Consider that the excitation current sheet is located at radius r_g, then

$$H'_{\varphi,n} = H_{\varphi,n}, \ n \neq g, \tag{19}$$

$$H'_{\varphi,n} = H_{\varphi,n} + J', \ n = g, \tag{20}$$

where $H_{\Phi,n}$ is the circumferential magnetic field strength in close inner proximity to the boundary and $H_{\Phi,n}'$ is the circumferential magnetic field strength in close outer proximity to the boundary.

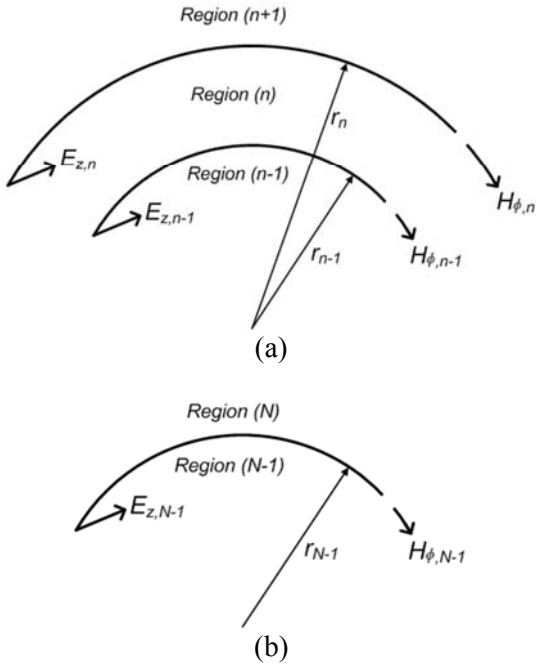

Fig. 2. Mathematical model. (a) General region *n;* (b) end region *N.*

Bearing in mind the boundary conditions, it is apparent that for the model considered, we can write

$$\begin{bmatrix} E_{z,n-1} \\ H_{\varphi,n-1} \end{bmatrix} = [T_{n-1}] \cdot [T_{n-2}] \cdots [T_{g+1}] \cdot \begin{bmatrix} E_{z,g} \\ H_{\varphi,g} + J' \end{bmatrix}, \tag{21}$$

$$\begin{bmatrix} E_{z,g} \\ H_{\varphi,g} \end{bmatrix} = [T_g] \cdot [T_{g-1}] \cdots [T_2] \cdot \begin{bmatrix} E_{z,1} \\ H_{\varphi,1} \end{bmatrix}. \tag{22}$$

If regions 1 and N are now considered then the field should vanish for $r=0$ and $r=\infty$, hence

$$E_{z,1} = C_2 r_1^p, \tag{23}$$

$$H_{\varphi,1} = \frac{p}{j\omega\mu r_1} C_2 r_1^p, \tag{24}$$

$$E_{z,N-1} = C_1 r_{N-1}^{-p}, \tag{25}$$

$$H_{\varphi,N-1} = -\frac{p}{j\omega\mu r_{N-1}} C_1 r_{N-1}^p. \tag{26}$$

The field components at the boundaries of regions 1 and N still contain unknown constants. The ratios, however, of E_z and H_Φ at these boundaries contain no constants and it is only these ratios that are needed for a complete solution.

C. Surface impedance calculation

The surface impedance looking outward at a boundary of radius r_n is defined as

$$Z_{n+1} = -\frac{E_{z,n}}{H_{\varphi,n}}, \tag{27}$$

and the surface impedance looking inwards is defined as

$$Z_n = \frac{E_{z,n}}{H_{\varphi,n}}. \tag{28}$$

With the values of $E_{z,N-1}$, $H_{\Phi,N-1}$, $E_{z,1}$, $H_{\Phi,1}$ and a_n, b_n, c_n, and d_n as derived in the previous section we have at the current sheet (for n=g):

$$Z_{in} = \frac{Z_g \cdot Z_{g+1}}{Z_g + Z_{g+1}}, \tag{29}$$

where Z_{in} is the input surface impedance at the current sheet and Z_{g+1} and Z_g are the surface impedances looking outwards and inwards at the current sheet. Substituting for Z_{g+1} and Z_g using (27) and (28) and rearranging gives

$$Z_{in} = \frac{E_{z,g}}{H_{\varphi,g} - H'_{\varphi,g}} = -\frac{E_{z,g}}{J'}, \tag{30}$$

thus, the input surface impedance at the current sheet has been determined. This means that all field components can be found by making use of this and (28), (21), (22).

D. The micro-T terminal equivalent circuit

The transmission-line form of (21) and (22) suggests that, by analogy, some form of equivalent circuit is possible [22, 23]. No loss of generality occurs if only one region is considered. The electric and magnetic field quantities are linked as shown in (17). In order to represent the relationship between E_n, H_n and E_{n-1}, H_{n-1} by a corresponding T-circuit, a change of variable is required. A practical variable transformation refers to the variable H, which is changed to rH. A T-circuit can now be used to link the variables E and rH on either side of a region as shown in Fig. 3.

The current r_nH_n in a T-circuit is driven by a voltage E_n. For the general region n, the impedances are given by the following relations

$$Z_{B,n} = \frac{1}{r_n c_n}, \tag{31}$$

$$Z_{A,n} = Z_{B,n}\left(d_n \frac{r_n}{r_{n-1}} - 1\right), \tag{32}$$

$$Z_{C,n} = Z_{B,n}\left(a_n - 1\right). \tag{33}$$

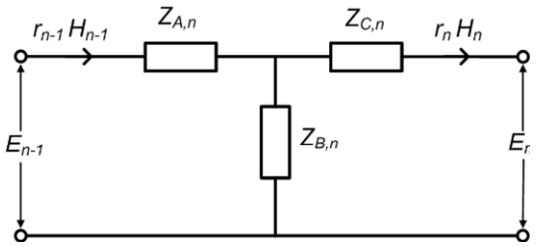

Fig. 3. Basic T-circuit for region n.

When the T-circuits are joined in cascade, the full equivalent circuit is obtained as shown in Fig. 1b where, by the use of (28) and (27), the following expressions are obtained [23].

$$Z_1 = \frac{E_1}{r_1 H_1}. \tag{34}$$

$$Z_N = -\frac{E_{N-1}}{r_{N-1} H_{N-1}}. \tag{35}$$

Thus, an equivalent circuit has been derived by rearrangement of the field solution, where the voltages and currents are directly related to the field quantities. Furthermore, the normal flux density at any interface can be obtained in the form

$$B_{r,n} = \frac{p E_{z,n}}{\omega r_n}. \tag{36}$$

It is convenient to write the equations in terms of phase voltages and currents. The input quantities to the basic equivalent circuit are the current $r_g J'$ and the voltage E_g. The relation between J' and the rms phase current I can be written as

$$r_g J' = \frac{3\sqrt{2} N_{eff} I}{\pi}, \tag{37}$$

where N_{eff} is the effective number of series turns per phase, therefore

$$I = \left(I_{fac}\right) J' r_g, \tag{38a}$$

where:

$$I_{fac} = \frac{\pi}{3\sqrt{2} N_{eff}}, \tag{38b}$$

and for a motor of length l m, the rms phase voltage V is related to E_g by

$$V = \sqrt{2} N_{eff} E_g l, \tag{39}$$

therefore,

$$V = \left(V_{fac}\right) E_g \,, \tag{40a}$$

where

$$V_{fac} = \sqrt{2} N_{eff} l \,. \tag{40b}$$

Let us now consider the effect of multiplying the quantities E_n and $r_n H_n$ terms in the basic equivalent circuit by the factors V_{fac} and I_{fac}, respectively; then, the impedances in the basic circuit have to be multiplied by an impedance factor given by

$$Z_{fac} = \frac{V_{fac}}{I_{fac}} = \frac{6 N_{eff}^2 l}{\pi}, \tag{41}$$

and the terminal impedance of the machine is given by

$$Z_t = Z_{fac} \frac{Z_{in}}{r_g} \,. \tag{42}$$

The result is a completely new equivalent circuit in which the input quantities are the rms phase voltage and rms phase current using (40) and (38). Thus, the various voltages and currents at the input to each T-circuit are now related directly to the field quantities at the corresponding interfaces in the machine. The terminal equivalent circuit has all the advantages of the basic circuit but, in addition, the impedances are real impedances. The voltages and currents appearing in the circuit can be used in (40) and (37) in order to obtain the field quantities E_z, B_r, and B_Φ at any desired region boundary.

Using the terminal impedance, the rotor resistance, rotor leakage reactance, and magnetizing reactance can be obtained.

The rotor resistance is obtained from the terminal impedance at standstill as $r_2 = \mathrm{Re}\{Z_t\}$ and the leakage reactance is obtained from the terminal impedance at standstill as $x_2 = \mathrm{Im}\{Z_t\}$.

The magnetizing impedance is obtained from the terminal impedance at synchronous speed. It should be noted that the real part of the terminal impedance is zero at this speed. The stator winding resistance can be simply joined in series at the input terminals. From above an equivalent circuit analogous to classical theory can be derived as will be shown in the next section.

The time-average input power density P_{in} [W/m^2] passing through a surface can be calculated through the concept of the Poynting theorem in the field solution as:

$$P_{in} = \frac{1}{2} \mathrm{Re}\left\{ \bar{E} \times \bar{H}^* \right\}, \tag{43}$$

and the total power P_w [W] is given by

$$P_w = \frac{1}{2} \left| E_g \right|^2 \mathrm{Re}\left\{ \frac{2\pi r_g l}{Z_{in}^*} \right\}. \tag{44}$$

Using the terminal equivalent circuit, the total power is calculated as

$$P_w = 3\,\mathrm{Re}\left\{ VI^* \right\} = 3\,\mathrm{Re}\left\{ \frac{\left|V\right|^2}{Z_t^*} \right\}, \tag{45}$$

and the torque T [N-m] is given by

$$T = \frac{P_w}{\omega} \,. \tag{46}$$

The force in the circumferential direction F_z is calculated as

$$F_z = \frac{T}{r_r}, \tag{47}$$

where r_r is the outer rotor radius.

IV. NUMERICAL RESULTS

The equivalent circuit method that has been described in the previous section is validated using a commercial finite element program (Comsol Multiphysics [25]) along with a real motor whose data is given in Table I.

Figure 4 shows the finite element discretization of the model. It should be noted that the air gap layer is not visible in this to scale drawing. Figures 5a and 5b show the radial and circumferential flux density components respectively using both the micro-T circuit model and the finite element method (FEM), for standstill and rated speed conditions. The magnitude of flux density is greater at the rated speed since most of the flux is magnetizing while its leakage flux is under standstill conditions.

Figures 6 and 7 show the flux contours at standstill and rated speed, respectively. At the rated speed, the skin depth in the rotor conductor is appreciable, allowing flux to penetrate the rotor core while at a standstill, the skin depth is much lower, hence forcing the flux to concentrate around the air gap.

Table I: Machine data

Rated power, (W)	746
Number of poles	2
Line stator voltage, (V)	220
Number of turns per phase	86
Frequency, (Hz)	60
Rated speed, (rpm)	3358
Efficiency, (%)	89
Rated slip	0.067
Rotor core radius, (mm)	32.6
Outer rotor radius, (mm)	46.5
Inner stator radius, (mm)	46.8
Outer stator radius, (mm)	63
Relative permeability of iron	4000
Rotor conductivity, (S/m)	1.56×10^{7}

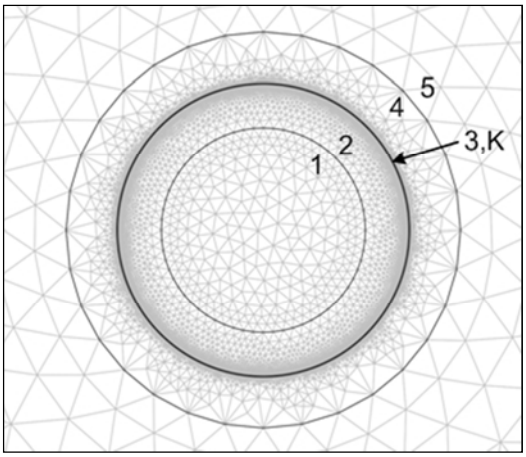

Fig. 4. Finite element discretization of model.

Figure 8 compares the torque-speed characteristic for the following four cases:

(1) The true behavior of a real motor designed with RMxprt, a commercially available computer software [24], which works based on the magnetic circuit approach to predict the performance parameters. This curve is obtained from the equivalent circuit given by RMxprt and corresponds to the base case.
(2) The equivalent circuit with the stator resistance neglected. This is done to gauge the effect of the first assumption in the derivation of the analytical model.
(3) The base case, but with the stator windings represented by a current sheet and the squirrel cage bars represented by a conductive layer (as in Fig. 4). This case is obtained with finite element simulations using Comsol Muti-physics.
(4) The plot corresponding to the analytical model of this paper.

One can appreciate that the performance of this paper's model is identical to the numerical solution for the same geometry and not too far from the true motor.

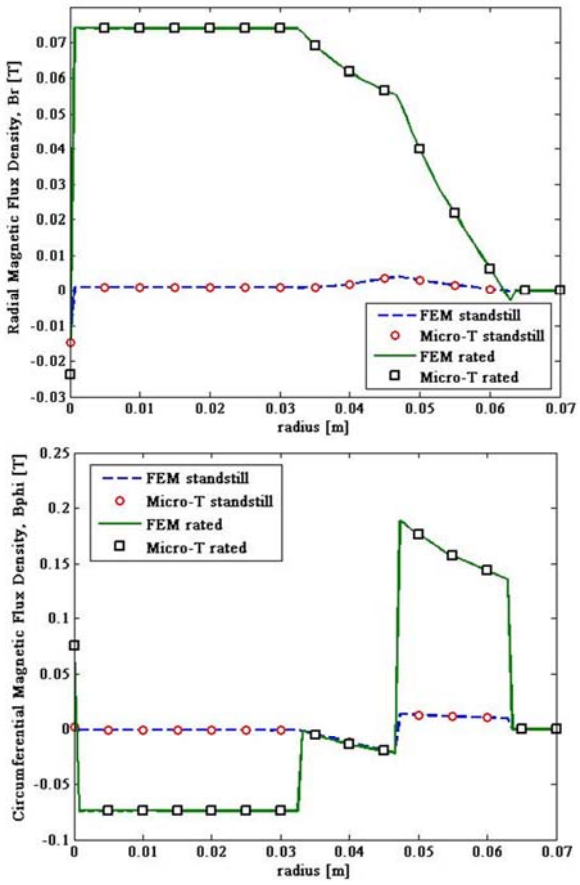

(b)

Fig. 5. (a) Comparison of radial flux density computed from FEM and micro-T circuit model. (b) Comparison of circumferential flux density computed from FEM and micro-T circuit model.

V. CONCLUSIONS

The micro-T circuit has been used for the analysis of squirrel-cage induction motors. It can be used for any number of regions, and in addition, with any number of stator poles so that our proposed method of analysis becomes quite general.

Given just the voltages at the terminal equivalent circuit, all field quantities at any region boundary can be easily derived, as well as air gap power, losses, output power and torque.

Using such circuits may provide a better technical insight into the system than is possible from studying the full-wave solutions from a computational electromagnetics analysis.

The obtained results agree well with the data from the corresponding finite element method analysis as well as with the equivalent circuit of a real motor (with no stator). Therefore, the micro-T circuit can reproduce the behavior of the terminal equivalent circuit and gives physical meaning to the elements of the circuit.

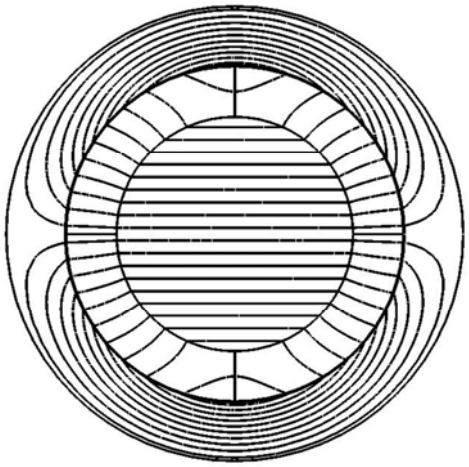

Fig. 6. Flux contour plot at rated speed.

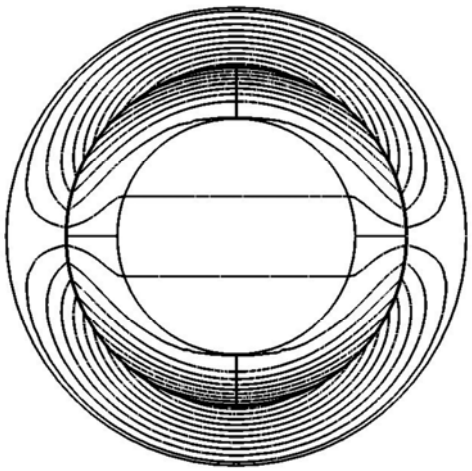

Fig. 7. Flux contour plot at standstill.

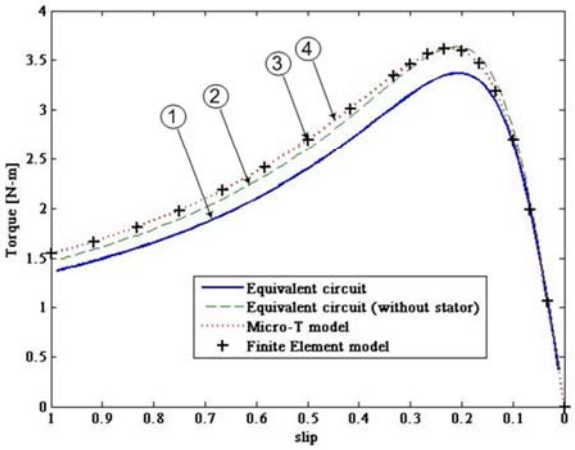

Fig. 8. Comparison of torque-speed characteristics for the following cases: (1) True behavior of the motor computed by RMxpert (reluctance network). (2) Neglecting stator resistance. (3) Stator windings represented as a current sheet and squirrel cage represented by a conductive layer computed with Comsol (FEM). (4) Analytical model of this paper.

VI. APPENDIX – CALCULATION OF THE ELEMENTS OF THE TRANSFER MATRIX

Equations (15) and (16) are solved for the constants C_1 and C_2 at the inner boundary of a non-conducting region n. Then the values of these constants are used for the same region at the outer boundary. The two equations thus obtained relate field quantities at the outer and inner boundary of region n with no constants. The same method is applied for a conducting region whose slip is different from zero using (15) and (16). The result is as follows:

1. Transfer matrix elements for regions in which $s_n.\sigma_n \neq 0$.

$$a_n = -\alpha_n r_{n-1}[I_p(\alpha_n r_n)\cdot K'_p(\alpha_n r_{n-1}) - K_p(\alpha_n r_n)\cdot I'_p(\alpha_n r_{n-1})], \quad (48)$$

$$b_n = -j\omega\mu_n r_{n-1}[I_p(\alpha_n r_{n-1})\cdot K_p(\alpha_n r_n) - I_p(\alpha_n r_n)\cdot K_p(\alpha_n r_{n-1})], \quad (49)$$

$$c_n = -s_n\sigma_n r_{n-1}[I'_p(\alpha_n r_n)\cdot K'_p(\alpha_n r_{n-1}) - K'_p(\alpha_n r_n)\cdot I'_p(\alpha_n r_{n-1})], \quad (50)$$

$$d_n = -\alpha_n r_{n-1}[I_p(\alpha_n r_{n-1})\cdot K'_p(\alpha_n r_n) - K_p(\alpha_n r_{n-1})\cdot I'_p(\alpha_n r_n)], \quad (51)$$

where σ_n and s_n are the conductivity and slip of region n, respectively.

2. Transfer matrix elements for regions in which $s_n.\sigma_n = 0$.

$$a_n = \frac{1}{2}(\xi^p + \xi^{-p}), \quad (52)$$

$$b_n = j\frac{1}{2}\omega\mu_n r_{n-1}\left(\frac{\xi^p - \xi^{-p}}{p}\right), \quad (53)$$

$$c_n = \frac{1}{2}\frac{p}{j\omega\mu_n r_n}\left(\xi^p - \xi^{-p}\right), \quad (54)$$

$$d_n = \frac{1}{2}\left(\frac{\xi^p + \xi^{-p}}{\xi}\right), \quad (55)$$

where

$$\xi = \frac{r_n}{r_{n-1}}. \quad (56)$$

ACKNOWLEDGEMENT

The authors would like to recognize the contribution of Prof. N. K. Al-Sahib for the support of the University of Baghdad.

REFERENCES

[1] E. R. Laithwaite, *Induction Machines for Special Purposes*, Newnes, Oxford, U.K., 1966.

[2] A. L. Cullen and T. H. Barton, "A Simplified Electromagnetic Theory of the Induction Motor using the Concept of Wave Impedance," *Proc. IEE*, vol. 105C, pp. 331-336, 1958.

[3] L. S. Piggot, "A Theory of the Operation of Cylindrical Induction Motors with Squirrel-Cage Rotors," *Proc. IEE*, vol. 109C, pp. 270-282, 1962.

[4] E. Mishkin, "Theory of the Squirrel-Cage Induction Motor Derived Directly from Maxwell's Field Equations," *Quart. J. Mech. Appl. Maths*., no. 7, pp. 472-487, 1954.

[5] J. C. Wilson, E. A. Erdely, and R. E. Hopkins, "Aerospace Composite-Rotor Induction Motors," *IEEE Trans.* AES-3. Suppl., pp.18-23, 1965.

[6] J. C. West and D. E. Hesmondhalgh, "The Analysis of Thick-Cylinder Induction Machines," *Proc. IEE*, vol. 109C, pp. 172-181, 1962.

[7] W. D. Jackson and E. S. Pierson, "Operating Characteristics of the M.P.D. Induction Generator," *IEE conf*., rep. 4, pp. 38-42, 1962.

[8] R. L. Stoll and P. Hammond, "Calculation of the Magnetic Field of Rotating Machines-Pt. 4. Approximate Determination of the Field and the Losses Associated with Eddy Currents in Conducting Surfaces," *Proc. IEE*, vol. 112, no.11, pp. 2083-2094, 1965.

[9] P. J. Lawrenson, P. Reece, and M. C. Ralph, "Tooth-Ripple Losses in Solid Poles," *Proc. IEE*, vol. 113, no. 4, pp. 657-662, 1966.

[10] L. Concordia and H. Poritsky, "Synchronous Machine with Cylindrical Rotor," *Trans. Amer. Inst. Elect. Engrs*, vol. 56, pp. 49-58, 1937.

[11] A. J. Wood, "An Analysis of Solid Rotor Machines," *Trans. Amer. Inst. Elect. Engrs*, vol. 79, pp. 1657-1665, 1960.

[12] C. Steinmetz, *Theory and Calculation of Alternating Current Phenomena,* W. J. Johnston Company, New York, 1897.

[13] C. V. Jones, "Unification of Field and Circuit Theories of Electrical Machines," *Proc. IEE*, vol. 119, no. 7, pp. 871-876, 1972.

[14] B. Beland and J. Richard, "A New Transmission Line Representation of Eddy-Current Problems in Cylinders," *IEEE Trans*. vol. PAS-90, no. 5, pp. 2181-2185, 1971.

[15] R. Wang and J. M. Jin, "A Symmetric Electromagnetic-Circuit Simulator Based on the Extended Time-Domain Finite Element Method," *IEEE Transactions on Microwave Theory and Techniques*, vol. 56, no. 12, pp. 2875-2884, December 2008.

[16] M. Feliziani and F. Maradei, "Circuit-Oriented FEM: Solution of Circuit-Field Coupled Problems by Circuit Equations Magnetics," *IEEE Transactions on Magnetics*, pp. 965 – 968, vol. 38, no. 2, Mar. 2002.

[17] L. J. Qaseer, "The Micro-T Circuit Model for the Analysis of Cylindrical Induction Heating Systems," *IEEE Trans. Energy Convers*., vol. 25, no. 4, pp. 1021-1027, 2010.

[18] L. J. Qaseer, "Micro-T Circuit Model for Double and Single Sided Induction Heating Systems," *Applied Computational Electromagnetic Society (ACES) Journal*, vol. 25, no. 8, pp. 713–721, August 2010.

[19] J. Greig and E. M. Freeman, "Traveling Wave Problem in Electrical Machine," *Proc. IEE*, vol. 114, no. 11, pp. 1681-1683, 1967.
[20] E. M. Freeman, "Traveling Waves in Induction Machines: Input Impedance and Equivalent Circuits," *Proc. IEE*, vol. 115, no. 12, pp. 1772-1776, 1968.
[21] E. M. Freeman and B. E. Smith, "Surface Impedance Method Applied to Multilayer Cylindrical Induction Devices with Circumferential Exciting Currents," *Proc. IEE*, vol. 117, no. 10, pp. 2012-2013, 1970.
[22] L. A. Pipes, "Matrix Theory of Skin Effect in Laminations," *J. Franklin Inst.*, vol. 262, pp. 127-138, 1956.
[23] E. M. Freeman and T. G. Bland, "Equivalent Circuit of Concentric Cylindrical Conductors in an Axial Alternating Magnetic Field," *Proc. IEE*, vol. 123, no. 2, pp. 149-152, 1976.
[24] Ansoft RMxprt, http://www.ansoft.com/products/em/rmxprt/
[25] Comsol Multiphysics, *ACDC Module User's Guide*, Comsol AB Group, 2010, pp. 1-222.

Layth Qaseer received his B.Sc., M.Sc., and Ph.D. degrees from the University of Baghdad, Baghdad, Iraq in 1979, 1993, and 2004 respectively, all in electrical engineering. Between 1979 and 2001, he worked at the National Scientific Research Center and the Ministry of Industry. In 2005, he joined the Department of Mechatronic Engineering at the University of Baghdad. He is currently with the Department of Electrical and Computer Engineering at the Polytechnic Institute of New York University. His research interest includes rotary, flat linear, tubular linear, and helical motion induction motors as well as induction heating systems.

Francisco de León (S'86–M'92–SM'02) received the B.Sc. and the M.Sc. (Hons.) degrees in Electrical Engineering from the National Polytechnic Institute, Mexico City, Mexico, in 1983 and 1986, respectively, and the Ph.D. degree from the University of Toronto, Toronto, ON, Canada, in 1992. He has held several academic positions in Mexico and has worked for the Canadian electric industry. Currently, he is an Associate Professor at the Polytechnic Institute of NYU, Brooklyn, NY. His research interests include the analysis of power definitions under nonsinusoidal conditions, the transient and steady-state analyses of power systems, the thermal rating of cables and transformers, and the calculation of electromagnetic fields applied to machine design and modeling.

Sujit Purushothaman (S'09) received his B.E. degree in Electrical Engineering from Mumbai University (Sardar Patel College of Engineering), India in 2005. His work experience includes testing and development of medium voltage switchgear for Siemens India. He received his Master's degree in 2009 and is currently pursuing his Ph.D. at Polytechnic Institute of NYU. His research interest includes power system transients, subsynchronous resonance damping, machine design and modeling, and thermal modeling of electrical machines.

Efficient Direct Solution of EFIE for Electrically Large Scattering Problems using $\mathcal{H}$-LDLT and PE Basis Function

Ting Wan, Rushan Chen, Xiaoqing Hu, Yilin Chen, and Yijun Sheng

Department of Communication Engineering
Nanjing University of Science and Technology, Nanjing, 210094, China
billwanting@163.com

Abstract ─ Method of moments (MoM) solution of the electric field integral equations (EFIE) encounters the large memory requirements and the slow convergence rate of the iterative solver. A direct method based on hierarchical ($\mathcal{H}$-) matrix algorithm and phase extracted (PE) basis function is proposed to overcome these obstacles. A recompressed adaptive cross approximation (ACA) technique is employed to generate a data-sparse representation of the dense EFIE system matrix, i.e., so-called $\mathcal{H}$-matrix. $\mathcal{H}$-matrix formatted LDLT-decomposition ($\mathcal{H}$-LDLT) can be implemented in nearly optimal complexity, which provides an efficient way for the direct solution of EFIE. PE basis function, containing the propagating wave phase factor and defined on large patches, is introduced to further reduce the computational costs. Numerical results demonstrate the accuracy and efficiency of the proposed method for electrically large scattering problems.

Index Terms ─ Direct solution, electrically large scattering, hierarchical LDLT-decomposition ($\mathcal{H}$-LDLT), phase extracted (PE) basis function, recompressed adaptive cross approximation (ACA).

I. INTRODUCTION

The electric-field integral equation (EFIE) is widely used to analyze electromagnetic scattering since it can handle fairly general geometries [1]. The method of moments (MoM) is a powerful technique for the solution of EFIE. Numerical discretization of the EFIE by MoM [2] yields a dense complex linear system, which is a serious handicap especially for electrically large scattering problems. Two distinct approaches have recently emerged to address this issue. The first concerns efficient methods for the solution of the large dense linear system. The second directly pursue a reduction of the number of unknowns required to obtain an accurate result. In respect of the first point, methods for the numerical solution of the linear system can usually be classified into two categories, i.e., direct methods and iterative methods. It is basically impractical to use direct methods due to the $O(N^2)$ memory requirement and $O(N^3)$ computational complexity, where N refers to the number of unknowns. This can be circumvented by iterative methods, in which the required matrix-vector product operation can be accelerated by multilevel fast multipole method (MLFMM) [3-6]. However, a linear system resulting from EFIE is usually ill-conditioned, particularly for electrically large problems. Effective preconditioners can be used to accelerate the convergence rate of iterations, but they are usually problem-dependent [7,8]. Moreover, for electrically large problems, the memory is still burdened due to the filling of near-interaction blocks. As the second approach mentioned above, other interesting contributions attempt to reduce the complexity by considering more elaborate bases to approximate the unknown field, such as, the physical optics (PO) method, geometrical optics (GO) method, and characteristic basis function (CBF) method [9-12]. Besides, a kind of basis functions with phase information, named phase extracted (PE) basis functions, has recently been presented [13-15]. Since the induced currents

Submitted On: July 7, 2011
Accepted On: August 12, 2011

on the smooth PEC surface have the propagating wave phase dependency, the PE bases can be defined on very large patches.

Combining the two approaches mentioned above, in this paper, an efficient direct method based on hierarchical LDLT-decomposition ($\mathcal{H}$-LDLT) algorithm and PE basis function is presented to improve the MoM solution of EFIE. $\mathcal{H}$-matrix algorithm are based on the data-sparse representation, which is an inexpensive but sufficiently accurate way to approximate a fully populated matrix [16-18]. The key idea is to approximate a full matrix by a product of two low-rank matrices [16,19]. In this paper, the adaptive cross approximation (ACA) algorithm is used to generate the low-rank approximations [20-23]. A major advantage of ACA is that it deals only with the matrix entries and is, therefore, kernel-independent in contrast to other compression methods like fast multipole [3], panel clustering [24], or the $\mathcal{H}^2$-matrix approximation [25] that are based on expansions or interpolations of the kernel-function. Hence, a practical advantage of ACA is that it can be built on top of existing computer codes without changes. A blockwise recompression scheme is applied following ACA to decrease the memory usage. The essential operations of $\mathcal{H}$-matrices, such as matrix-vector and matrix-matrix multiplication, addition, and LU decomposition, can be performed through $\mathcal{H}$-matrix arithmetic in $O(k^a N \log^b N)$ complexity with blockwise rank k and appropriate parameters a, b [26]. The PE basis function is introduced to reduce the number of unknowns, which creates more favourable conditions for the implement of $\mathcal{H}$-LDLT. Expressing the propagating wave phase dependency, the PE bases break the well-known convention of '10 degrees of freedom per wavelength' and can be defined on the patches with much larger electrical size. Hence, the use of PE basis functions leads to a dramatically computational saving. Numerical examples will show that the proposed method can significantly reduce the memory requirement and computational complexity compared with the traditional direct method and is robust for electrically large scattering problems.

The remainder of this paper is organized as follows: Section II describes the theory and implementation of PE basis functions, the recompressed ACA technique, and the $\mathcal{H}$-LDLT algorithm in detail. Numerical experiments with several electrically large scattering problems are presented to demonstrate the efficiency of the proposed method in Section III. Section IV gives some conclusions.

II. THEORY

A. MoM solution of EFIE with phase extracted basis functions

Consider an arbitrarily-shaped 3D conducting object illuminated by an incident field $\mathbf{E}^i(\mathbf{r})$. The EFIE is given by

$$\hat{n} \times \iint_S \bar{\boldsymbol{G}}(\mathbf{r},\mathbf{r}') \mathbf{J}(\mathbf{r}') d\mathbf{r}' = \frac{1}{jk_0\eta_0} \hat{n} \times \mathbf{E}^i(\mathbf{r}) \text{ on } S, \quad (1)$$

where S denotes the conducting surface of the object, $\hat{n}$ is an outwardly directed normal, $\bar{\boldsymbol{G}}(\mathbf{r},\mathbf{r}')$ is the well-known free-space Green's function, and J(r) denotes the unknown surface current.

For the scattering excited by a plane wave in the homogeneous background medium, the tangential component of the incident magnetic field contains a propagating wave phase dependency, which can be expressed as

$$\mathbf{H}_t^{inc} \sim e^{-j\mathbf{k}^i \cdot \mathbf{r}}, \quad (2)$$

where $\mathbf{k}^i$ is the propagation vector of the incident wave in the background medium. (2) indicates $\nabla \cdot \mathbf{H}_t^{inc} \sim e^{-j\mathbf{k}^i \cdot \mathbf{r}}$. Expressing the tangential component of the total magnetic field as the summation of the tangential component of incident and the scattering magnetic field, and considering the boundary condition that the normal component of magnetic field vanishes on the PEC surface, we have

$$\nabla \cdot \mathbf{H}_t = \nabla \cdot \mathbf{H}_t^{inc} + \nabla \cdot \mathbf{H}_t^{sca} = 0. \quad (3)$$

Hence, the total magnetic field also has the phase dependency. According to the surface equivalence theorem, the induced current, and the total magnetic field satisfy $\mathbf{J} = \hat{\mathbf{n}} \times \mathbf{H}$, thus, it can be concluded that the induced current on the PEC surface has the propagating wave phase property:

$$\mathbf{J}_t^{inc} \sim e^{-j\mathbf{k}^i \cdot \mathbf{r}}. \quad (4)$$

Based on this, a basis function with the propagating wave phase factor is introduced, called phase extracted (PE) basis functions. PE

basis functions can be expressed as the multiplication of an amplitude term and a phase

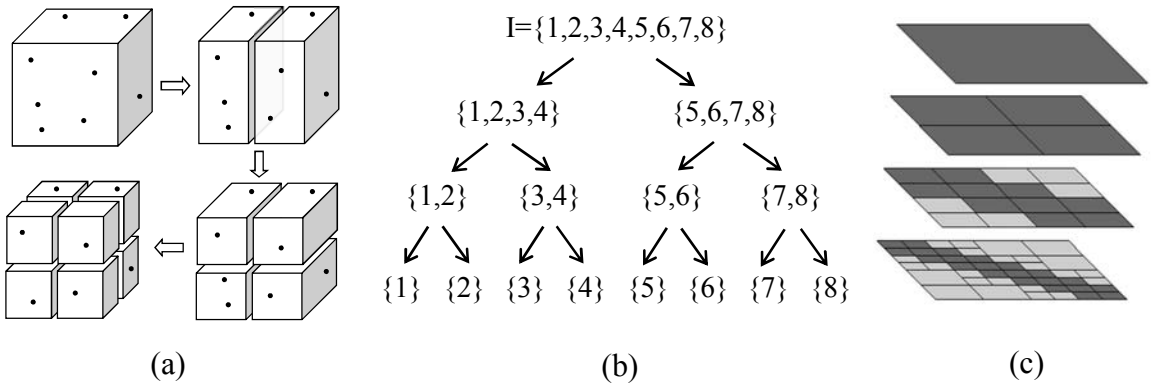

Fig. 1. (a) Subdivision of a finite set using bounding box. " • " denotes the midpoint of each edge. (b) Cluster tree T_I. (c) Block cluster tree $T_{I\times I}$. Admissible leaves are *light grey*.

term. The amplitude term here is chosen as a triangular curvilinear Rao-Wilton-Glisson (CRWG) function in conventional MoM formulation due to its accuracy in representing arbitrary curvilinear surfaces, and the phase term is an exponential function, as follows

$$\mathbf{J}_n(\mathbf{r}) = \mathbf{j}_n(\mathbf{r})e^{-j\mathbf{k}^i\cdot\mathbf{r}}, \tag{5}$$

where $\mathbf{j}_n(\mathbf{r})$ denotes the CRWG basis functions. Thus, the induced current $\mathbf{J}(\mathbf{r})$ can be expanded with the PE basis functions $\mathbf{J}_n(\mathbf{r})$:

$$\mathbf{J}(\mathbf{r}) = \sum_{n=1}^{N} a_n \mathbf{j}_n(\mathbf{r})e^{-j\mathbf{k}^i\cdot\mathbf{r}}. \tag{6}$$

After the phase extraction, the residual part of the basis needs to express the amplitude distribution only. For convex objects with smooth surfaces, the amplitude term of the induced current varies much slower compared with the oscillatory phase term. As a result, they can be defined on much larger patches than the traditional basis functions which do not involve any phase information. Hence, a set of very coarse mesh grid can be used to discretize the objects and the number of basis functions can be reduced dramatically. Away from the smooth region, where the PE basis function becomes invalid, the ordinary discretization density of conventional CRWG basis functions is needed. After Galerkin's testing, the resulting linear system from EFIE formulation can be symbolically rewritten as

$$Ax=b, \tag{7}$$

where A denotes the system matrix with the size being the number of PE basis functions.

B. Construct an $\mathcal{H}$-matrix by hierarchical partitioning

The process of generating an $\mathcal{H}$-matrix representation of the EFIE system matrix A is performed by two main procedures. They are the hierarchical partitioning of the matrix into blocks and the blockwise restriction to low-rank matrices. The hierarchical partitioning is on the basis of a *cluster tree*, i.e., a tree T_I satisfies the following:

- $\mathrm{root}(T_I) = I$,
- if $t \in T_I$ with $\mathrm{sons}(t) \neq \varnothing$, then $t = \bigcup\{t' : t' \in \mathrm{sons}(t)\}$,
- if $t \in T_I$ with $\mathrm{sons}(t) = \varnothing$, then $\#t \le n_{\min}$.

where $I = \{1,2,\ldots\ldots N\}$ is a finite index set of all the PE basis functions, $\#t$ denotes the number of elements in the cluster t and $n_{\min}$ is a predetermined threshold parameter to control the depth of the cluster tree. A simple method for building a cluster tree is bisection based on geometry-based subdivisions of the index sets using bounding boxes. The key idea of this method is to split an index set in the coordinate direction of maximal extent. Figure 1 (a) depicts a simplified subdivision with I including only eight elements, and the resulting binary cluster tree T_I is shown in Fig. 1 (b).

Based on the cluster tree T_I, the index set $I \times I$ corresponding to the system matrix $\mathbf{A} \in \mathbb{C}^{I \times I}$ is split into a partition

$$P = \{t \times s : t, s \in T_I\}, \tag{8}$$

which generates the *block cluster tree* $T_{I \times I}$. To approximate a matrix by a block-wise low-rank approximation, the sub-blocks have to fulfill a so-called admissibility condition as follows

$$\max\{diam(B_t), diam(B_s)\} \le \eta dist(B_t, B_s), \tag{9}$$

where B_t and B_s denotes the minimal bounding box for the support of cluster *t* and *s*, *diam* and *dist* denote the Euclidean diameter and distance of cluster *t* and *s* respectively, and $\eta \in \mathbb{R}^+$ controls the trade-off between the number of admissible blocks. Based on this, the partitioning *P* can be split into admissible ("far-field") and inadmissible ("near-field") blocks described as:

$$P = P^{near} \bigcup P^{far}, \tag{10}$$

with

$$P^{far} = \{t \times s \in P : \text{(9) holds}\}, \tag{11}$$

where admissible blocks can be approximated by low-rank representation in the following Rk-matrices as follows

$$M\big|_{m \times n} = AB^H, \quad A \in \mathbb{C}^{m \times k}, B \in \mathbb{C}^{n \times k}, \tag{12}$$

with *A*, *B* in full matrix representation, and *k* is much smaller than *m* and *n*. The corresponding block cluster tree $T_{I \times I}$ based on the cluster tree T_I of Fig. 1 (b) is given in Fig. 1 (c).

Based on the cluster tree and the block cluster tree, the class of $\mathcal{H}$-matrix for an admissible partitioning *P* and the maximum rank *k* can be defined as

$$\mathcal{H}(P,k) := \left\{A \in \mathbb{C}^{I \times I} : \text{rank}(A|_b) \le k \text{ for all } b \in P\right\}. \tag{13}$$

C. Low-rank approximation using recompressed ACA

In the $\mathcal{H}$-matrix representation, near-field blocks are uncompressed and to be computed via PE-based MoM. Due to the rapid decay of the discrete Green's function, the far-field blocks can be compressed to low-rank representations with little loss of accuracy. To find these low-rank approximations, the adaptive cross approximation (ACA) algorithm is adopted. In this algorithm, the normally dense far-field blocks are approximated by using only a few rows and columns, i.e., crosses of these blocks, while other matrix entries are not required to be calculated. Starting from only one cross and adding more and more crosses, one applies this approximation iteratively until the difference between two consecutive cross-approximations are small enough. Then, the low-rank approximations of the far-field blocks are achieved. Since the ACA theory can be found in the original work of Bebendorf [20,21], the details of it will not be presented in this paper. It is worth noting that the low-rank representation obtained by ACA is not yet optimal in terms of storage requirements. These low-rank blocks can be in fact recompressed, using QR decomposition and the truncated singular value decomposition (SVD), which allows a further storage reduction without accuracy penalties. The process of recompressing a low-rank block $M = AB^H$ to $\tilde{M} = \tilde{A}\tilde{B}^H$ can be performed as follows:

1. Compute a QR decomposition $A = Q_A R_A$, $Q_A \in \mathbb{C}^{m \times k}$, $R_A \in \mathbb{C}^{k \times k}$.
2. Compute a QR decomposition $B = Q_B R_B$, $Q_B \in \mathbb{C}^{n \times k}$, $R_B \in \mathbb{C}^{k \times k}$.
3. Compute a singular value decomposition $R_A R_B^H = U \sum V^H$.
4. Extract $\tilde{\sum} = \text{diag}(\sum_{11}, \sum_{22} \cdots, \sum_{k'k'})$ (first largest k' singular values) with k' satisfies $\sum_{k'k'} > \varepsilon_{\text{ACA}} \sum_{11}$ and $\sum_{(k'+1)(k'+1)} \le \varepsilon_{\text{ACA}} \sum_{11}$, where ε_{ACA} is the relative truncation error.
5. Extract $\tilde{U} = [U_1\ U_2 \cdots U_{k'}]$ (first k' columns), $\tilde{V} = [V_1\ V_2 \cdots V_{k'}]$ (first k' columns).
6. Set $\tilde{A} = Q_A \tilde{U} \tilde{\sum}$ and $\tilde{B} = Q_B \tilde{V}$.

Thus, the construction of an $\mathcal{H}$-matrix is accomplished with its admissible blocks generating from the recompressed ACA technique. A typical structure of an $\mathcal{H}$-matrix in practice is presented in Fig. 2.

D. The recursive scheme for $\mathcal{H}$-LDLT

The $\mathcal{H}$-LDLT decomposition can be implemented recursively starting from a 2×2 block-matrix induced by the hierarchical partitioning. Using the exact LDLT decomposition on the finest level and assuming that the $\mathcal{H}$-LDLT decomposition has already been defined on all finer

levels, the unknown blocks L_{ij}, D_{ii}, and U_{ij} can be solved in the following three steps:

$$\mathcal{H}=\begin{bmatrix}\mathcal{H}_{11} & \mathcal{H}_{12}\\ \mathcal{H}_{21} & \mathcal{H}_{22}\end{bmatrix}=\begin{bmatrix}L_{11} & \\ L_{21} & L_{22}\end{bmatrix}\begin{bmatrix}D_{11} & \\ & D_{22}\end{bmatrix}\begin{bmatrix}L_{11}^{\mathrm{T}} & L_{21}^{\mathrm{T}}\\ & L_{22}^{\mathrm{T}}\end{bmatrix}. \quad (14)$$

1. Compute L_{11} and D_{11} from $\mathcal{H}_{11}=L_{11}D_{11}L_{11}^{\mathrm{T}}$ by an $\mathcal{H}$-LDLT decomposition on the next finer level.
2. Compute L_{21} from $\mathcal{H}_{21}=L_{21}D_{11}L_{11}^{\mathrm{T}}$ by an upper triangular solver.
3. Compute L_{22} and D_{22} from $\mathcal{H}_{22}-L_{21}D_{11}L_{21}^{\mathrm{T}}=L_{22}D_{22}L_{22}^{\mathrm{T}}$ by an $\mathcal{H}$-LDLT decomposition on the next finer level.

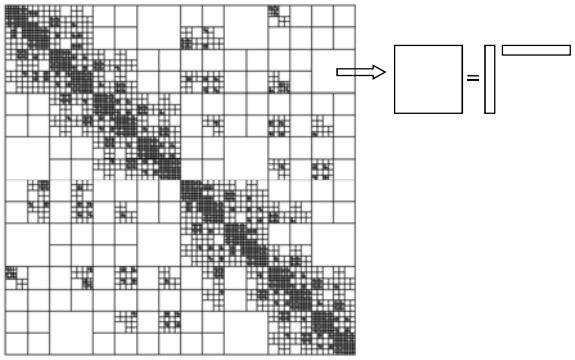

Fig. 2. A typical $\mathcal{H}$-matrix with ACA-based low-rank matrices.

In Step 2 above, an upper triangular solver is needed to solve a upper triangular system, with a given upper triangular matrix $D_{11}L_{11}^{\mathrm{T}}$ and a given right-hand-side matrix $\mathcal{H}_{21}$, simplified as $XU=B$. It can also be solved recursively from

$$\begin{bmatrix}X_{11} & X_{12}\\ X_{21} & X_{22}\end{bmatrix}\begin{bmatrix}U_{11} & U_{12}\\ & U_{22}\end{bmatrix}=\begin{bmatrix}B_{11} & B_{12}\\ B_{21} & B_{22}\end{bmatrix}. \quad (15)$$

in the following four steps:

1. Compute X_{11} from $X_{11}U_{11}=B_{11}$ by an upper triangular solver on the next finer level.
2. Compute X_{21} from $X_{21}U_{11}=B_{21}$ by an upper triangular solver on the next finer level.
3. Compute X_{12} from $X_{12}U_{22}=B_{12}-X_{11}U_{12}$ by an upper triangular solver on the next finer level.
4. Compute X_{22} from $X_{22}U_{22}=B_{22}-X_{21}U_{12}$ by an upper triangular solver on the next finer level.

In all these steps for the $\mathcal{H}$-LDLT decomposition and the upper triangular solver, the exact addition and multiplication are replaced by the faster formatted $\mathcal{H}$-matrix counterparts ($\oplus$ and $\otimes$). Truncation operator $\mathcal{T}_{k\leftarrow k'}^{\mathcal{H}}$ based on truncated versions of the *QR*-decomposition and singular value decomposition (SVD) is used to define the $\mathcal{H}$-matrix addition $A\oplus B=\mathcal{T}_{k\leftarrow 2k}^{\mathcal{H}}(A+B)$ and the $\mathcal{H}$-matrix multiplication $A\otimes B=\mathcal{T}_{k\leftarrow k'}^{\mathcal{H}}(A\times B)$. In this paper, an adaptive truncation scheme with a relative truncation error $\varepsilon_{\mathcal{H}}$ is adopted, similarly defined as $\varepsilon_{\mathrm{ACA}}$. It should be noted that matrix D is the diagonal matrix with little additional storage consumption. $\mathcal{H}$-LDLT can be performed in $O(k^2N\log^2N)$ computational complexity and $O(kN\log N)$ storage requirement with blockwise rank k. After the completion of $\mathcal{H}$-LDLT decomposition, $\mathcal{H}$-matrix formatted forward and backward substitutions ($\mathcal{H}$-FBS) are implemented to obtain the solution x of equation (3) with $O(kN\log N)$ computational complexity [26]. If the right-hand-side matrix B is replaced by a vector b, the process of solving (15) is the backward substitution, while the forward case is similar.

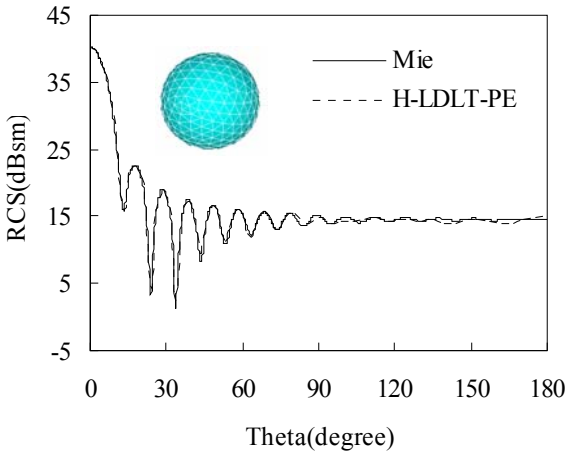

Fig. 3. Bistatic RCS of the sphere.

III. NUMERICAL RESULTS

In order to demonstrate the performances of the proposed method for 3D electrically large scattering problems, a variety of arbitrarily shaped objects are simulated. In these examples, scatters are all excited by the plane wave. The relative truncation error of ACA is set to be $\varepsilon_{\mathrm{ACA}}=10^{-3}$. The computations of the examples in this section are performed on a common PC with Intel Core2 2.8GHz CPU and 8GB RAM in double precision.

Table 1: Comparison of the computational costs for different methods

Method	Matrix construction		LDLT manipulation	
	Mem (MB)	Time (s)	Mem (MB)	Time (s)
MoM-LDLT	1.0×10^4	-	$>1.0\times10^4$	$>1.0\times10^5$
MoM-LDLT-PE	6.6	3.2	11.3	6.6
$\mathcal{H}$-LDLT	897.4	532.9	1054.6	1227.1
$\mathcal{H}$-LDLT-PE	4.4	9.6	4.9	3.9
Improvement Ratio	204.0	55.5	215.2	314.6

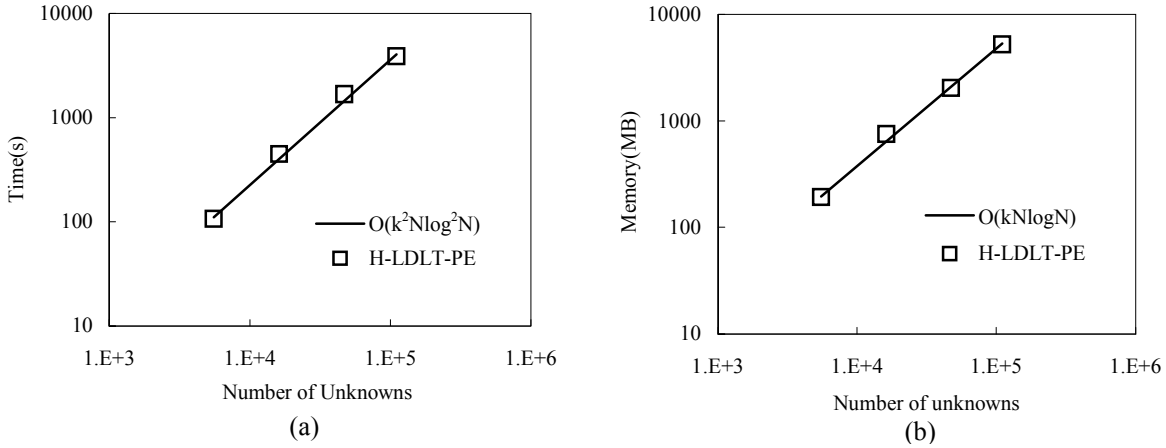

Fig. 4. The complexity tests of the $\mathcal{H}$-LDLT-PE with the number of unknowns increasing. (a) Time required for the $\mathcal{H}$-LDLT decomposition. (b) Memory required for $\mathcal{H}$-LDLT factors.

For simplification, the proposed method is referred to as the $\mathcal{H}$-LDLT-PE method.

The first example deals with the problem of scattering from a PEC sphere with a radius of 3*m*. A plane wave is incoming in the direction $\theta=0^\circ$ and $\phi=0^\circ$ at a frequency of 300MHz. The conventional MoM solution may need 36,273 unknowns due to 0.1λ patch size. The proposed $\mathcal{H}$-LDLT-PE method needs only 927 unknowns since a patch size of about 0.6λ is achieved by using PE basis functions. The bistatic RCS is computed by the $\mathcal{H}$-LDLT-PE method and compared with the exact Mie series solution on the plane $\phi=0^\circ$. Very good agreement can be observed in Fig. 3. Direct solution of this example by conventional MoM on a common PC is an impossible mission, since a memory usage of about 10.0GB is required to store the impedance matrix and a rapid increase would occur in the direct solution. The bald ACA-based $\mathcal{H}$-LDLT method can reduce the total memory requirement for entire direct solution to about 2.0GB. By using the $\mathcal{H}$-LDLT-PE method, the computational costs can be further reduced dramatically. Table 1 shows the computational requirements of the MoM-based LDLT decomposition and presents the computational costs of the $\mathcal{H}$-LDLT method and the $\mathcal{H}$-LDLT-PE method for building an $\mathcal{H}$-matrix representation based on recompressed ACA and implementing the $\mathcal{H}$-LDLT decomposition under $\varepsilon_{\mathcal{H}}=10^{-3}$. The improvement ratio is also presented which validates the ability of the $\mathcal{H}$-LDLT method can be further improved by the $\mathcal{H}$-LDLT-PE method. Besides, we adopt the MLFMM combined with GMRES iteration to solve this problem. According to our test, 203.6MB memory usage and 19.2s CPU time usage are required for the construction of the

Table 2: Computational costs of the $\mathcal{H}$-LDLT-PE method for different $\varepsilon_{\mathcal{H}}$

$\mathcal{H}$-matrix construction		$\mathcal{H}$-LDLT manipulation		
Mem (MB)	Time (s)	$\varepsilon_{\mathcal{H}}$	Mem (MB)	Time (s)
520.4	624.6	5e-1	308.9	121.5
		1e-1	398.6	213.4
		1e-2	555.7	459.3
		1e-3	669.3	689. 5
		1e-4	785.2	877. 6

impedance matrix, and 582.39s CPU time is needed for the GMRES iterative solution with 10^{-3} residual norm.

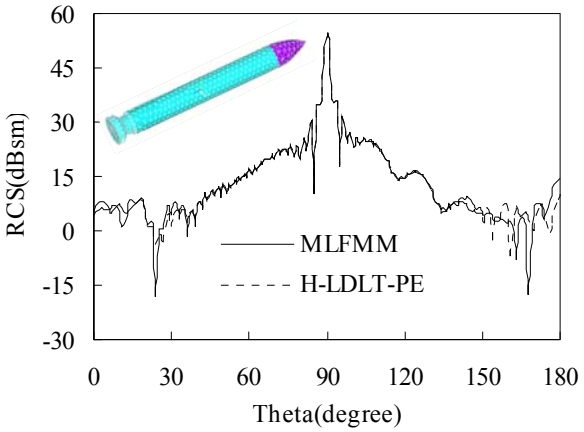

Fig. 5. Bistatic RCS of the missile.

It can be found that the $\mathcal{H}$-LDLT-PE has obvious advantages in the competition. Finally, the computational costs of the $\mathcal{H}$-LDLT-PE method are tested with the unknown number increasing from 5,531 to 110,362. As shown in Fig. 4 (a) and (b), the CPU time and memory usages are validated to be very close to $O(k^2 N \log^2 N)$ and $O(k N \log N)$, respectively.

The second example considers the scattering from a missile with a total length of $12.5m$ and a radius of $3m$ at the main body. The incident plane wave propagates from the direction $\theta = 90^\circ$ and $\phi = 0^\circ$ at 1 GHz. The conventional MoM solution needs 146,694 unknowns by using 0.1λ patch size, while the proposed $\mathcal{H}$-LDLT-PE method needs only 17,082 unknowns by using 0.6λ patch size at the smooth region of the missile. The bistatic RCS computed by the $\mathcal{H}$-LDLT-PE method on the plane $\phi = 0^\circ$ agrees very well with the results calculated by the MLFMM, as depicted in Fig. 5. Table 2 shows the computational costs for the construction of an $\mathcal{H}$-matrix and the $\mathcal{H}$-LDLT manipulation. The $\mathcal{H}$-LDLT-PE method not only provides an efficient solution of EFIE, but also can control the computational accuracy flexibly by different choices of the relative truncation error $\varepsilon_{\mathcal{H}}$ in the formatted $\mathcal{H}$-matrix arithmetic. Different $\varepsilon_{\mathcal{H}}$ requires different memory and CPU time usage, as shown in Table 2, and leads to different RCS error. Fig. 6 presents the RCS error integrated over all directions and normalized by the appointed accurate RCS calculated under $\varepsilon_{\mathcal{H}} = 10^{-8}$, without taking the truncation error of ACA into consideration. Since the parts of the top and bottom of this missile are not smooth, finer discretization can be employed for more accurate RCS, while the coarse discretization can be retained at the body of this missile without loss of accuracy. It is obvious that the direct solution of this 37λ problem based on MoM is drastically impossible, and the $\mathcal{H}$-LDLT method can hardly be performed on a common PC though the computational cost has been dramatically reduced. However, the $\mathcal{H}$-LDLT-PE method can be easily performed on a common PC at a very low cost as show in Table 2. For this example, the MLFMM requires 812.4MB memory and 192.6s CPU time to construct the impedance matrix, and 5410.6s CPU time to perform the GMRES iterations. Compared with the $\mathcal{H}$-LDLT-PE, although the MLFMM needs less construction time, it spends much more time for the iterative solution due to the slow convergence rate.

Finally, the scattering from a bent rectangular plate of $14m \times 7m$ is analyzed at 1 GHz. The plate

is bent leading to a dihedral conforming a wedge with an interior angle of 90°. The incident elevation angle is $\theta = 90^\circ$ and $\phi = 135^\circ$. A patch size of about 0.8λ is employed at the smooth region of the plate, which leads to only 27,189 unknowns. The bistatic RCS computed by the proposed $\mathcal{H}$-LDLT-PE method on the plane $\theta = 90^\circ$ is plotted together with the results of the MLFMM in Fig. 7. Table 3 shows the computational costs of the $\mathcal{H}$-LDLT-PE method under $\varepsilon_{\mathcal{H}} = 10^{-3}$. Obviously, the computational costs are extremely low by using the $\mathcal{H}$-LDLT-PE method, while the direct solution of this 42λ problem with 373,956 unknowns under the traditional 0.1λ patch size can hardly be accomplished on a common PC. For this problem, the MLFMM requires 1899.4MB memory and 366.9s CPU time to construct the impedance matrix, and 2796.8s

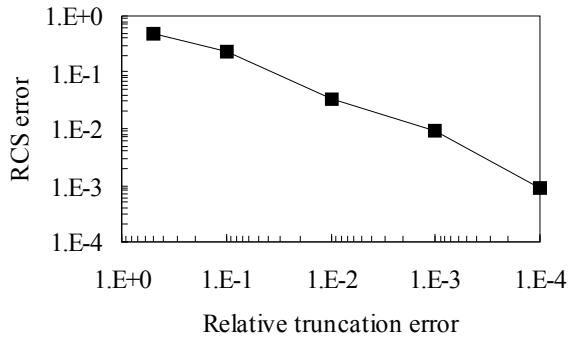

Fig. 6. Change of the RCS error with $\varepsilon_{\mathcal{H}}$ decreasing.

approximation technique with a recompression scheme is exploited to build the data-sparse representation of an $\mathcal{H}$-matrix, yielding a kernel-independent method. The $\mathcal{H}$-LDLT algorithm provides an inexpensive but sufficiently accurate way to compute and store the approximate triangular factor of the EFIE system matrix in nearly optimal complexity. The accuracy of the $\mathcal{H}$-LDLT is controllable by different choices of the relative truncation error, leading to different computational costs. PE basis function is employed to further reduce the memory and CPU time required for the $\mathcal{H}$-LDLT by introducing propagating wave phase dependence. Numerical results demonstrate the proposed method is robust for electrically large scattering problems.

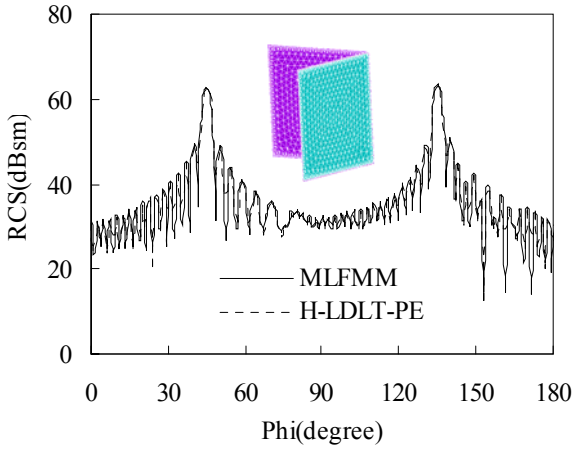

Fig. 7. Bistatic RCS of the bent rectangular plate.

Table 3: Computational costs of the $\mathcal{H}$-LDLT-PE method

$\mathcal{H}$-matrix construction		$\mathcal{H}$-LDLT manipulation	
Mem (MB)	Time (s)	Mem (MB)	Time (s)
631.1	842.5	855.7	860.2

$\varepsilon_{\mathcal{H}}$

CPU time to complete the GMRES iterative solution. It can be found that the $\mathcal{H}$-LDLT-PE defeats the MLFMM in overall computational costs, which demonstrate the capability of the H-LDLT-PE.

IV. CONCLUSION

A new direct method based on the $\mathcal{H}$-LDLT algorithm and PE basis functions is presented for the MoM solution of EFIE. The adaptive cross

ACKNOWLEDGMENT

We would like to thank the support of the Natural Science Foundation of 60871013, Jiangsu Natural Science Foundation of BK2008048.

REFERENCES

[1] S. M. Rao, D. R. Wilton, and A. W. Glisson, "Electromagnetic Scattering by Surfaces of Arbitrary Shape," *IEEE Trans. Antennas Propag.*, vol. 30, 409-418, 1982.

[2] S. M. Rao and R. F. Harrington, *Field Computation by Moment Methods*. New York: Macmillan, 1968.

[3] W. C. Chew, J. M. Jin, E. Midielssen, and J. M. Song, *Fast and Efficient Algorithms in Computational Electromagnetics*, Boston, MA: Artech House, 2001.

[4] J. M. Song, C. C. Lu, and W. C. Chew, "Multilevel Fast Multipole Algorithm for Electromagnetic Scattering by Large Complex Objects," *IEEE Trans. Antennas Propag.*, vol. 45, pp. 1488-1493, 1997.

[5] R. S. Chen, Z. H. Fan, Y. Y. An, M. M. Zhu, and K. W. Leung, "Modified Adaptive Cross Approximation Algorithm for Analysis of Electromagnetic Problems," *Applied Computational Electromagnetic Society (ACES) Journal*, vol. 26, no. 2, pp. 160-169, February 2011.

[6] H. Chen, Z. H. Fan, R. S. Chen, Z. N. Jiang, and M. M. Li, "Adaptive Mixed-Form Fast Multipole Method for the Analysis of Electromagnetic Scattering," *Applied Computational Electromagnetic Society (ACES) Journal*, vol. 25, no. 11, pp. 962-974, November 2010.

[7] Y. Saad, *Iterative Methods for Sparse Linear Systems*. New York: PWS Publishing, 1996.

[8] Michele Benzi, "Preconditioning Techniques for Large Linear Systems: A Survey", *Journal of Computational Physics*, 182, pp. 418-477, 2002.

[9] C. Delgado, E. García, F. Felipe Cátedra, and R. Mittra, "Application of the Characteristic Basis Function Method for the Electromagnetic Analysis of Electrically Large and Complex Bodies," *Applied Computational Electromagnetic Society (ACES) Journal*, vol. 24, no. 2, pp. 189-203, April 2009.

[10] K. R. Aberegg and A. F. Peterson, "Application of the Integral Equation-Asymptotic Phase Method to Two-Dimensional Scattering," *IEEE Trans. Antennas Propagat.*, vol. 43, pp. 534-537, 1995.

[11] J. M. Taboada, F. Obelleiro, J. L. Rodriguez, I. Garcia-Tunon, and L. Landesa, "Incorporation of Linear-Phase Progression in RWG Basis Functions," *Microwave and Optical Technology Letters*, vol. 44, no. 2, pp. 106-112, 2005.

[12] R. J. Burkholder, Ç. Tokgöz, C. J. Reddy, and W. O. Coburn, "Iterative Physical Optics for Radar Scattering Predictions," *Applied Computational Electromagnetic Society (ACES) Journal*, vol. 24, no. 2, pp. 241–258, April 2009.

[13] D. H. Kwon, R. J. Burkholder, and P. H. Pathak, "Efficient Method of Moments Formulation for Large PEC Scattering Problems using Asymptotic Phase Front Extraction (APE)," *IEEE Trans. Antennas Propag*, vol. 49, no. 4, pp. 583-591, 2001.

[14] Z. Nie, S. Yan, S. He, and J. Hu, "On the Basis Functions with Propagating Wave Phase Factor for Efficient Analysis of Scattering from Electrically Large Targets," *Progress In Elec-tromagnetics Research*, vol. 85, pp. 83-114, 2008.

[15] S. Yan, S. He, Z. Nie, and J. Hu, "Simulating Wide Band Radar Response from PEC Targets using Phase Extracted Basis Functions," *Progress In Electromagnetics Research*, vol.13, 409-431, 2009.

[16] W. Hackbusch, "A Sparse Matrix Arithmetic Based on $\mathcal{H}$-matrices. I. Introduction to $\mathcal{H}$-matrices," *Computing*, 62(2): pp. 89-108, 1999.

[17] S. Le Borne, "$\mathcal{H}$-Matrices for Convection-Diffusion Problems with Constant Convection," *Computing*, vol. 70, pp. 261-274, 2003.

[18] W. Chai and D. Jiao, "A $\mathcal{H}$-Matrix-Based Method for Reducing the Complexity of Integral-Equation-Based Solutions of Electromagnetic Problems," *IEEE International Symposium on Antennas and Propagation*, 2008.

[19] W. Hackbusch and B. Khoromskij, "A Sparse $\mathcal{H}$-Matrix Arithmetic. Part II: Application to Multi-Dimensional Problems," *Computing*, vol. 64, pp. 21-47, 2000.

[20] M. Bebendorf, "Approximation of Boundary Element Matrices," *Numer. Math.*, no. 86, pp. 565-589, 2000.

[21] M. Bebendorf and S. Rjasanow, "Adaptive Low-Rank Approximation of Collocation Matrices," *Computing*, vol. 70, no. 1, pp. 1-24, 2003.

[22] K. Z. Zhao, M. N. Vouvakis, and J. F. Lee, "The Adaptive Cross Approximation Algorithm for Accelerated Method of Moments," *IEEE Trans. Electromagn. Compat.*, vol. 47, no. 4, pp. 763-773, 2005.

[23] Z. N. Jiang, Z. H. Fan, D. Z. Ding, R. S. Chen, and K. W. Leung, "Preconditioned MDA-SVD-MLFMA for Analysis of Multi-Scale Problems," *Applied Computational Electromagnetic Society (ACES) Journal*, vol. 25, no. 11, pp. 914-925, November 2010.

[24] W. Hackbusch and Z. P. Nowak, "On the Fast Matrix Multiplication in the Boundary Element Method by Panel Clustering," *Numer. Math.*, vol. 54, pp. 463-491, 1989.

[25] S. Börm and W. Hackbusch, "$\mathcal{H}2$-Matrix Approximations of Integral Operators by Inter-Polation," Appl. Numer. Math., vol. 43, pp. 129-143, 2002.

[26] L. Grasedyck and W. Hackbusch, "Construction and Arithmetics of $\mathcal{H}$-Matrices," *Computing*, vol. 70, no. 4, pp. 295-344, 2003.

Ting Wan was born in Huanggang, Hubei, China. He received the B.S. and M.S. degrees in Electrical Engineering from Nanjing University of Science and Technology (NJUST), Nanjing, China, in 2003 and 2006, respectively. He is currently working toward the Ph.D. degree in the Department of Communication Engineering at NJUST. His research interests include computational electromagnetics, antennas, and microwave integrated circuits.

Rushan Chen was born in Jiangsu, China. He received his B.S. and M.S. degrees from the Dept. of Radio Engineering, Southeast University, in 1987 and in 1990, respectively, and his Ph.D. from the Dept. of Electronic Engineering, City University of Hong Kong in 2001. Since September 1996, he has been a Visiting Scholar with the Department of Electronic Engineering, City University of Hong Kong, first as Research Associate, then as a Senior Research Associate in July 1997, a Research Fellow in April 1998, and a Senior Research Fellow in 1999. From June to September 1999, he was also a Visiting Scholar at Montreal University, Canada. In September 1999, he was promoted to Full Professor and Associate Director of the Microwave & Communication Research Center in NJUST and in 2007, he was appointed Head of the Dept of Communication Engineering, Nanjing University of Science & Technology. His research interests mainly include microwave/millimeter-wave systems, measurements, antenna, RF-integrated circuits, and computational electro-magnetics. He is a Senior Member of the Chinese Institute of Electronics (CIE). He received the 1992 third-class science and technology advance prize given by the National Military Industry Department of China, the 1993 third class science and technology advance prize given by the National Education Committee of China, the 1996 second-class science and technology advance prize given by the National Education Committee of China, and the 1999 first-class science and technology advance prize given by JiangSu Province as well as the 2001 second-class science and technology advance prize. At NUST, he was awarded the Excellent Honor Prize for academic achievement in 1994, 1996, 1997, 1999, 2000, 2001, 2002, and 2003. He has authored or co-authored more than 200 papers, including over 140 papers in international journals. He is the recipient of the Foundation for China Distinguished Young Investigators presented by the National Science Foundation (NSF) of China in 2003. In 2008, he became a Chang-Jiang Professor under the Cheung Kong Scholar Program awarded by the Ministry of Education, China.

Xiaoqing Hu was born in Hubei, China, in June 1981. He received the B.S. and M.S. degrees in Applied Mathematics from Jilin University, Jilin, China, in 2004 and 2007, respectively. He is currently working toward the Ph.D. degree at Nanjing University of Science and Technology, Jiangsu, China. His research interests include integral equation and its fast methods.

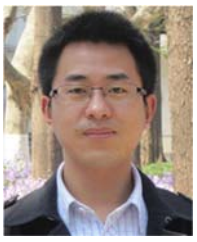

Yilin Chen was born in Jiangsu Province, the People's Republic of China. He is currently working toward the M.S. degree in the Department of Communication Engineering at Nanjing University of Science and Technology, Nanjing, China. His research interests include computational electromagnetics, antennas and microwave integrated circuits.

Yijun Sheng was born in Jiangsu Province, the People's Republic of China. He received the M.S. degree in Physics from Nanjing University of Science and Technology (NJUST) in 2003, and is currently working toward the Ph.D. degree in the Department of Communication Engineering at NJUST, Nanjing, China. His research interests include compu-tational electromagnetics, antennas, and microwave integrated circuits.

Scan Blindness Elimination Using Composite Defected Ground Structures and Edge-coupled Split Ring Resonators

Ming-Chun Tang[1], Shaoqiu Xiao[1], Chang-Jin Li[2], Chaolei Wei[1], and Bingzhong Wang[1]

[1] The Institute of Applied Physics
University of Electronic Science and Technology of China, Chengdu, 610054, China
tmc_212@163.com, xiaoshaoqiu@uestc.edu.cn, weichaolei@126.com, bzwang@uestc.edu.cn

[2] Engineering and Technology College of Neijiang Normal University
Neijiang, 641112, China
lcj2255628@126.com

Abstract-A novel compact composite structure, composed of double-U shaped defected ground structure (DGS) and edge-coupled split ring resonator (E-SRR), is presented in this paper. The composite structure is integrated into microstrip array to reduce the interelement mutual coupling, with the aim to eliminate the scan blindness and improve the scanning performance. The three kinds of two-element arrays (without composite structure, with only DGS and with composite structure) are thoroughly simulated, measured, and compared. The results show that, the reduction in mutual coupling of 11 dB between elements in E-plane is obtained with the use of composite structure. It is worth mentioning that, approximately 2dB gain improvement and 2.4dB side lobe suppression are both attained, in comparison with the array with only DGSs. Finally, the scan properties of three kinds of infinite microstrip phased arrays are studied by the waveguide simulator method. The results indicate that the scan blindness in an infinite microstrip phased array can be well eliminated by virtue of the effect of the proposed composite structures, in accordance with results obtained by active patterns of the centre element in 9×5 array.

Index Terms ─ DGS, edge-coupled SRR, scan blindness elimination.

I. INTRODUCTION

In infinite microstrip phased arrays, scan characteristic is very poor by reason of the occurrence of unwanted scan blindness when the interelement distance is between $\lambda_0/2$ and λ_0 (the operating wavelength in free space). Due to the scan blindness induced by strong surface waves, the effective methods, such as loading electromagnetic band-gap (EBG) structures and mu-negative (MNG) metamaterial between the elements, have been used extensively [1-4] to eliminate scan blindness. However, these structures witness some intrinsic defects, such as suffering complicated and high-cost designs, taking much spacing, and being of little mechanical robustness. Recently, compact DGSs of simple and low-cost design are utilized into microstrip phased array design [5] instead. Meanwhile, the etched DGS at ground plate leads to inevitable backward radiation through the DGS slot, which worsens the radiation characteristic of the whole array seriously.

To maintain the excellent capability of DGS in surface wave suppression and suppress backward radiation simultaneously, a novel compact composite structure composed of double-U shaped DGS and E-SRR is proposed to load on the infinite microstrip array to ensure high scanning performance in this paper. This paper is organized as follows: Section II firstly shows the novel double-U shaped DGS and E-SRR and analyzes their particular characteristics, respectively. Section III analyzes the influence of proposed composite structure on suppression of surface wave and backward radiation in a two-element array. Finally, the simulated results based on waveguide simulator are presented and

Submitted On: April 1, 2011
Accepted On: May 3, 2011

discussed in Section IV, demonstrating that the scan blindness is also well eliminated, in comparison with the array with only DGSs. Especially, centre active-element patterns in a 9×5 array validate its irreplaceable performance of mutual coupling suppression and gain improvement, and the result further indicates the proposed composite structure is quite suitable for practical application because of its compact structure and good mechanical robustness.

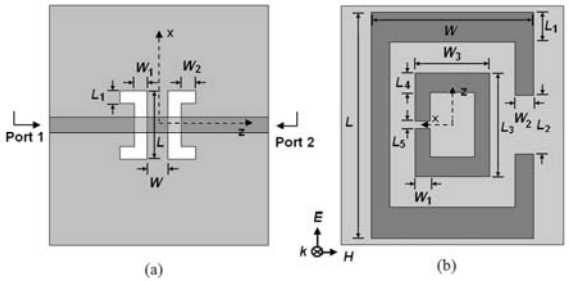

Fig. 1. Configuration of double-U shaped DGS and E-SRR. (a) Double-U Shaped DGS; The parameters: *L= 8.7mm, L_1= 1.6mm, W= 2.6mm, W_1=1.6 mm, W_2= 1.8mm*. (The white parts indicate the slots etched in the ground plate, the grey parts indicate the ground plate, and dark grey parts indicate the microstrip transmission line.) (b) E-SRR; The parameters: *L=4.34mm, L_1= 0.585mm, L_2=1.14mm, L_3=2mm, L_4= 0.37mm, L_5=0.14mm, W=3.11mm, W_1=0.285mm, W_2=0.355mm, W_3=1.43mm*, the unit cell *x×y×z=7.45mm×7.45mm×7.45mm*. (The grey parts indicate the substrate, and the dark grey parts indicate the metal.)

II. CHARACTERISTICS OF DOUBLE-U SHAPED DGS AND E-SRR, RESPECTIVELY

The Ansoft HFSS, an electromagnetic simulator based on the finite element method (FEM), is used to carry out all simulations in this paper. The compact double-U shaped DGS is shown in Fig. 1(a). It is etched in the ground plane under the microstrip substrate, and the substrate of 2mm thick has the dielectric constant of 10.2. A 50Ω microstrip transmission line is used to weigh the characteristics of the DGS. The DGS can be modeled by an *L-C* resonator loaded on the transmission line. Naturally, its resonance frequency (rejection band) is also determined by $\omega = 1/\sqrt{LC}$ according to literatures [5, 6]. Particularly, we will analyze the resonance mechanism of this type DGS and report its performance in details in a separate paper in future. The simulation results of the DGS are shown in Fig. 2. It is observed that the -10dB stopband between 5.25GHz and 6.48GHz is obtained. Especially, the -44dB rejection level is achieved near 5.5GHz in the stopband, which demonstrate its excellent rejection performance.

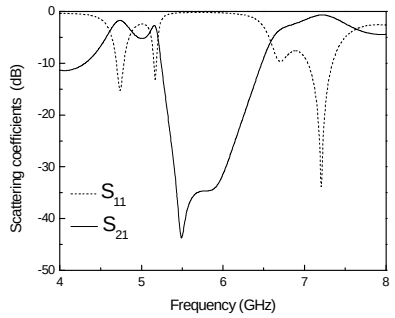

Fig. 2. Simulated scattering coefficients for configuration of double-U shaped DGS in Fig. 1(a).

On the other hand, metamaterials have been extensively investigated recently [7-11]. Figure 1(b) gives a rectangle E-SRR structure metamaterial unit and the description of the corresponding EM environment. In this environment, the EM wave propagates perpendicularly to the E-SRR plane with the electric field *E* polarized parallel to the E-SRR plane and perpendicularly to the E-SRR splitting gap. Thus, the electric excitation is induced by an external electric field *E*, in respect that *E* is polarized perpendicularly to the SRR splitting gap [12-15]. Accordingly, the E-SRR can block electromagnetic wave propagating near its resonant frequency [14, 15]. It is noted that, there is no external magnetic excitation in this structure [16, 17] due to the fact that the magnetic field (*H*) is polarized parallel to SRR plane. Therefore, the E-SRR can demonstrate response to the external electric field *E* and the block electromagnetic wave propagating near its resonant frequency [15-17]. Moreover, it is worth mentioning that, since there is no symmetry plane normal to the *y*-axis, magneto-electric coupling also occurs and produces magnetic response in the direction of propagation [15]. The E-SRR structure performance is also simulated and the results are shown in Fig. 3(a).

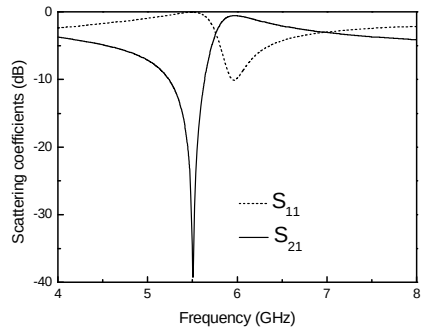

(a)

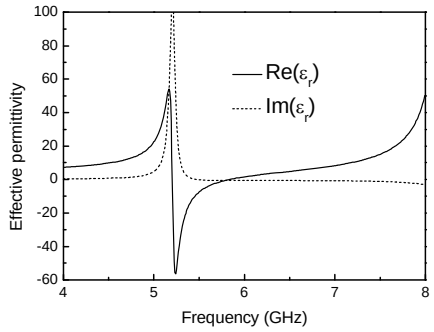

(b)

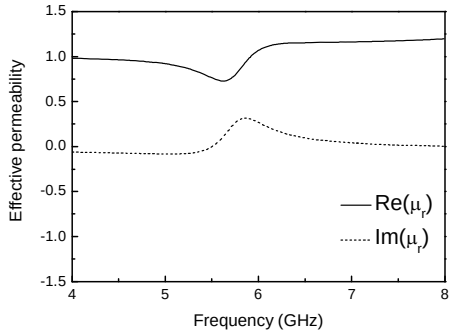

(c)

Fig. 3. Simulated scattering coefficients and retrieved effective permittivity and permeability of configuration E-SRR in Fig. 1(b); (a) simulated scattering coefficients, (b) retrieved effective permittivity, and (c) retrieved effective permeability.

The -10dB stopband between 5.25GHz and 5.64GHz is easily obtained, especially -39dB rejection level achievement near 5.4GHz, even though the dimension is much smaller than wavelength. Moreover, the effective permittivity and permeability are extracted by the Nicolson-Ross-Weir (NRW) method [18], and the values are listed in Fig. 3(b) and (c), respectively. Obviously, there is a certain region above the resonant frequency (5.3GHz) where the E-SRR exhibits negative permittivity of a large value (in Fig. 3(b)) and positive permeability with the integer value despite of slight variations (in Fig. 3(c)), which validates its electric response. Thus, it is promising that the proposed E-SRR could provide required stopband by adjusting the metallic part dimensions in Section III.

III. MUTUAL COUPLING REDUCTION BASED ON COMPOSITE STRUCTURE

Physically small microstrip array exhibits wide application by virtue of its excellent inherent characteristic of simple structure, light weight, small volume, low cost, and so on [4, 19]. However, mutual coupling between elements in a microstrip array, as one of the major sources of degradation in an array performance, limits its extensive application in a high-density package. Previous studies indicated that mutual coupling between the *E*-plane-coupled elements is much stronger than that between the *H*-plane-coupled elements, since stronger surface wave is excited along the *E*-plane [19-22]. Therefore, mutual coupling suppression between the *E*-plane-coupled elements is discussed in this section to demonstrate the excellent performance of the proposed composite structures.

A. Traditional two-element array analysis

In this section, a traditional two-element *E*-coupled microstrip array with the interelement distance between $\lambda_0/2$ and λ_0 is presented as an example. Figure 4 shows the layout of a two-element microstrip array with an operating frequency of 5.4GHz. The size of the two patches is $7.7mm \times 6.7mm$, and the interelement distance is $37.1mm$ corresponding to $0.65\lambda_0$ at the operating frequency. Each patch is excited on its symmetrical axis by a coaxial probe with a distance 1.05 mm away from the patch centre. A $2mm$ thick Rogers RT/duroid 6010/6010LM (tm) substrate ($70mm \times 140mm$) with the relative permittivity ε_r=10.2 is selected to support the patches.

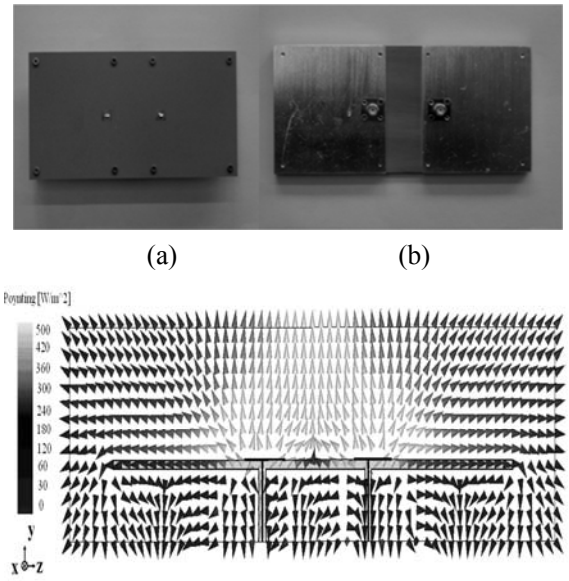

Fig. 4. Configuration of a traditional two-element array; (a)front view, (b) back view, (c) simulated poynting vector distribution in side view, when two antenna operating.

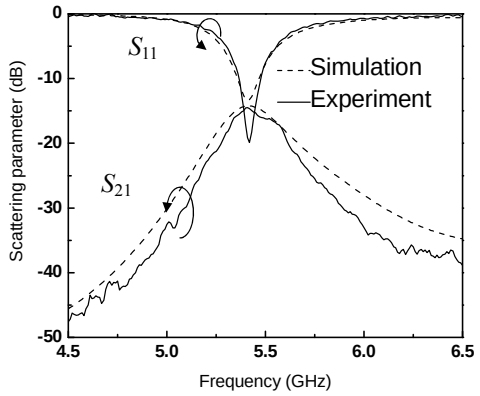

Fig. 5. Simulated and experimentally measured input matching (S_{11}) and mutual coupling (S_{21}) of the two patches in Fig. 4.

As shown in the previous literatures [4, 20-23], strong mutual coupling occurs between adjacent elements, on account of pronounced surface wave excited in the grounded high-permittivity substrate. The simulated and experimentally measured results are shown in Figs. 5 and 6. At the operation frequency 5.4GHz, the measured interelement mutual coupling of -14.5dB is observed, and the gain pattern of the array is not smooth and two deep ripples appear, because of the prominent influence of the strong mutual coupling [5]. Moreover, the good front-to-back ratio of the gains of 22.3dB is measured, which validates the simulated results in Fig. 4(c), i.e., most of the EM energy is radiated in the upper free apace, while the negligible back radiation is observed.

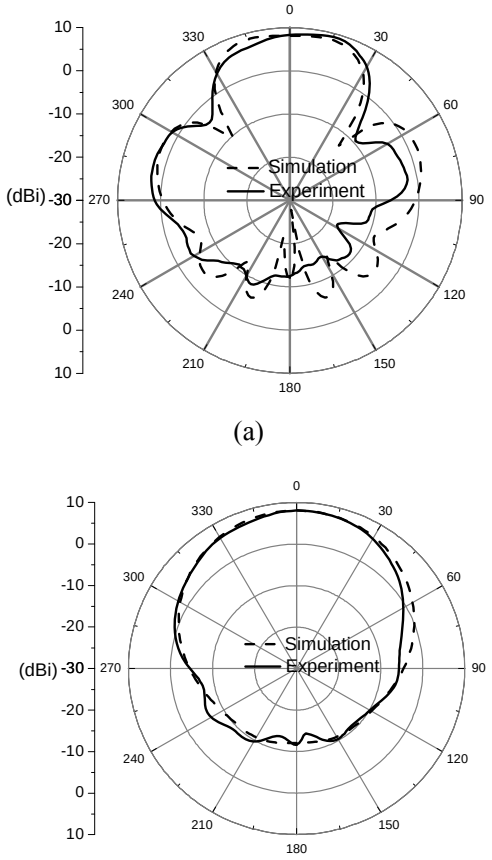

Fig. 6. Simulated and experimentally measured gain patterns of the traditional array in Fig. 4; (a) in *E*-plane, (b) in *H*-plane.

B. Mutual coupling suppression using only DGS in two-element array

To suppress strong mutual coupling, the DGS (here, the double-U shaped DGS in Fig. 1(a) is selected as an example) is etched at the centre of the ground plate between the adjacent elements in *E*-plane, shown in Fig. 7. As aforementioned in Section II, the etched DGS has the inherent property

of rejection to suppress surface wave restricted within substrate [5]. When it is integrated into the array, it could bring about predominant reduction in mutual coupling for the array. Figure 8 demonstrates that mutual coupling (S_{21}) drops drastically below -25dB around operation frequency 5.4GHz, especially -39.3dB achievement at 5.39GHz in experimental results. Obviously, it also illustrates that the DGS exhibits an excellent performance in mutual coupling reduction.

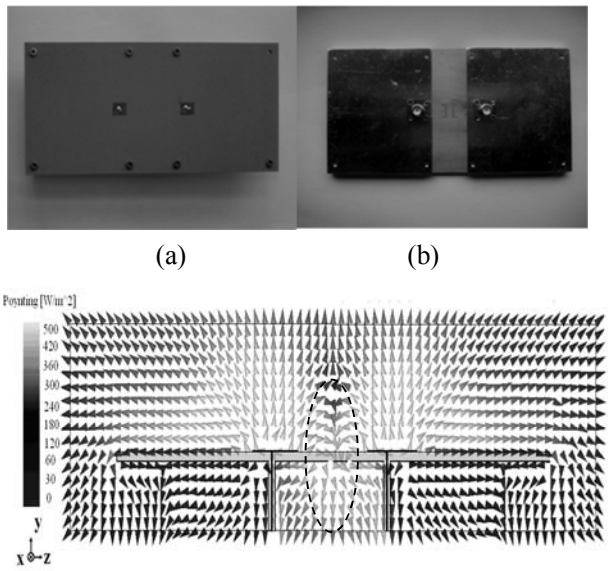

(a) (b)

(c)

Fig. 7. Configuration of a two-element array with double-U shaped DGS; (a) front view, (b) back view, (c) simulated poynting vector distribution in side view.

However, the etched DGS brings adverse impact on the array in Fig. 7, which incurs some EM energy, which should be radiated in the upward free space (in Fig.4(c)), leaking into the backward space through the etched DGS-slots shown in Fig. 7(c). Compared with the poynting vector distributions in Fig. 4(c), a certain energy in the upward space turns towards the backward space (in Fig. 7(c)), which results in much decrease of upward radiation and severe increase of backward radiation. In order to further illustrate its noteworthy defect, Fig. 9 shows experimentally measured gain pattern results together with the simulated one, and they both validate the influence of the DGS on radiation performance of the array. In details, the DGS makes the radiation pattern obviously smooth because of its performance in dramatic mutual coupling reduction. Unfortunately, this improvement is achieved at the cost of the 2.5dB peak gain reduction, 15.9dB back lobe gain increase, and 4dB front-to-back ratio of the gains achievement, in contrast with the array without DGS.

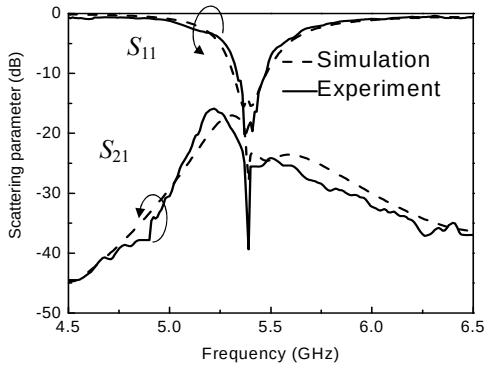

Fig. 8. Simulated and experimentally measured input matching (S_{11}) and mutual coupling (S_{21}) of the two patches in Fig. 7.

C. Gain improvement using composite DGS and E-SRRs in two-element array

As it has been already mentioned in Section III(B), a certain EM wave is propagating through the slots due to the etched DGS. Furthermore, the electric field (*E*-field) distribution at the interface of upward free space and substrate is also simulated in Fig. 10. It is easily seen that a strong *E*-field region appearance above the slots (labeled in the dotted ellipse), which is predominantly polarized in the *z*-axis direction.

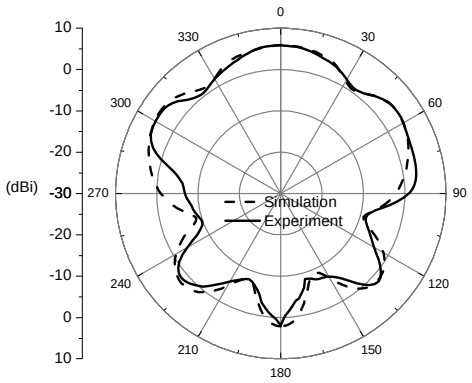

(a)

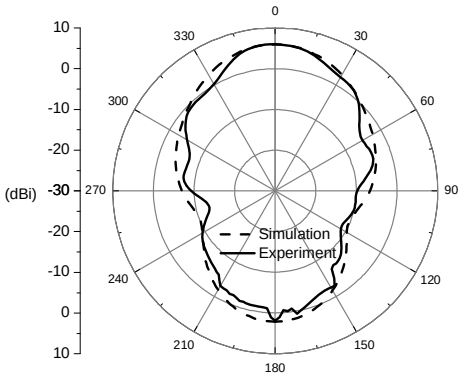

(b)

Fig. 9. Simulated and experimentally measured gain patterns of the array with DGS in Fig. 7; (a) in *E*-plane, (b) in *H*-plane.

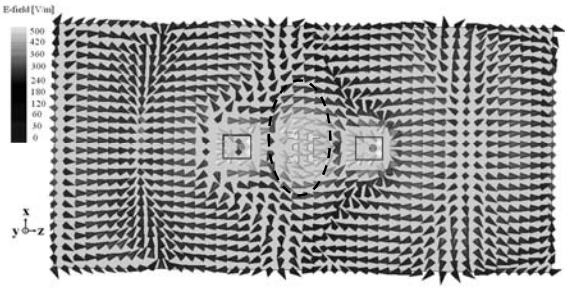

Fig. 10. Simulated *E*-field distributions in front view of the array in Fig. 7.

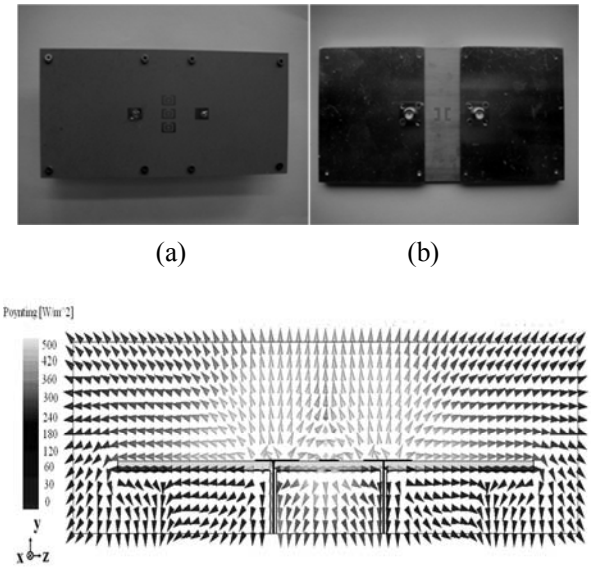

(a) (b)

(c)

Fig. 11. Configuration of a two-element array with composite double U-shaped DGS and E-SRRs; (a) front view, (b) back view, and (c) simulated poynting vector distribution in side view.

Based on the electromagnetic condition in the region of interest (in Fig. 10) well consistent with the condition shown in Fig.1(b), the three-periodic E-SRRs are proposed to be placed at the upper surface of the substrate to block the EM energy leaking into backward space [10]. It is noted that, unlike application in the free space as a semi-infinite periodic structure [23], there are only three elements etched at the substrate upper surface instead. Additionally, the DGS etched at the other side of the substrate exhibits intercoupling with the SRRs. Because of the above main factors, all the metallic part parameters of the E-SRRs given in Section II are enlarged by three quarters in order to obtain the required rejection frequency band. On the other hand, the double U-shaped DGS given in Fig. 1(a) are also adjusted in order to obtain the required rejection frequency band. To simplify the design of the DGS for the proposed array, only the length of the double slots *L* is optimized to *7.4mm* (in Figs. 11(a) and (b)). Figure 11(c) indicates that the energy leaking downwards reduces sharply compared with that in Fig. 7(c), which approves the remarkable performance of E-SRRs electric response in inhibiting EM energy from upside.

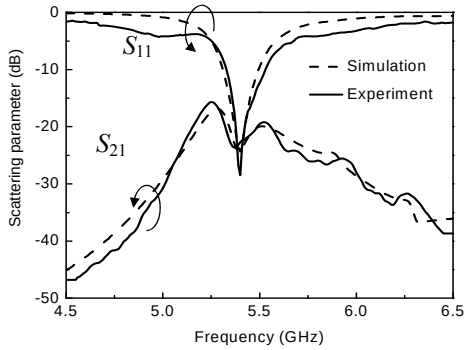

Fig. 12. Simulated and experimentally measured input matching (S_{11}) and mutual coupling (S_{21}) of the two patches in Fig. 11.

In the same way, the measured results together with simulated results are also shown in Figs. 12 and 13. In Fig. 12, the mutual coupling S_{21} maintains the reduction to -24.5dB around the operating frequency

5.4GHz, and shows stabilization in its reduction. And more importantly, the gain pattern in Fig. 13 keeps smooth, the peak gain increases 2.15dB, back lobe gain drops 2.84dB and front-to-back ratio of the gains of 9.93dB, in contrast with the array with only DGS in Section III(B), which shows a close agreement with the simulated poynting vector distribution in Fig. 11(c).

Furthermore, in order to demonstrate the unique capability of the E-SRRs in improving the performance in detail, a metal sheet of the same dimensions is etched halfway between E-coupled elements instead. According to poynting vector distribution in Fig. 14, the energy propagating into backward space is neglected, by virtue of intrinsic isolation property of the metal. Figure 15 also validates the gain of main lobe and back lobe is optimized just like that in Fig. 6. However, the mutual coupling increases to -16.5dB except for a trivial variation in Fig. 16, which also damages the smoothness of the radiation pattern in *E*-plane severely shown in Fig. 15(a). That is to say, the metal above the substrate works as a surface wave "bridge" that leads the pronounced surface wave to pass across the DGS-etched region, even if the DGS possesses the characteristic of predominant suppression in mutual coupling. The above phenomenon indicates the metal sheet cannot take up the E-SRRs as an isolation wall horizontally laid at the substrate upper surface, due to its adverse impact on the mutual coupling reduction.

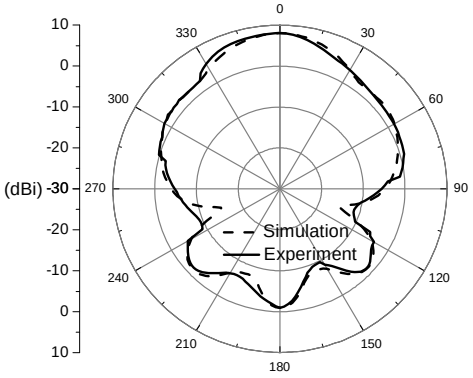

(a)

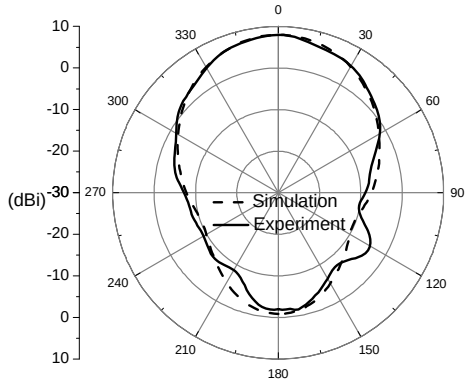

(b)

Fig. 13. Simulated and experimentally measured gain patterns of the array with composite structure in Fig. 11; (a) in *E*-plane, (b) in *H*-plane.

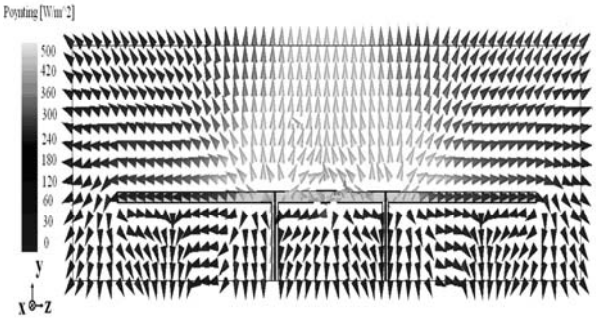

Fig. 14. Simulated poynting vector distribution in side view of two-element array with composite DGS and metal.

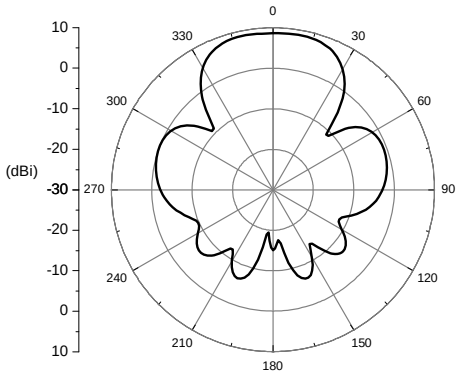

(a)

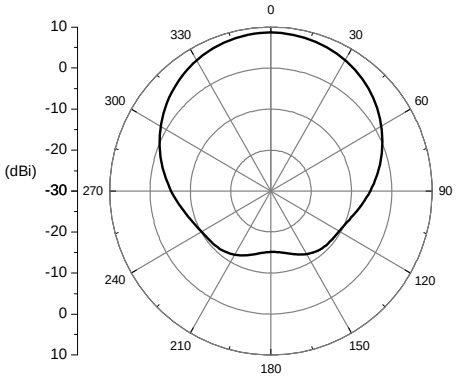

(b)

Fig. 15. Simulated gain patterns of the array with composite double U-shaped DGS and metal in Fig. 14; (a) in *E*-plane, (b) in *H*-plane.

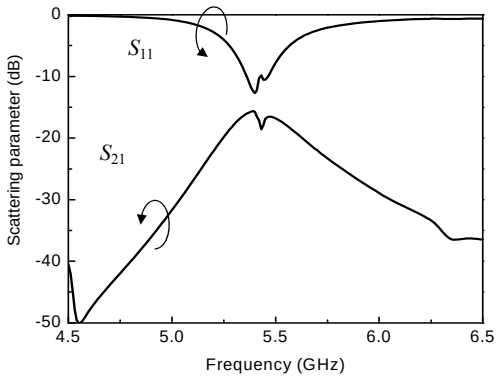

Fig. 16. Simulated input matching (S_{11}) and mutual coupling (S_{21}) of the two patches in Fig.14.

IV. SCAN BLINDNESS ELIMINATION IN MICROSTRIP PHASED ARRAY

The scan characteristic of the infinite microstrip phased array is calculated and discussed in this section. Figure 17 gives the sketch of the infinite phased array cell. In this array, the periods along the *x*- and *z*-axis are the same of 37.1*mm* (near $0.65\lambda_0$), and the composite DGSs and SRRs are arranged for the reduction of mutual coupling in *E*-plane. Based on the waveguide simulator method, the array characteristic can be extracted by analyzing one of the elements in the array [24].

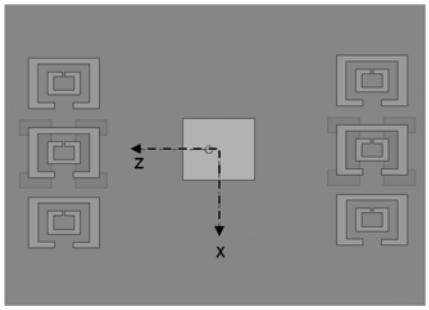

Fig. 17. Topological structure of an infinite phased array cell.

According to literature [24], Fig. 18 gives the calculated scan characteristics of the infinite microstrip phased array without DGSs, with only DGSs and with composite DGSs and SRRs at the resonant frequency of 5.4GHz. These results indicate that, for the traditional phased array, scan blindness occurs at 28° in the *E*-plane and no scan blindness occurs in the *H*-plane. As depicted in literature [4], the scan blindness in the *E*-plane is well eliminated because of the usage of the DGSs. Meanwhile, the DGSs have a weak influence on the array reflection coefficient for the *H*-plane scan patterns. Just like the array with only DGSs, when loaded composite structures, the scan blindness in the *E*-plane array is eliminated as well and the array maintains excellent wide-angle impedance matching. Besides, its influence on scan performance in *H*-plane also counts for little.

The active element patterns for the centre element without DGSs, with only DGSs, and with composite structure are shown in Fig. 19, respectively. All of the patterns are plotted at the operation frequency (5.4 GHz). There are two significant nulls at 28° in the radiation pattern (in *E*-plane) for the array without DGSs in Fig. 20. The nulls are in accord with the blind spots obtained by the waveguide simulator method [5]. In addition, the radiation pattern of the array with the composite structures together with the array with only DGSs, is much smooth and has no apparent ripples in comparison with that of the traditional array. It is noted that, in contrast to the array with only DGSs, the array with composite structures also shows higher peak gain in front radiation and much lower gain in back radiation which results from inhibiting EM energy leaking through DGSs slots by SRRs.

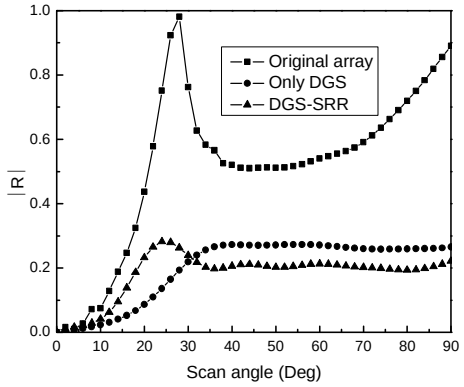

(a)

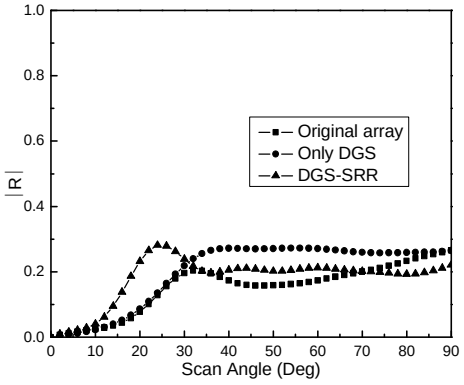

(b)

Fig. 18. Scan characteristics of infinite microstrip array; (a) in *E*-plane, (b) in *H*-plane.

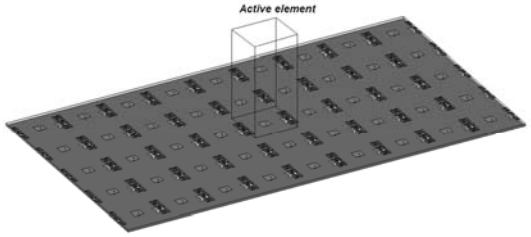

Fig. 19. Centre active element in the 9×5 array.

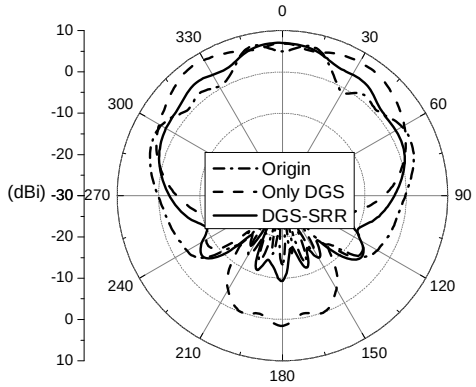

(a)

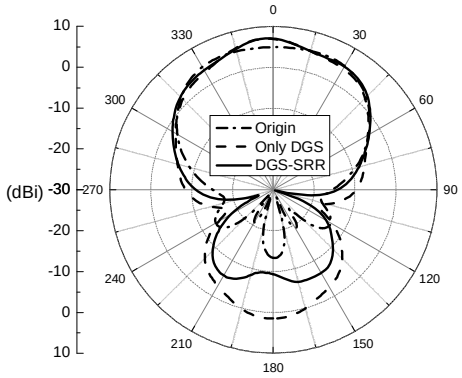

(b)

Fig. 20. Normalized gain patterns of the centre active element against the scan angle in 9×5 array in Fig.19; (a) in *E*-plane, (b) in *H*-plane.

V. CONCLUSION

This paper concentrates on the application of the composite of DGSs and SRRs to eliminate the scan blindness of microstrip phased array by reducing the element mutual coupling. Two-element arrays without DGSs, with only DGSs, and with composite structures are simulated and measured, respectively. The results indicate that a mutual coupling decrease of 11 dB is well achieved at the operation frequency of the array, resulting from the composite structures. Moreover, compared with the array with only DGSs, 2dB gain improvement and 2.4dB side lobe suppression are also attained. Importantly, in our numerical investigation of three kinds of active patterns for center elements in 9×5 element arrays, it

is found that the scan blindness in infinite microstrip phased array can be well eliminated by integrating proposed compact composite structures, in accordance with the simulation results in waveguide simulator. On account of its excellent isolation property and high mechanical strength, it is quite suitable for applying to high-performance array design, and promising for numerous other applications as well in the future.

ACKNOWLEDGMENT

The work was in part supported by the National Nature Science Foundation of China (Grant No. 60872034, 60971029), in part by the Natural Science Foundation of Educational Department of Sichuan Province, China (Grant No. 09ZA053), in part by the New-century Talent program of the Education Department of China (Grant No. NCET070154), and in part by the Aviation Science foundation (Grant No. 20090180007).

REFERENCES

1. Y. Fu and N. Yuan, "Elimination of Scan Blindness in Phased Array of Microstrip Patches using Electromagnetic Bandgap Materials," *IEEE Antennas and Wireless Propag. Lett.*, vol. 3, pp. 63-65, 2004.
2. L. Zhang, J. A. Castaneda, and N. G. Alexopoulos, "Scan Blindness Free Phased Array Design using PBG Materials," *IEEE Trans. Antennas Propag.*, vol. 52, pp. 2000-2007, 2004.
3. B. Wu, H. Chen, J. A. Kong, and T. M. Grzegorczyk, "Surface Wave Suppression in Antenna Systems using Magnetic Metamaterial," *J. Appl. Phys.*, vol. 101, pp. 112913 (1-4), 2007.
4. K. Bull, H. Mosallaei, and K. Sarabandi, "Metamaterial Insulator Enabled Superdirective Array," *IEEE Trans. Antennas Propag.*, vol. 55, pp. 1047-1085, 2007.
5. D. -B. Hou, S. Xiao, B. -Z. Wang, L. Jiang, J. Wang, and W. Hong, "Elimination of Scan Blindness with Compact Defected Ground Structures in Microstrip Phased Array," *IET Microw. Antennas Propag.*, vol. 3, pp. 269-275, 2009.
6. D. Ahn, J.-S. Park, C.-S. Kim, J. Kim, Y. Qian, and T. Itoh, "A Design of the Low-Pass Filter using the Novel Microstrip Defected Ground Structure," IEEE *Trans. Microw. Theory Tech.*, vol. 49, pp. 86-93, 2001.
7. B. D. Braaten, R. P. Scheeler, M. Reich, R. M. Nelson, C. Bauer-Reich, J. Glower, and G. J. Owen, "Compact Metamaterial-Based UHF RFID Antennas: Deformed Omega and Split-Ring Resonator Structures," *Applied Computational Electromagnetic Society (ACES) Journal*, vol. 25, no. 6, pp. 530–542, Jun. 2010.
8. M. R. I. Faruque, M. T. Islam, and N. Misran, "Evaluation of EM Absorption in Human Head with Metamaterial Attachment," *Applied Computational Electromagnetic Society (ACES) Journal*, vol. 25, no. 12, pp. 1097–1107, Dec. 2010.
9. M.-C. Tang, S. Xiao, T. Deng, Y. Bai, J. Guan, and B.-Z. Wang, "Study of Miniaturized Electric Resonance Metamaterial," *Acta Physica Sinica*, vol. 59, no. 7, pp. 4715-4719, Jul. 2010.
10. M.-C. Tang, S. Xiao, J. Guan, Y. Bai, S. Gao, and B. –Z. Wang, "Composite Metamaterial Enabled Excellent Performance of Microstrip Antenna Array," *Chinese Physics B*, vol. 19, pp. 074214(1-5), Jul. 2010.
11. M.-C. Tang, S. Xiao, T. Deng, D. Wang, J. Guan, B. -Z. Wang, and G. Ge "Compact UWB Antenna with Multiple Band-Notches for WiMAX and WLAN," *IEEE Trans. Antennas Propag.*, vol. 59, no. 4, pp. 1372-1376, Apr. 2011
12. N. Katsarakis, T. Koschny, and M. Kafesaki, "Electric Coupling to the Magnetic Resonance of Split Ring Resonators," *Appl. Phys. Lett.*, vol. 84, pp. 2943-2945, 2004.
13. D. R. Smith, W. J. Padilla, D. C. Vier, S. C. Nemat-Nasser, and S. Schultz, "Composite Medium with Simultaneously Negative Permeability and Permittivity," *Phys. Rev. Lett.*, vol. 84, pp. 4184-4187, 2000.
14. J. D. Baena, J. Bonache, F. Martín, R. M. Sillero, F. Falcone, T. Lopetegi, M. A. G. Laso, J. García-García, I. Gil, M. F. Portillo, and M. Sorolla, "Equivalent-Circuit Models for Split-Ring Resonators and Complementary Split-Ring Resonators Coupled to Planar Transmission Lines," *IEEE Trans. Microwave Theory Tech.*, vol. 53, pp. 1451-1461, 2005.
15. D. R. Smith, J. Gollub, J. J. Mock, W. J. Padilla, and D. Schurig, "Calculation and Measurement of Bianisotropy in a Split Ring Resonator

Metamaterial," *J. Appl. Phys.*, vol. 100, pp. 024507(1-9), 2006.
16. P. Gay-Balmaz and O. J. F. Martina, "Electromagnetic Resonances in Individual and Coupled Split-Ring Resonators," *J. Appl. Phys.*, vol. 92, pp. 2929-2936, 2002.
17. T. Koschny, M. Kafesaki, E. N. Economou, and C. M. Soukoulis, "Effective Medium Theory of Left-Handed Materials," *Phys. Rev. Lett.*, vol. 93, pp. 107402(1-4), 2004.
18. R. W. Ziolkowski, "Design, Fabrication, and Testing of Double Negative Metamaterials," *IEEE Trans. Antennas Propag.*, vol. 51, pp.1516-1528, 2003
19. Y. X. Guo, K. M. Luk, and K. W. Leung, "Mutual Coupling Between Millimeter Wave Dielectric Resonator Antennas," *IEEE Trans. Microw. Theory Tech.*, vol. 47, pp. 2164-2166, 1999.
20. F. Yang and Y. Rahmat-Samii, "Microstrip Antennas Integrated with Electromagnetic Band-Gap (EBG) Structures: A Low Mutual Coupling Design for Array Applications," *IEEE Trans. Antennas Propag.*, vol. 51, no. 10, pp. 2936-2945, 2003.
21. A. H. Mohammadian, N. M. Martin, and D. W. Griffin, "A Theoretical and Experimenttal Study of Mutual Coupling in Microstrip Antenna Arrays," *IEEE Trans. Antennas Propag.*, vol. 37, pp.1217-1223, 1989.
22. R. P. Jedlicka, M. T. Poe, and K. R. Carver, "Measured Mutual Coupling Between Microstrip Antennas," *IEEE Trans. Antennas Propag.*, vol. 29, pp. 147-149, 1981.
23. K. Buell, H. Mosallaei, and K. Sarabandi, "A Substrate for Small Patch Antennas Providing Tunable Miniaturization Factors," *IEEE Trans. Microw. Theory Tech.*, vol. 54, pp. 135–146, 2006.
24. D. M. Pozar "Analysis of an Infinite Phased Array of Aperture Coupled Microstrip Patches," *IEEE Trans. Antennas Propag.*, vol. 37, pp. 418–425, 1989.

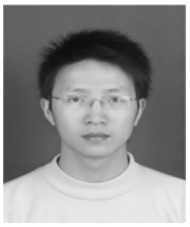

Ming-Chun Tang received the B.S. degree in Physics from the Neijiang Normal University, Neijiang, China, in 2005. He is currently working toward the Ph.D. degree in Radio Physics at University of Electronic Science and Technology of China (UESTC) from 2007.
His research interest includes miniature antenna, RF circuit, metamaterial design, and its application. He has authored or coauthored more than 30 international referred journal and conference papers. He was a recipient of the Best Student Paper Award in 2010 International Symposium on Signals, Systems and Electronics (ISSSE2010). He serves as reviewers for the Journals IEEE Antennas and Wireless Propagation Letters and IEEE Antennas and Propagation Magazine.

Shaoqiu Xiao received the Ph.D. degree in Electromagnetic field and Microwave Engineering from the University of Electronic Science and Technology of China (UESTC), Chengdu, China, in 2003. From January 2004 to June 2004, he joined UESTC as an assistant professor. From July 2004 to March 2006, he worked for the Wireless Communications Laboratory, National Institute of Information and Communications Technology of Japan (NICT), Singapore, as a researcher with the focus on the planar antenna and smart antenna design and optimization. From July 2006 to June 2010, he worked for UESTC as an associate professor and now he is working for UESTC as a professor. His current research interests include planar antenna and array, microwave passive circuits and electromagnetic in ultrawide band communication. He has authored/coauthored more than 100 technical journals, conference papers, books, and book chapters.

Chang-Jin Li received the B.S. degree in Physics from the Sichuan Normal University, Sichuan, China, in 1989, and the master's degree in Pedagogics from the Sichuan Normal University, Sichuan, China, in 2004, respectively. His research interest includes laser characterization, propagation and transformation, resonator technology, and physics.

Chaolei Wei was born in Shandong Province, China, in 1981. He received the B.S. degree in Physics from the Liaocheng University, Liaocheng, Shandong, China in 2006, and the M.D. degree in Nuclear Energy Engineering from the Insititute of Southwest Physics, Chengdu in 2009, respectively, and is currently working toward the Ph.D. degree in Electrical Engineering at University of Electronic Science and Technology of China (UESTC). His research interests include microwave planar filters, microwave and millimeter-wave circuits, and systems design.

Bingzhong Wang received the Ph.D. degree in Electrical Engineering from the University of Electronic Science and Technology of China (UESTC), Chengdu, China, in 1988.

He joined the UESTC in 1984 and is currently a Professor there. He has been a Visiting Scholar at the University of Wisconsin-Milwaukee, a Research Fellow at the City University of Hong Kong, and a Visiting Professor in the Electromagnetic Communication Laboratory, Pennsylvania State University, University Park. His current research interests are in the areas of computational electromagnetics, antenna theory and technique, electromagnetic compatibility analysis, and computer-aided design for passive microwave integrated circuits.

An Efficient Finite-Element Time-Domain Method via Hierarchical Matrix Algorithm for Electromagnetic Simulation

Ting Wan, Rushan Chen, Jianjian She, Dazhi Ding, and Zhenhong Fan

Department of Communication Engineering
Nanjing University of Science and Technology, Nanjing, 210094, China
billwanting@163.com

Abstract ─ An efficient finite-element time-domain (FETD) method based on the hierarchical ($\mathcal{H}$-) matrix algorithm is presented. The FETD method is on the basis of the second-order vector wave equation, obtained by eliminating one of the field variables from Maxwell's equations. The time-dependent formulation employs the Newmark-beta method which is known as an unconditional stable time-integration method. $\mathcal{H}$-matrix algorithm is introduced for the direct solution of a large sparse linear system at each time step, which is a serious handicap in conventional FETD method. $\mathcal{H}$-matrix algorithm provides a data-sparse way to approximate the LU triangular factors of the FETD system matrix. Using the $\mathcal{H}$-matrix arithmetic, the computational complexity and memory requirement of $\mathcal{H}$-LU decomposition can be significantly reduced to almost logarithmic-linear. Once the $\mathcal{H}$-LU factors are obtained, the FETD method can be computed very efficiently at each time step by the $\mathcal{H}$-matrix formatted forward and backward substitution ($\mathcal{H}$-FBS). Numerical examples are provided to illustrate the accuracy and efficiency of the proposed FETD method for the simulation of three-dimension (3D) electromagnetic problems.

Index Terms ─ Direct solution, finite-element time-domain (FETD) method, $\mathcal{H}$-matrix algorithm, reduced complexity.

I. INTRODUCTION

As one of the most efficient numerical methods for the electromagnetic simulation, the finite-element time-domain (FETD) method has been widely applied to the analysis of various problems in the field of computational electromagnetics (CEM) recently. The FETD method holds the advantages of the finite element method (FEM) by combining the geometrical adaptability and material generality for modeling arbitrary shaped and inhomogeneously dielectric-filled objects. Moreover, it can also obtain a wideband response like the finite-difference time-domain (FDTD) method [1]. Therefore, a variety of FETD schemes have been developed during the past decades [2 - 11]. These schemes fall into two categories. The first scheme solves the time-dependent Maxwell's equations directly. The other scheme discretizes the second-order vector wave equation, known as the curl-curl equation, involving one of the field variables from the Maxwell's equations. It is similar to the traditional frequency-domain FEM in spatial discretization and can be made unconditionally stable by using the Newmark-beta method for the temporal discretization [7].

Due to the attractive advantage of the unconditionally stable scheme, the implicit methods are popularly used in the FETD to solve the second-order vector wave equation. However, the capability of an implicit scheme is highly limited since a large sparse linear system needs to be solved at each time step [12,13]. There are two categories of methods for the solution of this sparse linear system, i.e., iterative methods and direct methods. The iterative methods are widely used for large-scale problems due to their O(N) computational complexity, with N being the matrix size [14 , 15]. However, the iterative methods encounter two obstacles. One is the slow convergence rate when the FETD system matrix is

Submitted On: March 3, 2011
Accepted On: August 20, 2011

ill-conditioned, the other is the heavy redundant computational consumption for dealing with problems with multiple right-hand-side (RHS) vectors. These obstacles can be overcome by direct methods. However, the direct methods face the high computational complexity and memory requirement. Nonlinear complexity is familiar in electrodynamic filed, even for existing state-of-the-art sparse matrix solvers. As reported in [16], the optimal complexity of the FEM-based direct solvers was shown to be $O(N^{1.5})$. This means that the direct methods will face a great challenge or even become impractical with the number of unknowns increasing.

In this paper, a direct method based on the hierarchical ($\mathcal{H}$-) matrix algorithm is proposed to yield an efficient FETD scheme with reduced complexity. $\mathcal{H}$-matrices have first been introduced in 1999 [17], and subsequently they were widely used for different applications [18,19]. $\mathcal{H}$-matrices provide an inexpensive but sufficiently accurate approximation to fully populated matrices arising from an integral operator or from the inverse of the finite element discretisation of an elliptic or hyperbolic partial differential operator [20-23]. These matrices are not sparse in the sense that there are only few non-zero entries, but they are *data-sparse* in the sense that these matrices are described by only a few data, that is, certain sub-blocks of these matrices can be described by low-rank approximations which are represented by a product of two low-rank matrices [24,25]. $\mathcal{H}$-matrix arithmetic allows the LU decomposition multiplication to be implemented with nearly optimal complexity $O(k^a N \log^b N)$ with appropriate parameters a,b and a blockwise rank k. The FETD system matrix is sparse and can be represented by an $\mathcal{H}$-matrix without approximation, while its LU-factors can be approximated in data-sparse representations by $\mathcal{H}$-matrices [26]. Based on this, in this paper, an efficient $\mathcal{H}$-LU decomposition algorithm is developed for solving the sparse linear system of the FETD with computational complexity and memory requirement being close to $O(N\log^2 N)$ and $O(N\log N)$ respectively. It should be noted that the $\mathcal{H}$-LU decomposition multiplication only needs to be performed once, and then the $\mathcal{H}$-LU-factors are stored and enter the subsequent FETD computation by the fast $\mathcal{H}$-forward and backward substitutions (FBS) at each time step.

This paper is structured as follows: in Section II, the theory of the FETD method based on the second-order vector wave equation is outlined, along with the Newmark-beta method yielding an unconditional stable FETD scheme. Then, the $\mathcal{H}$-matrix algorithm is presented in detail for the efficient solution of the sparse linear FETD system in Section III. In Section IV, some numerical results are presented to demonstrate the performance of the resulting FETD method. Finally, conclusions are presented in Section V.

II. FETD FORMULATION WITH THE NEWMARK-BETA METHOD

In the FETD method, the whole computational domain is terminated by the anisotropic perfectly matched layer (PML) backed with perfect electronic conductor (PEC) wall. From the Maxwell's equations in the anisotropic material, the curl-curl equation can be derived as follows

$$\nabla \times \frac{1}{\mu}\left([\Lambda]^{-1} \cdot \nabla \times E\right) - \omega^2 \varepsilon [\Lambda] E = 0 , \qquad (1)$$

where $[\Lambda]$ is a diagonal matrix that describes the anisotropic permittivity and permeability of the PML region [27,28].

To get the FETD solution, the frequency-domain formulation is converted to the time-domain version by using the following relationships

$$j\omega \leftrightarrow \frac{\partial}{\partial t} \quad -\omega^2 \leftrightarrow \frac{\partial^2}{\partial t^2} \quad \frac{1}{j\omega} \leftrightarrow \int_0^t \quad \frac{-1}{\omega^2} \leftrightarrow \int_0^t \int_0^t \qquad (2)$$

Then, the computational domain is discretized with tetrahedral elements [29] and the electric field is expressed in terms of the basis functions associated with the edges of each element as

$$E = \sum_{i=1}^{N} W_i e_i , \qquad (3)$$

where N is the total number of the edges in an element, W_i is the vector basis function associated with edge i, and e_i is the unknown coefficient, which is the circulation of the electric field along the edge i. After the Galerkin testing, a weak form can be obtained as follows

$$[A]e + [B]\frac{de}{dt} + [C]\frac{d^2 e}{dt^2} + [D] f + [E] g = 0 , \qquad (4)$$

where

$$
\begin{aligned}
[A]_{ij} &= \iiint_V \frac{1}{\mu_r}\nabla\times W_i\cdot\nabla\times W_j + \\
&\qquad \frac{\varepsilon\mu_0}{\varepsilon_0^2}\left([J]^2+2[K]\right)W_i\cdot W_j dV \\
[B]_{ij} &= \iiint_V \frac{2\varepsilon\mu_0}{\varepsilon_0}[J]W_i\cdot W_j dV \\
[C]_{ij} &= \iiint_V \varepsilon\mu_0 W_i\cdot W_j dV \\
[D]_{ij} &= \iiint_V \frac{2}{\mu_r\varepsilon_0}[I]\nabla\times W_i\cdot\nabla\times W_j dV + \\
&\qquad \iiint_V \frac{2\varepsilon\mu_0}{\varepsilon_0^3}[L]W_i\cdot W_j dV \\
[E]_{ij} &= \iiint_V \frac{1}{\mu_r\varepsilon_0^2}[I]^2\nabla\times W_i\cdot\nabla\times W_j dV + \\
&\qquad \iiint_V \frac{\varepsilon\mu_0}{\varepsilon_0^4}[K]^2 W_i^{(1)}\cdot W_j^{(1)} dV \\
f &= \int_t e dt, \quad g = \iint_t e dt .
\end{aligned} \tag{5}
$$

$[I]$, $[J]$, $[K]$ and $[L]$ are PML-related matrices [30]. Using the Newmark-Beta formulation, (4) can be approximated as

$$
\begin{aligned}
&\left([A]\beta+[B]\frac{1}{2\Delta t}+[C]\frac{1}{\Delta t^2}\right)e^{n+1} = \\
&[A]\left((2\beta-1)e^n-\beta e^{n-1}\right)+[B]\frac{1}{2\Delta t}e^{n-1}+ \\
&[C]\frac{1}{\Delta t^2}\left(2e^n-e^{n-1}\right)+ \\
&[D]\left(\beta f^{n+1}+(1-2\beta)f^n+\beta f^{n-1}\right)+ \\
&[E]\left(\beta g^{n+1}+(1-2\beta)g^n+\beta g^{n-1}\right) \\
&=0
\end{aligned} \tag{6}
$$

It has been proven that unconditional stability is achievable by choosing the interpolation parameter $\beta \geq 1/4$, and it is further shown that this choice of $\beta = 1/4$ minimizes the solution error [5]. Equation (6) can be simplified as

$$[M]e^{n+1} = [b], \tag{7}$$

where $[M]$ and $[b]$ denote the resultant system matrix and right-hand-side (RHS) vector, respectively. At each time step, the updating of the electric field requires solving equation (7). Obviously, $[M]$ keeps invariable while $[b]$ changes with the time steps. For such multi-RHS-vector problem, direct solution is a good choice. Here, an $\mathcal{H}$-LU decomposition algorithm is introduced for the direct solution of (7). Although $[M]$ is sparse, its LU-factors are in general dense. However, $\mathcal{H}$-matrix algorithm provides a data-sparse way to compute and store the LU-factors of $[M]$ at a low cost. After the $\mathcal{H}$-LU decomposition, the update can be fast computed by $\mathcal{H}$-FBS as follows

$$e^{n+1} = U_{\mathcal{H}}^{-1}L_{\mathcal{H}}^{-1}b, \tag{8}$$

where $L_{\mathcal{H}}$ and $U_{\mathcal{H}}$ are the approximate LU-factors with $\mathcal{H}$-matrix representations.

III. $\mathcal{H}$-MATRIX ALGORITHM

$\mathcal{H}$-matrix algorithm can be applied to the FETD method in the following five steps: 1. Construct the cluster tree by a hierarchical partitioning of the set of edge-based basis functions. 2. Construct the block cluster tree from a given cluster tree using appropriate admissibility condition. 3. Generate the $\mathcal{H}$-matrix representation of the FETD system matrix $[M]$. 4. Compute the $\mathcal{H}$-LU decomposition in $\mathcal{H}$-matrix formatted arithmetic to obtain the $\mathcal{H}$-LU-factors. 5. Perform the $\mathcal{H}$-FBS to obtain the solution of (7) at each time step.

A. Construction of the cluster tree

Let I={1,2,……N} be a finite index set, which includes the indices of all edge-based basis functions W_i (i=1,2,…N) in the entire computational domain. Obviously, the FETD system matrix $[M]$ has the $I\times I$ matrix indices. The construction of an $\mathcal{H}$-matrix representation of $[M]$ starts from the construction of a cluster tree. A tree T_I satisfying the following conditions is called a *cluster tree* to I:

1. I is the root of T_I.
2. If $t\in T_I$ is a leaf, then $|t|\leq n_{\min}$, where $|t|$ denotes the number of elements in the set I and $n_{\min}$ is a relatively small number which is predetermined.
3. If $t\in T_I$ is not a leaf, then t has two sons $t_1, t_2 \in T_I$, and $t = t_1 \dot{\cup} t_2$.

The set of sons of $t\in T_I$ is denoted by $S(t)$, and $L(T_I)$ stands for the set of leaves of T_I.

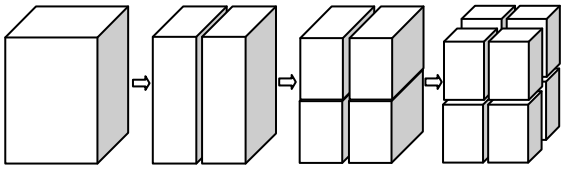

Fig. 1. Subdivision of a finite set using bounding boxes.

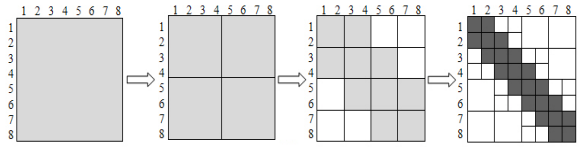

Fig. 3. Construction of a block cluster $T_{I\times I}$. Inadmissible blocks are *dark grey* and admissible blocks are *white*.

A cluster tree T_I is usually obtained by recursive subdivision of I. In this paper, binary trees are generated by subdividing an index set into two subsets recursively. This process continues until the size of the subset is smaller than a threshold parameter $n_{\min}$. $n_{\min}$ is used to control the depth of the cluster tree, i.e., the maximum distance of a vertex to the root of the tree increased by one. In addition, $\Omega_t := \bigcup_{i\in t}\Omega_i$ is defined as the support of a cluster $t \in T_I$ where Ω_i is the support of the basis functions W_i. Ω_i can be chosen to be the bounding box B_i that comprises all the elements sharing W_i. A simple method for building a cluster tree is bisection based on geometry-based subdivisions of the index sets. Fig. 1 shows the process of bisection using bounding boxes and a simple example of a cluster tree is shown in Fig. 2.

B. Construction of the block cluster tree

A block cluster tree $T_{I\times I}$ arises from the grouping of pairs of clusters from the cluster tree T_I, as depicted in Fig. 3. $T_{I\times I}$ can be structured by recursively subdividing each block $v = t\times s$ ($t, s \in T_I$) into four disjoint subblocks $t_1\times s_1$, $t_1\times s_2$, $t_2\times s_1$ and $t_1\times s_2$ ($t_1, t_2 \in S(t)$, $s_1, s_2 \in S(s)$). This subdivision stops when

1. $|t| \le n_{\min}$ or $|s| \le n_{\min}$.
2. Clusters *t* and *s* satisfy admissibility condition.

The admissibility condition is a criterion for us to judge whether a block cluster $v \in T_{I\times I}$ allows for a low-rank approximation. As shown in Fig. 4, a standard admissibility condition is given by

$$\max\{diam(B_t), diam(B_s)\} \le \eta dist(B_t, B_s) \quad (9)$$

where B_t and B_s denote the minimal bounding box for the support of cluster *t* and *s*, *diam* and *dist* denote the Euclidean diameter and distance of cluster *t* and *s* respectively, and $\eta \in \mathbb{R}^+$ controls the trade-off. Blocks $v \in T_{I\times I}$ satisfying (9) are called admissible blocks, as shown in Fig. 3, which can be approximated by low-rank representtation in the following Rk-matrices as follows

$$M|_{m\times n} = AB^T, A \in \mathbb{R}^{m\times k}, B \in \mathbb{R}^{n\times k}, \quad (10)$$

with *A*, *B* in full matrix representation, and *k* is much smaller than *m* and *n*.

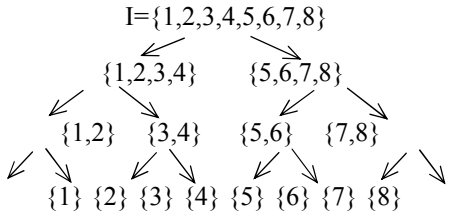

Fig. 2. A simple binary cluster tree T_I.

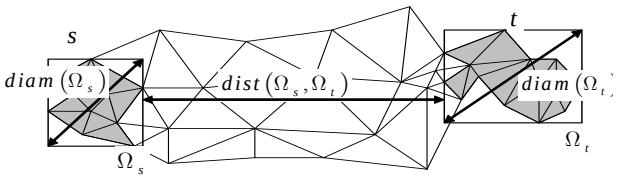

Fig. 4. Model graph of the admissibility condition.

C. Generate the $\mathcal{H}$-matrix representation of the FETD system matrix

Based on the block cluster tree $T_{I\times I}$, the class of $\mathcal{H}$-matrices with blockwise rank *k* and minimum block size $n_{\min}$ of the FETD system matrix $[M]$ can be defined as

$$H(T,k) := \{M \in \mathbb{R}^{I\times I} \mid \forall t\times s \in L(T): \operatorname{rank}(M|_{t\times s}) \le k \text{ or } |t| \le n_{\min} \text{ or } |s| \le n_{\min}\}. \quad (11)$$

An $\mathcal{H}$-matrix induced by the block cluster tree $T_{I\times I}$ is on the basis of two cluster trees, named row cluster tree, and column cluster tree. In the $\mathcal{H}$-matrix structure of $[M]$ generated from the Galerkin method, the row and column cluster tree can be seen as the trees of the sets of original basis functions and testing basis functions respectively. Hence, all entries of $[M]$ can be filled into the

blocks of an $\mathcal{H}$-matrix compatibly. It should be pointed that, in the $\mathcal{H}$-matrix representation of $[M]$, all the nonzero matrix entries of $[M]$ are filled in inadmissible leaves while admissible leaves keep empty. This is because the partial differential operator is local, the nonzero entries of $[M]$ appear only in the case that the associated pair of bounding boxes B_t and B_s have a nonempty intersection. However, if the admissibility condition is satisfied, $dist(B_t, B_s)$ must be larger than zero since η is positive. Therefore, to generate the $\mathcal{H}$-matrix representation of $[M]$, one only needs to fill the inadmissible leaves with the nonzero entries of $[M]$ while keeps the admissible leaves empty. Inadmissible leaves are blocks stored as full matrices exactly so that $[M]$ can be represented by an $\mathcal{H}$-matrix without approximation.

D. $\mathcal{H}$-LU decomposition and $\mathcal{H}$-FBS

The obtained $\mathcal{H}$-matrix representation of the FETD system matrix $[M]$ has a structure of a quad tree based on a binary tree T_I. $[M]$ can be written as $M=\begin{bmatrix} M_{11} & M_{12} \\ M_{21} & M_{22} \end{bmatrix}$. The $\mathcal{H}$-LU decomposition can be computed recursively from this 2×2 block-matrix as follows

$$M=\begin{bmatrix} M_{11} & M_{12} \\ M_{21} & M_{22} \end{bmatrix}=\begin{bmatrix} L_{11} & \\ L_{21} & L_{22} \end{bmatrix}\begin{bmatrix} U_{11} & U_{12} \\ & U_{22} \end{bmatrix} \quad (12)$$

whose process can be expressed in detail as the following pseudo-code.

Procedure $\mathcal{H}$-LU decomposition (M, r, L, U)
if $Son(r\times r)=\phi$ then
  calculate the LU decomposition $M_{r\times r}=L_{r\times r}U_{r\times r}$ exactly
else
  ($Son(r)=\{r_1,r_2\}$, $M=\begin{bmatrix} M_{11} & M_{12} \\ M_{21} & M_{22} \end{bmatrix}$, $L=\begin{bmatrix} L_{11} & \\ L_{21} & L_{22} \end{bmatrix}$, $U=\begin{bmatrix} U_{11} & U_{12} \\ & U_{22} \end{bmatrix}$)
  call $\mathcal{H}$-LU decomposition (M_{11}, r_1, L_{11}, U_{11})
  call Block $\mathcal{H}$-Forward Substitution (L_{12}, M_{12}, r_1, r_2, U_{12})
  call Block $\mathcal{H}$-Backward Substitution (U_{21}, M_{21}, r_2, r_1, L_{21})
  call $\mathcal{H}$-LU decomposition ($M_{22}-L_{21}U_{12}$, r_2, L_{22}, U_{22})
end

In the above procedure, a triangular solver $PX=Q$ or $XP=Q$ is required for a given lower or upper triangular matrix P and a given right-hand-side (RHS) matrix Q. The lower triangular solver can be viewed as a block $\mathcal{H}$-forward substitution recursively implemented as the following pseudo-code and the upper case as well as the block $\mathcal{H}$-backward substitution is similar. When X and Q are vector, the process of solving $PX=Q$ and $XP=Q$ is the $\mathcal{H}$-FBS.

Procedure Block $\mathcal{H}$-Forward Substitution (L, Q, r_i, r_j, X)
if $Son(r_i\times r_j)=\phi$ then
  calculate the $L_{r_i\times r_i}X_{r_i\times r_j}=Q_{r_i\times r_j}$ exactly
else
  ($Son(r)=\{r_1,r_2\}$, $L=\begin{bmatrix} L_{11} & \\ L_{21} & L_{22} \end{bmatrix}$, $Q=\begin{bmatrix} Q_{11} & Q_{12} \\ Q_{21} & Q_{22} \end{bmatrix}$, $X=\begin{bmatrix} X_{11} & X_{12} \\ X_{21} & X_{22} \end{bmatrix}$)
  call Block $\mathcal{H}$-Forward Substitution (L_{11}, Q_{11}, r_1, r_1, X_{11})
  call Block $\mathcal{H}$-Forward Substitution (L_{11}, Q_{12}, r_1, r_2, X_{12})
  call Block $\mathcal{H}$-Forward Substitution (L_{22}, $Q_{21}-L_{21}X_{11}$, r_2, r_1, X_{21})
  call Block $\mathcal{H}$-Forward Substitution (L_{22}, $Q_{22}-L_{21}X_{12}$, r_2, r_2, X_{22})
end

In all the procedures above, the exact addition and multiplication are replaced by the formatted $\mathcal{H}$-matrix counterparts ($\oplus$ and $\otimes$). Truncation operator $\mathcal{T}^{\mathcal{H}}_{k\leftarrow k'}$ based on truncated versions of the QR-decomposition and SVD is used to define $\mathcal{H}$-matrix addition $\mathcal{H}_1\oplus\mathcal{H}_2=\mathcal{T}^{\mathcal{H}}_{k\leftarrow k'}(\mathcal{H}_1+\mathcal{H}_2)$ and $\mathcal{H}$-matrix multiplication $\mathcal{H}_1\otimes\mathcal{H}_2=\mathcal{T}^{\mathcal{H}}_{k\leftarrow k'}(\mathcal{H}_1\times\mathcal{H}_2)$. In this paper, an adaptive truncation scheme with a relative truncation error $\varepsilon_{\mathcal{H}}$ is adopted, i.e., the rank of each admissible block is determined adaptively based on a required level of accuracy. The resulting $\mathcal{H}$-LU-factors $L_{\mathcal{H}}$ and $U_{\mathcal{H}}$ have the

Table 1: Performance of the $\mathcal{H}$-matrix algorithm

$\varepsilon_{\mathcal{H}}$	δ	$\mathcal{H}$-LU Time(s)	Memory(MB)	$\mathcal{H}$-FBS Time(s)
1.0e-1	1.39e-4	0.26	6.32	6.62e-3
1.0e-2	2.07e-5	0.36	8.69	7.88e-3
1.0e-3	1.12e-6	0.58	11.17	9.39e-3
1.0e-4	1.73e-8	0.84	14.64	1.08e-2
1.0e-5	2.29e-11	1.25	17.11	1.30e-2

same tree-structure as the $\mathcal{H}$-matrix representation of $[M]$, whereas the Rk-matrices may be not empty but filled with non-zero items during the recursion. The computational complexity of the $\mathcal{H}$-LU has been proven to be O(k^2Nlog^{2}N) [25] with blockwise rank k. Once $L_{\mathcal{H}}$ and $U_{\mathcal{H}}$ have been obtained, we only need to perform the $\mathcal{H}$-FBS as (8) at each time step of the FETD, whose computational complexity is O(kNlogN).

IV. NUMERICAL RESULTS

In this section, some numerical examples of microwave circuits are simulated to demonstrate the performance of the proposed FETD method based on the $\mathcal{H}$-matrix algorithm. All computations are performed on an Intel Xeon E5405 workstation with 2.0GHz CPU and 16GB RAM in double precision.

A. A waveguide example

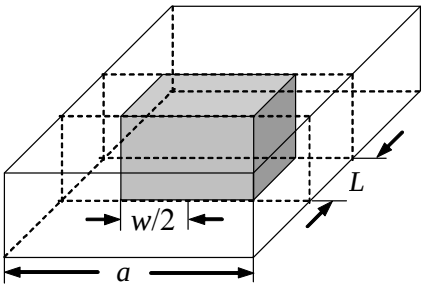

Fig. 5. Configuration of the full-height dielectric-filled rectangular waveguide.

The first example considers a waveguide filled with a full-height dielectric [31], as shown in Fig. 5. The rectangular waveguide has a width of a=22.86mm, and a height of b=10.16mm and the inserted dielectric material slab has a dimension of w=12mm and L=6mm and a relative permittivity of $\varepsilon_r = 8.2$. In order to obtain an input reflection coefficient, two blocks of PML are placed at the input port and the out port to simulate the input and output matched loads. A modulated Gaussian pulse is applied, with mid-frequency $f_0 = 10.0$ GHz and bandwidth $= 4.0$GHz. The $\mathcal{H}$-matrix algorithm associated parameter η in the admissibility condition (9) is set to be $\eta = 1.0$ and the minimal block size is chosen as $n_{\min} = 32$. First, the unknown number is fixed at N=4,290 to test the performance of the $\mathcal{H}$-LU decomposition for solving the FETD system. The relative error of the $\mathcal{H}$-LU factors $L_{\mathcal{H}}$ and $U_{\mathcal{H}}$ is defined as $\delta = \left\| I - U_{\mathcal{H}}^{-1} L_{\mathcal{H}}^{-1} M \right\| / \|I\|$, where I is identity matrix and $\|\cdot\|$ denotes 2-Norm. For different choices of the relative truncation error $\varepsilon_{\mathcal{H}}$, the relative error of $L_{\mathcal{H}}$ and $U_{\mathcal{H}}$, the time used for the $\mathcal{H}$-LU decomposition and the $\mathcal{H}$-FBS and the memory needed for the $\mathcal{H}$-LU decomposition are given in Table 1. Obviously, the relative error δ exponentially decreases with the $\varepsilon_{\mathcal{H}}$ decreasing, while the time and memory required for the $\mathcal{H}$-LU decomposition and the $\mathcal{H}$-FBS increase gradually. Fig. 6 shows the S parameter computed by the proposed $\mathcal{H}$-LU decomposition-based FETD method compared with that simulated by HFSS software in the case of $\varepsilon_{\mathcal{H}} = 1.e-3$. Then, the relative truncation error is fixed $\varepsilon_{\mathcal{H}} = 1.e-4$ and the unknown number increases from 19,317 to 609,364 by increasing the electric size of the waveguide to test the large-scale modeling capability. As shown in Figs. 7 and 8, the time complexity and the memory requirement can be observed to be very close to O(Nlog^{2}N) and O(NlogN), respectively.

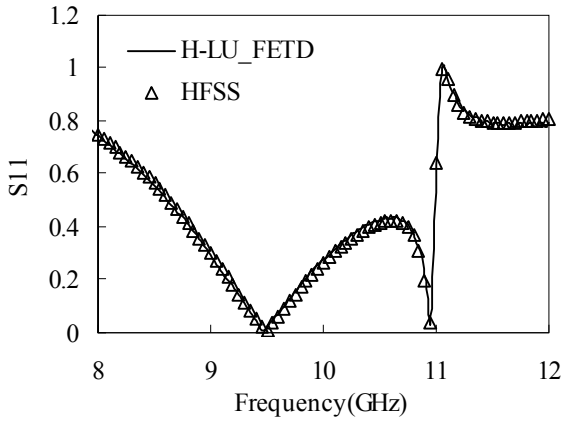

Fig. 6. S parameter of the waveguide filled with a full-height dielectric.

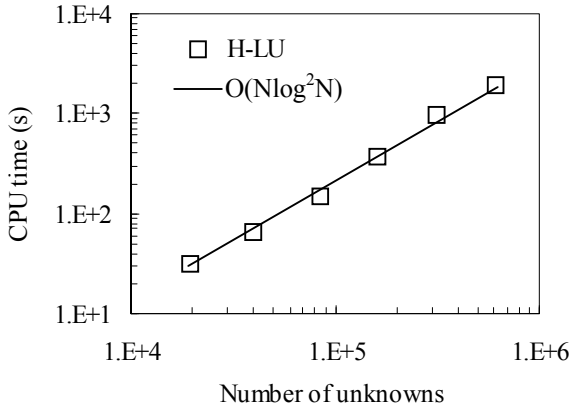

Fig. 7. Time required for the $\mathcal{H}$-LU decomposition.

B. A microstrip lowpass filter example

The second example deals with a microstrip lowpass filter. The detailed geometry of the metallization is shown in Fig. 9. The dielectric substrate has a thickness of $d = 0.76$mm and a relative permittivity of $\varepsilon_r = 2.43$.

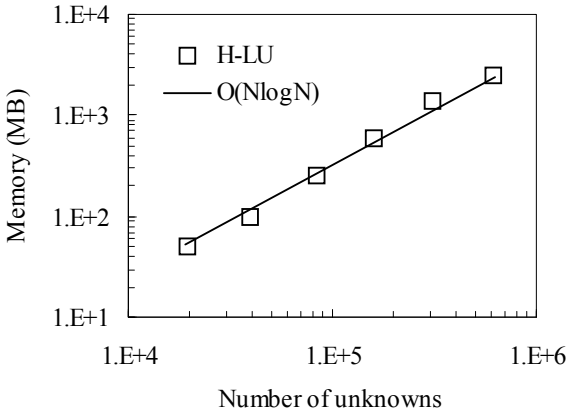

Fig. 8. Memory required for the $\mathcal{H}$-LU factors.

A modulated Gaussian pulse with mid-frequency $f_0 = 9.0$GHz and bandwidth $= 16.0$GHz is applied. The $\mathcal{H}$-matrix algorithm associated parameters are set to be $\eta = 1.0$, $n_{\min} = 64$. The relative truncation error is set to be $\varepsilon_{\mathcal{H}} = 1.e-4$. To test the performance of the $\mathcal{H}$-LU decomposition algorithm, the number of unknowns N increases from 42,927 to 412,863 by increasing the electric size of this microstrip. As shown in Figs. 10 and 11, the CPU time and memory requirements for the $\mathcal{H}$-LU are presented to be close to O(Nlog^{2}N) and O(NlogN), respectively. Moreover, the time requirements for the $\mathcal{H}$-FBS are also shown in Fig. 10, which are close to O(NlogN). As can be seen from Fig. 10, even in the case N =231,263, the computational time of the $\mathcal{H}$-FBS is only 3.15s, which means that once $\mathcal{H}$-LU factors are obtained, the computation of the FETD method at each time step can be finished with no more than 3.15s CPU time.

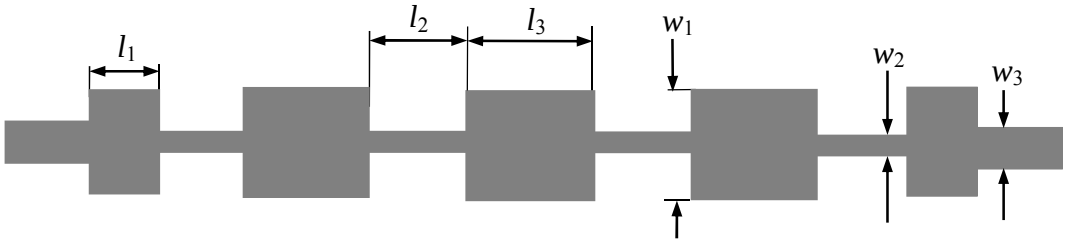

l_1=3.5 mm, l_2=5.6 mm, l_3=3.0 mm, w_1=5.6 mm, w_2=0.62 mm, w_3=2.2 mm

Fig. 9. Geometry and dimensions of the microstrip lowpass filter.

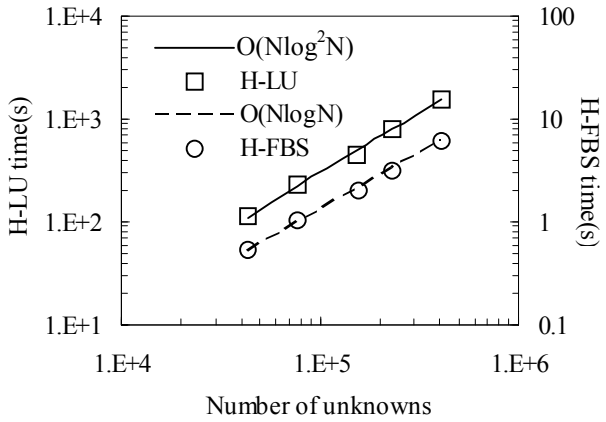

Fig. 10. Time required for the $\mathcal{H}$-LU decomposition and the $\mathcal{H}$-FBS.

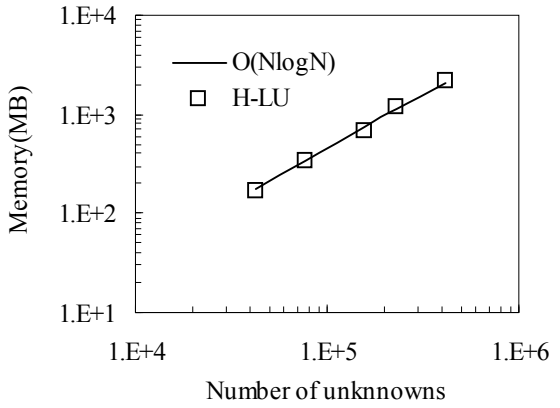

Fig. 11. Memory required for the $\mathcal{H}$-LU factors.

Meanwhile, good accuracy is achieved and the relative error is relatively stable as shown in Fig.

12, which is accurate enough for a correct solution. Figure 13 presents the S parameters computed by the $\mathcal{H}$-LU decomposition-based

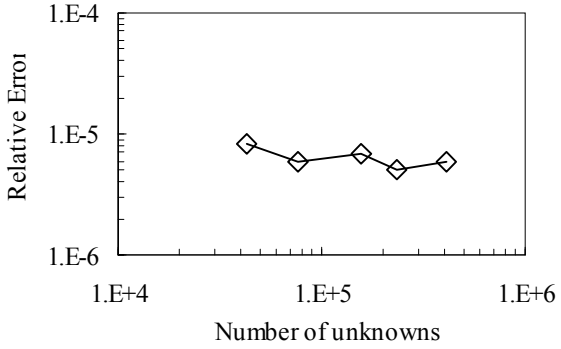

Fig. 12. Relative error of the $\mathcal{H}$-LU decomposition.

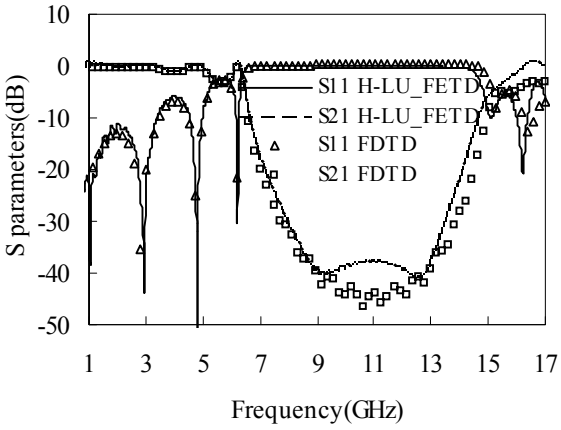

Fig. 13. S parameters of the microstrip lowpass filter.

FETD method in the case N =231,263 compared with that computed by the finite-difference time-domain (FDTD) method.

C. A fractal-shaped UWB bandpass filter example

The last example deals with a fractal-shaped ultra-wideband (UWB) bandpass filter (BPF). Figure 14 shows the topology and detailed sizes of the UWB-BPF structure. The UWB-BPF has been

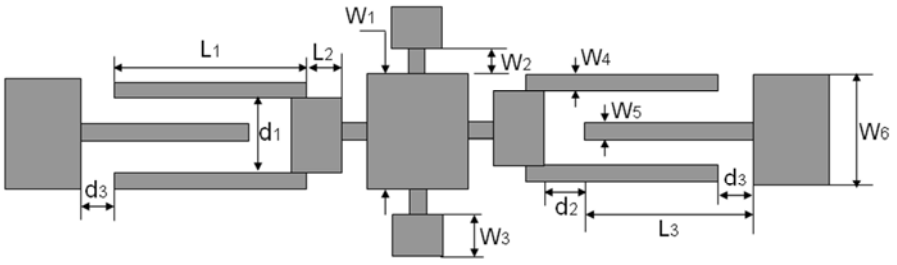

l_1=4.7 mm, l_2=0.2 mm, l_3=4.6 mm, d_1=0.3 mm, d_2=d_3=0.2 mm, w_1=1.3 mm, w_2=w_4= w_5=0.1 mm, w_3=0.3 mm, w_6=0.76 mm

Fig. 14. Geometry and dimensions of the fractal-shaped UWB bandpass filter.

fabricated on a substrate with relative permittivity $\varepsilon_r = 2.43$ and thickness $d = 0.76$mm . A modulated Gaussian pulse with mid-frequency $f_0 =$ 7.0GHz and bandwidth=12.0GHz is applied. The total number of unknowns is 310,035. The $\mathcal{H}$-matrix algorithm associated parameters are set to be $\eta = 1.0$, $n_{\min} = 64$. Table 2 shows the relative error of $L_{\mathcal{H}}$ and $U_{\mathcal{H}}$, the time used for the $\mathcal{H}$-LU decomposition and the $\mathcal{H}$-FBS and the memory needed for the $\mathcal{H}$-LU decomposition with the relative truncation error $\varepsilon_{\mathcal{H}}$ decreasing. Figure 15 presents the S parameters computed by the $\mathcal{H}$-LU decomposition-based FETD method in the case compared with that simulated by HFSS software. As can be seen from Fig. 15, reasonable agreement can be observed in the whole frequency band. The -10dB return loss bandwidth is from 3.2 GHz to 10.8GHz with mid-frequency 7.0GHz. What's more, in the bandwidth of interest, the designed UWB filter achieves an almost flat frequency response of insertion loss close to 0 dB.

V. CONCLUSION

In this paper, an efficient FETD method based on the second-order vector wave equation is generated by using the $\mathcal{H}$-matrix algorithm to directly solve the large sparse linear FETD system. The Newmark-beta scheme is implemented leading to an unconditionally stable FETD method. The $\mathcal{H}$-matrix algorithm provides a data-sparse way to compute and store the LU-factors of the FETD system matrix. This $\mathcal{H}$-LU decomposition can be implemented with reduced complexity, which highly improves the capability of the FETD method for large-scale modeling. Via the $\mathcal{H}$-FBS, the FETD system can be computed rapidly at each time step. Numerical results validate that the $\mathcal{H}$-LU-based direct solver significantly reduces the computational complexity and memory require-ment to be close to $O(N\log^2 N)$ and $O(N\log N)$, respectively, and demonstrate the validity and efficiency of the proposed FETD method in the applications of electromagnetic simulation.

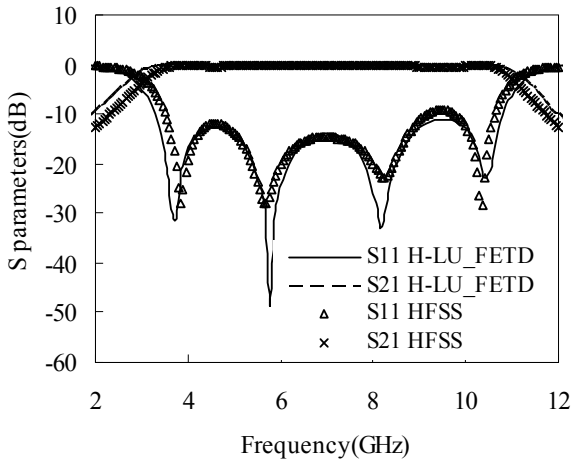

Fig. 15. S parameters of the fractal-shaped UWB bandpass filter.

ACKNOWLEDGMENT

We would like to thank the support of the Major State Basic Research Development Program of China (973 Program: 2009CB320201), Natural Science Foundation of 60871013, Jiangsu Natural Science Foundation of BK2009387 and NUST 2010ZYTS027.

REFERENCES

[1] F. L. Teixeira, "A Summary Review on 25 Years of Progress and Future Challenges in FDTD and FETD Techniques," *Applied Computational Electromagnetic Society (ACES) Journal*, vol. 25, no. 1, pp. 1-14, Jan. 2010.

[2] J. F. Lee, R. Lee, and A. C. Cangellaris, "Time-Domain Finite Element Methods," *IEEE Transactions on Antennas and Propagation.*, vol. 45, pp. 430-442, 1997.

Table 2: Performance of the $\mathcal{H}$-matrix algorithm

$\varepsilon_{\mathcal{H}}$	δ	$\mathcal{H}$-LU Time(s)	Memory(MB)	$\mathcal{H}$-FBS Time(s)
1.0e-2	4.79e-3	626.2	783.5	3.6
1.0e-3	1.82e-4	854.8	1246.4	4.2
1.0e-4	2.77e-5	1387.5	1833.0	4.9

[3] M. F. Wongm, O. Picon, and V. F. Hanna, "A Finite-Element Method Based on Whitney Forms to Solve Maxwell Equations in the Time-Domain," *IEEE Trans. Magn.*, vol. 31, pp. 1618-1621, 1995.

[4] B. Donderici and F. L. Teixeira, "Mixed Finite-Element Time-Domain Method for Transient Maxwell Equations in Doubly Dispersive Media," *IEEE Trans. Microwave Theory Tech.*, vol. 56, no. 1, pp. 113-120, 2008.

[5] H. –P. Tsai, Y. Wang, and T. Itoh, "An Unconditionally Stable Extended (USE) Finite-Element Time- Domain Solution of Active Nonlinear Microwave Circuits Using Perfectly Matched Layers," *IEEE Tran. Microwave Theory Tech.*, vol. 50, no. 10, pp. 2226-2232, Oct. 2002.

[6] N. Marais and Davidson, "Numerical Evaluation of High-Order Finite Element Time Domain Formulations in Electromagnetics," *IEEE Trans. Antennas Propagat.*, vol. 56, vol. 12, pp. 3743-3751, 2008.

[7] S. D. Gedney and U. Navsariwala, "An Unconditionally Stable Finite Element Time-Domain Solution of the Vector Wave Equation," *IEEE Tran. M*icrowave *and Guided Wave Letters*, vol. 5, no. 10, pp. 332-334, Oct. 1995.

[8] M. Feliziani and F. Maradei, "Hybrid Finite Element Solution of Time Dependent Maxwell's Curl Equations," *IEEE Trans. Magn.*, vol. 31, no. 3, pp. 1330-1335, May 1995.

[9] R. N. Rieben, G. H. Rodrigue, and D. A. White, "A High-Order Mixed Vector Finite Element Method for Solving the Time Dependent Maxwell Equations on Unstructured Grids," *J. Comp. Phys.*, vol. 204, pp. 490-519, 2005.

[10] S. D. Gedney, C. Luo, J. A. Roden, R. D. Crawford, B. Guernsey, J. A. Miller, T. Kramer, and E. W. Lucas, "The Discontinuous Galerkin Finite-Element Time-Domain Method Solution of Maxwell's Equation," *Applied Computational Electromagnetic Society (ACES) Journal*, vol. 24, no. 2, pp. 129-142, April 2009.

[11] N. V. Kantartzis and T. D. Tsiboukis, Modern EMC Analysis Techniques - Volume I: Time-Domain Computational Schemes. San Rafael, CA, USA: Morgan & Claypool Publishers, 2008.

[12] T. V. Yioultsis, N. V. Kantartzis, C. S. Antonopoulos, and T. D. Tsiboukis, "A Fully Explicit Whitney-Element Time-Domain Scheme with Higher Order Vector Finite Elements for Three-Dimensional High-Frequency Problems," *IEEE Trans. Magn.*, vol. 34, no. 5, pp. 3288-3291, Sept. 1998.

[13] B. He and F. L. Teixeira, "A Sparse and Explicit FETD via Approximate Inverse Hodge (Mass) Matrix," *IEEE Microw. Wireless Comp. Lett.*, vol. 16, no. 6, pp. 348-350, 2006.

[14] Y. Saad, *Iterative Methods for Sparse Linear Systems*. New York: PWS Publishing, 1996.

[15] Z. Jia and B. Zhu, "A Power Sparse Approximate Inverse Preconditioning Procedure for Large Sparse Linear Systems," *Numer. Linear Algebra Appl.*, vol. 16, pp. 259-299, 2009.

[16] A. George, "Nested Dissection of a Regular Finite Element Mesh," *SIAM J. on Numerical Analysis*, 10(2):345-363, April 1973.

[17] W. Hackbusch, "A Sparse Matrix Arithmetic Based on $\mathcal{H}$-Matrices. I. Introduction to $\mathcal{H}$-Matrices," *Computing*, 62 (2):89-108, 1999.

[18] W. Hackbusch and B. Khoromskij, "A Sparse $\mathcal{H}$-Matrix Arithmetic. Part II: Application to Multi-Dimensional Problems," *Computing*, 6, pp. 21-47, 2000.

[19] S. Börm and L. Grasedyck, "Low-Rank Approximation of Integral Operators by Interpolation," *Computing*, vol. 72, pp. 325-332, 2004.

[20] M. Bebendorf and S. Rjasanow, "Adaptive Low-Rank Approximation of Collocation Matrices," *Computing*, 70, pp. 1-24, 2003.

[21] M. Bebendorf and W. Hackbusch, "Existence of $\mathcal{H}$-Matrix Approximants to the Inverse FE Matrix of Elliptic Operators with L^∞-Coefficients," *Numer. Math.*, 95 (2003), pp.1-28.

[22] H. Liu and D. Jiao, "A Direct Finite-Element-Based Solver of Significantly Reduced Complexity for Solving Large-Scale Electro-

magnetic Problems," IMS 2009, pp. 177-180, 2009.

[23] H. Liu and D. Jiao, "Existence of $\mathcal{H}$-Matrix Representations of the Inverse Finite-Element Matrix of Electrodynamic Problems and $\mathcal{H}$-Based Fast Direct Finite-Element Solvers," *IEEE Trans. on Microwave Theory and Techniques*, vol. 58, no. 12, pp. 3697-3709, Dec. 2010.

[24] S. Borm, L. Grasedyck, and W. Hackbusch, "Induction to Hierarchical Matrices with Applications," *Engineering Analysis with Boundary Elements*, no. 27, pp. 405-422, 2003.

[25] L. Grasedyck and W. Hackbusch, "Construction and Arithmetics of $\mathcal{H}$-Matrices," *Computing*, vol. 70, no. 4, pp. 295-344, August 2003.

[26] M. Bebendorf, "Why Finite Element Discretizations can be Factored by Triangular Hierarchical Matrices," *SIAM J. Matrix Anal*. Appl., 45(4):1472-1494, 2007.

[27] J. P. Berenger, "A Perfectly Matched Layer for the Absorption of Electromagnetic Waves," *J. Compru. Phys*., vol. 114, pp. 185-200, Oct. 1994.

[28] S. D. Gedney, "An Anisotropic Perfectly Matched Layer-Absorbing Medium for the Truncation of FDTD Lattices," *IEEE Transactions on Antennas and Propagation*, vol. 44, no. 11, pp. 1630-1639, 1996.

[29] A. Bossavit, "Whitney Forms: A Class of Finite Elements for Three Dimensional Computations in Electromagnetism," *IEE Proc. Pt. A*, vol. 135, no. 8, pp. 493-500, Nov. 1988.

[30] Lei Du, R. S. Chen, and Z. B. Ye, "Perfectly Matched Layers Backed with the First Order Impedance Boundary Condition for the Time-Domain Finite-Element Solution of Waveguide Problems," *Microwave and Optical Technology Letters*, vol. 50, no. 3, pp. 838-843, March 2008.

[31] R. S. Chen, E. K. N. Yung, C. H. Chan, D. X. Wang, and D. G. Fang, "Application of the SSOR Preconditioned CG Algorithm to the Vector FEM for 3-D Full-Wave Analysis of Electromagnetic-Field Boundary-Value Problems," *IEEE Trans. Microwave Theory Tech*., vol. 50, no. 4, pp. 1165-1172, 2002.

Ting Wan was born in Huanggang, Hubei, China. He received the B.S. and M.S. degrees in Electrical Engineering from Nanjing University of Science and Technology (NJUST), Nanjing, China, in 2003 and 2006, respectively. He is currently working toward the Ph.D. degree in the Department of Communication Engineering at NJUST. His research interests include computational electromagnetics, antennas and microwave integrated circuits.

Rushan Chen was born in Jiangsu, China. He received his B.S. and M.S. degrees from the Dept. of Radio Engineering, Southeast University, in 1987 and in 1990, respectively, and his Ph.D. from the Dept. of Electronic Engineering, City University of Hong Kong in 2001. Since September 1996, he has been a Visiting Scholar with the Department of Electronic Engineering, City University of Hong Kong, first as Research Associate, then as a Senior Research Associate in July 1997, a Research Fellow in April 1998, and a Senior Research Fellow in 1999. From June to September 1999, he was also a Visiting Scholar at Montreal University, Canada. In September 1999, he was promoted to Full Professor and Associate Director of the Microwave & Communication Research Center in NJUST and in 2007, he was appointed Head of the Dept of Communication Engineering, Nanjing University of Science & Technology. His research interests mainly include microwave/millimeter-wave systems, measurements, antenna, RF-integrated circuits, and computational electro-magnetics. He is a Senior Member of the Chinese Institute of Electronics (CIE). He received the 1992 third-class science and technology advance prize given by the National Military Industry Department of China, the 1993 third class science and technology advance prize given by the National Education Committee of China, the 1996 second-class science and technology advance prize given by the

National Education Committee of China, and the 1999 first-class science and technology advance prize given by JiangSu Province as well as the 2001 second-class science and technology advance prize. At NUST, he was awarded the Excellent Honor Prize for academic achievement in 1994, 1996, 1997, 1999, 2000, 2001, 2002, and 2003. He has authored or co-authored more than 200 papers, including over 140 papers in international journals. He is the recipient of the Foundation for China Distinguished Young Investigators presented by the National Science Foundation (NSF) of China in 2003. In 2008, he became a Chang-Jiang Professor under the Cheung Kong Scholar Program awarded by the Ministry of Education, China.

Jianjian She was born in Jiangsu, China. He is currently working toward the M.S. degree in the Department of communi-cation engineering at Nanjing University of Science and Technology, Nanjing, China. His research interests include computational electromagnetics, antennas and microwave integrated circuits.

Dazhi Ding was born in Jiangsu, China. He received the B.S. and Ph.D. degrees in Electro-magnetic Field and Microwave Technique from Nanjing Univer-sity of Science and Technology (NJUST), Nanjing, China, in 2002 and 2007, respectively. During 2005, he was with the Center of wireless Communication in the City University of Hong Kong, Kowloon, as a Research Assistant. He is currently a Lecturer with the Electronic Engi-neering of NJUST. He is the author or coauthor of over 20 technical papers. His current research interests include computational electromagnetics, electromagnetic scattering and radiation.

Zhenhong Fan was born in Jiangsu, China, in 1978. He received the M.Sc and Ph.D degrees in Electromagnetic Field and Microwave Technique from Nanjing University of Science and Technology (NJUST), Nan-jing, China, in 2003 and 2007, respectively. During 2006, he was with the Center of wireless Communication in the City University of Hong Kong, Kowloon, as a Research Assistant. He is currently a Lecturer with the Electronic Engineering of NJUST. He is the author or coauthor of over 20 technical papers. His current research interests include computational electromagnetics, electromagnetic scattering, and radiation.

Mutual Coupling Compensation in Non-Uniform Antenna Arrays using Inter-Element Spacing Restrictions

F. Tokan and F. Gunes

Department of Electronics and Communication Engineering
Faculty of Electrics and Electronics, Yıldız Technical University, Yıldız 34349, Istanbul, Turkey
ftokan@yildiz.edu.tr, gunes@yildiz.edu.tr

Abstract ─ In the antenna array synthesis problems, most of the works in literature utilize isotropic elements. Thus, the mutual coupling effects between the array elements are neglected. It is obvious that an array antenna synthesized by neglecting the coupling effects cannot be used in the real world applications due to the possible incompatibilities between the desired and realized radiation patterns. In this work, two array antenna synthesis papers from literature are investigated in terms of mutual coupling effects so the necessary constraints are determined for the array geometry in order to compensate the coupling effects. Here, the same objectives of these two papers are achieved using the generalized pattern search (GPS) algorithm by considering the determined constraints for the inter-element spacings between the array elements. The resulted radiation patterns are validated with the computer simulation technology (CST) software with the aim of detecting possible incompatibilities due to the mutual coupling effects between the array elements. The simulation results verify that by using the constraints determined in this work, the radiation patterns obtained by pattern multiplication can provide the desired radiation demands also in the practical applications.

Index Terms ─ GPS algorithm, mutual coupling effects, non-uniform array, null control, sidelobe suppression.

I. INTRODUCTION

Synthesis of linear antenna arrays has been extensively studied in the last 50 years [1-14]. Generally, the objectives in an array design are achieving the minimum sidelobe level (SLL), maximization of the main beam in the desired direction and obtaining narrow or broad nulls in the directions of interfering signals. In most of the works realized in literature, the antennas of the array are accepted as isotropic. In these works, the possible mutual coupling effects between the array elements are neglected; thus, it is obvious that an array synthesized by neglecting the mutual coupling effects between the array elements may not be convenient for real world applications. Especially, in the works that the inter-element spacings between the elements are employed as optimization variables [4-8], the desired pattern and the pattern obtained in practical realization will not be in a good agreement. Besides, compensation of mutual coupling effects is also investigated in literature [11-12].

In this work, the full wave electromagnetic simulations (CST) of two works from literature [5-6] that have utilized isotropic elements and thus neglected mutual coupling effects between the array elements are performed to observe the differences between the desired and resulted patterns. Then, the reasons of the incongruity between the desired and resulted patterns are determined. Thus, the restrictions for the inter-elements spacings between the array elements are established to minimize the corruptions in the desired patterns occurred due to the mutual coupling effects.

Subsequently, in this work by using these restrictions, the same objectives of the examples in [5-6] are achieved using the GPS algorithm. The obtained array geometries can be used to obtain the desired radiation patterns also when they are used in the practical applications. The proposed

Submitted On: April 5, 2011
Accepted On: July 28, 2011

method can be efficiently employed in various antenna applications. Providing a simple approach by utilizing the determined inter-element spacing restrictions between the array elements, the synthesized radiation pattern will also be convenient for practical applications, thus there will be no need to perform electromagnetic simulation software to confirm the designed array geometry.

In this work, the GPS algorithm is used to achieve the same objectives that are used in [5-6]. GPS methods are introduced as an optimization tool into the antenna engineering for the array antenna synthesis. GPS are nonrandom methods for direct searching minima of a function which may even be discontinuous, non-differentiable, stochastic or highly nonlinear [15-20]. Moreover, the results of the GPS algorithm are validated by comparing with results obtained using the genetic algorithm (GA) and a full wave electromagnetic simulator (CST) which allows the prediction of the performance of antennas to very high accuracy without the need for costly trials and error constructions and measurements.

II. PROBLEM FORMULATION

In the selected papers [5-6], the linear array antenna geometries with 2*N* half-wave dipole antennas distributed symmetrically with respect to the origin along the *y*-axis is given in Fig. 1.

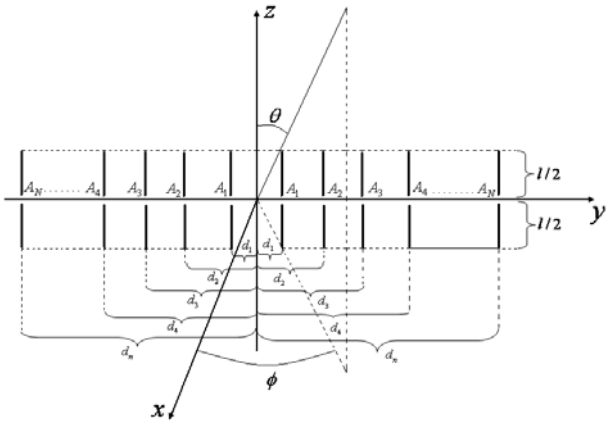

Fig. 1. The linear array antenna geometry with an even number of elements.

This linear array antenna has non-uniform inter-element spacings and also non-uniform excitations for array elements, thus the array factor in the azimuth plane can be expressed as follows [21]:

$$AF = 2\sum_{n=1}^{N} A_n \cos\left[\frac{2\pi d_n}{\lambda}\sin\phi + \beta_n\right], \qquad (1)$$

where 2*N* is total number of the antenna elements, λ is the wavelength in free space; A_n, β_n are the excitation amplitude and phase of the *n*th element, respectively and d_n is the distance from the origin to the *n*th element. In the papers we have used [5-6], β_n is fixed zero, thus the broadside arrays are worked out:

$$AF = 2\sum_{n=1}^{N} A_n \cos\left[\frac{2\pi d_n}{\lambda}\sin\phi\right]. \qquad (2)$$

III. GPS ALGORITHM

GPS methods are a class of direct search methods, originally introduced and analyzed by Torczon [15] for unconstrained minimization problems, and then extended by Lewis and Torczon to problems with bound [16] and general linear constraints [17]. GPS methods have been also adapted to solve nonlinearly constrained problems in an augmented Lagrangian framework [18]. A summary of the work on GPS methods can be found in [19]. Recently, a GPS method [20] is proposed to solve a class of non-smooth minimization problems, where the set of non-differentiability is included in the union of known hyper planes and, therefore, is highly structured. Both unconstrained and linearly constrained problems are considered.

GPS are the direct methods for searching minima of a function which may be even discontinuous, non-differentiable, stochastic, or highly nonlinear. Thus, they can be exploited efficiently in solving optimization problems without requiring any information about the gradient of the fitness function. As opposed to more traditional optimization methods that use information about the gradient or higher derivatives to search for an optimal point, a GPS algorithm searches a set of points around the current point, looking for one where the value of the fitness function is lower than the value at the current point.

It should be mentioned here that this paper is not intended to be an extensive review of GPS, and therefore only the main steps of the GPS algorithm we employed are explained here. The

reader is referred to [4, 15–20] and the references mentioned therein for a detailed discussion of the basic concepts of the GPS algorithm and how it works.

The GPS algorithm is applied to synthesize the same radiation pattern requirements of the selected papers. The objectives of these works are obtaining the minimum SLL and generating narrow or broad nulls in the directions of interfering signals. Thus, we have gathered these multiple objectives in a single fitness function as the logarithmic sums of the array factor, $|AF(\phi)|$ given by (3) and (3.1) as follows:

$$Fitness = 20\log\left\{\sum \max\left\{AF(\phi)\Big|_{\phi_l}^{\phi_u}\right\}\right\} + 20\log\left\{\sum_k |AF(\phi_k)|\right\}, \quad (3)$$

subject to;

$$d_{n+1} - d_n \geq 0.5\lambda, \quad n = 1,.....N-1 \; . \quad (3.1)$$

In (3), ϕ_u and ϕ_l are the upper and lower angles of the regions and ϕ_k, $k = 1,.....K$, are the directions where the nulls are required. Equation (2) can be employed directly in (3). Thus, the first term in (3) is employed to minimize the SLL between the desired angles whereas the second one is for having zeros in the desired directions. (3.1) gives the constraint imposed on inter-element spacing to reduce mutual coupling effects between the elements of the array antennas.

IV. APPLICATION EXAMPLES

In this section, firstly the synthesized radiation patterns of the selected papers [5-6] are performed using a full wave electromagnetic simulator (CST) which allows the prediction of the performance of antennas to very high accuracy without the need for costly trial and error constructions and measurements. In both [5] and [6], the array elements are accepted as isotropic and the desired radiation patterns are synthesized by optimizing the positions of array elements. All of the simulations are realized using half–wave dipole antennas at 2.6 GHz.

Afterwards, the same objectives for the examples of literature are achieved again but this time, by using the determined constraints for the inter-element spacings. Thus, the mutual coupling effects between antennas are minimized and the radiation patterns obtained using pattern multiplication can provide the desired radiation demands of practical applications. The results of the GPS algorithm are also validated by comparing with the results obtained using the GA for the same objective functions and restrictions. The GA is a stochastic algorithm that gives different solution sets after each run, thus the GA is run a few times with the same number of iterations of the GPS and the best results are given in this paper. The CST simulation results are also obtained for the recommended array geometries of the GPS algorithm with the aim of exhibiting the compatibility between the desired pattern and full-wave simulation result. Both the GPS and GA algorithms were implemented using MATLAB.

In [5], the authors have perturbed a -30 dB Dolph-Chebyshev initial pattern to form a null at 20^o using a 20 isotropic element linear array. The mutual coupling effects are neglected in this example. The perturbation amounts, the resulted positions of each element and also the inter-element spacings of the adjacent elements are given in Table 1.

Table 1: The excitation amplitudes and the perturbed element positions for Fig. 2

Dolph-Cheb.	$A_n(A)$	1.000 0.970 0.912 0.831 0.731 0.620 0.504 0.391 0.285 0.325
	$d_n(\lambda)$	0.250 0.750 1.250 1.750 2.250 2.750 3.250 3.750 4.250 4.750
	$d_{n+1} - d_n$	0.500 0.500 0.500 0.500 0.500 0.500 0.500 0.500 0.500 0.500
[5]	$A_n(A)$	1.000 0.970 0.912 0.831 0.731 0.620 0.504 0.391 0.285 0.325
	$d_n(\lambda)$	0.230 0.712 1.234 1.768 2.277 2.758 3.237 3.735 4.246 4.758
	$d_{n+1} - d_n$	**0.460 0.482** 0.522 0.534 0.509 **0.481 0.479 0.498** 0.511 0.512

The radiation patterns which are symmetrical with respect to the origin are given before and after optimization processes in Fig. 2 together with the CST simulation pattern.

The optimized radiation pattern is obtained using the element positions given in Table 1. Although, the desired null direction seems to be suppressed in the optimized pattern, the CST simulation pattern of the optimized array proves that the desired direction can be suppressed only a few dB. Besides, an unexpected null level is formed directed to 22^o. This amount of corruption in the expected null level and null direction is occurred because of the coupling effects between the array elements. Here, crucial differences are formed between the expected and occurred values

in the null deepness and null direction. When the element positions in Table 1 are observed, it can be seen that some of the spacings between the array elements are smaller than 0.5λ.

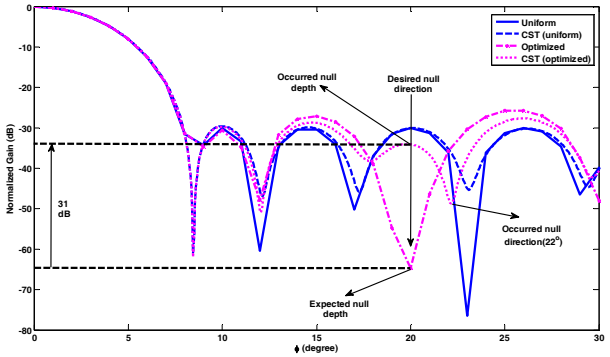

Fig. 2. Normalized radiation patterns obtained in [5] and the CST simulation pattern of the optimized array.

The spacing between the first elements about the origin is 0.46λ where the spacings between the first and second elements, between the fifth and sixth elements and between the sixth and seventh elements are 0.482λ, 0.481λ, and 0.479λ, respectively. These values are given in bold style in Table 1.

In this paper, the same objectives of [5] are achieved by using the following cost function:

$$Fitness = 20\log\left\{\max\left\{AF(\phi)\Big|_{\phi_l=8^o}^{\phi_u=90^o}\right\}\right\} + 20\log\left\{AF(20^o)\right\} \quad (4)$$

The GPS and GA algorithms are utilized to optimize (4), but this time using the determined restriction given with (3.1). The obtained solution spaces are given in Table 2 and the radiation pattern obtained using these solution spaces is given in Fig. 3.

Table 2: The excitation amplitudes and the perturbed element positions used to obtain Fig. 3

GPS	$A_n(A)$	0.250 0.750 1.250 1.787 2.338 2.838 3.338 3.838 4.338 4.990
	$d_n(\lambda)$	0.500 0.500 0.500 0.537 0.551 0.500 0.500 0.500 0.500 0.652
GA	$d_{n+1}-d_n$	0.264 0.779 1.283 1.840 2.382 2.884 3.389 3.897 4.419 5.079
	$A_n(A)$	0.528 0.515 0.504 0.557 0.542 0.502 0.505 0.508 0.522 0.660
Dolph-Cheb.	$d_n(\lambda)$	0.250 0.750 1.250 1.750 2.250 2.750 3.250 3.750 4.250 4.750
	$d_{n+1}-d_n$	0.500 0.500 0.500 0.500 0.500 0.500 0.500 0.500 0.500 0.500

It can be observed from the resulted pattern of GPS optimizer that a very deep null is achieved successfully in the 20^o direction. Although the null level is also easily achieved using GA, the MSLL of GA pattern is slightly higher than the GPS pattern level in the desired null direction.

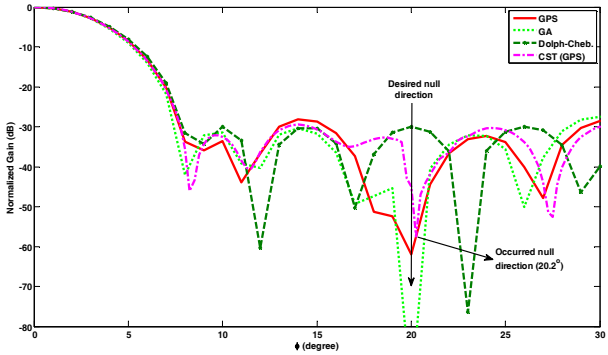

Fig. 3. Normalized radiation patterns optimized using the GPS and the GA algorithms with the CST simulation pattern of the optimized array.

As it is observed from Fig. 3, the resulted CST simulation pattern follows the features of the GPS pattern approximately in the all visible region. Besides, the CST simulation pattern has achieved a deep null level in the desired null direction which can be accepted as zero level for the practical applications.

In the second example [6], the authors have perturbed the positions of a 28 isotropic element array to achieve null levels at 30^o, 32.5^o, and 35^o. The mutual coupling effects are also neglected in this example. The perturbation amounts, the resulted positions of each element and also the inter-element spacings of the adjacent elements are given in Table 3.

Table 3: The excitation amplitudes and the perturbed element positions for Fig. 4

Uni-form	$A_n(A)$	1.000 1.000 1.000 1.000 1.000 1.000 1.000 1.000 1.000 1.000 1.000 1.000 1.000 1.000
	$d_n(\lambda)$	0.250 0.750 1.250 1.750 2.250 2.750 3.250 3.750 4.250 4.750 0.525 0.575 0.625 0.675
	$d_{n+1}-d_n$	0.500 0.500 0.500 0.500 0.500 0.500 0.500 0.500 0.500 0.500 0.500 0.500 0.500 0.500
[6]	$A_n(A)$	1.000 1.000 1.000 1.000 1.000 1.000 1.000 1.000 1.000 1.000 1.000 1.000 1.000 1.000
	$d_n(\lambda)$	0.280 0.780 1.220 1.750 2.270 2.740 3.265 3.770 4.195 4.750 5.315 5.710 6.160 6.840
	$d_{n+1}-d_n$	0.560 0.500 **0.440** 0.530 0.520 **0.470** 0.525 0.505 **0.425** 0.555 0.565 **0.395** **0.450** 0.680

The radiation patterns before and after the optimization process are given in Fig. 4 together with the CST simulation patterns. The optimized radiation pattern is obtained using the array geometry given in Table 3. The desired null directions are achieved in [6] by using isotropic

elements, thus by neglecting the mutual coupling effects. The CST simulation pattern shows that the expected and occurred null levels are quite different as illustrated in Fig. 4.

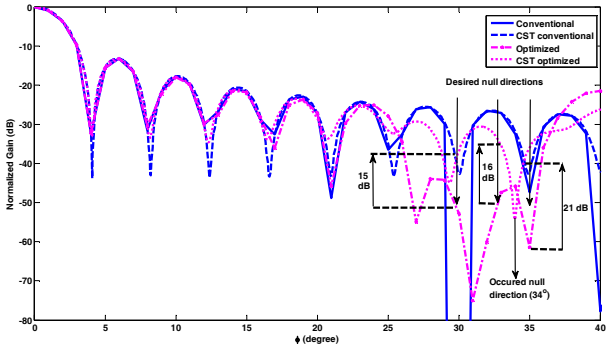

Fig. 4. Normalized radiation patterns obtained in [6] and the CST simulation pattern of the optimized array.

An only null level is formed directed to 34^o rather than the expected three null directions. It is obvious that this array geometry cannot be used in a real world problem to obtain nulls in the desired directions. When the element positions in Table 3 are investigated, it can also be seen that many of the spacings between the elements are smaller than 0.5λ. The first and second elements is 0.44λ, between the fifth and sixth elements is 0.47λ, between the eighth and ninth elements is 0.425λ, between the eleventh and twelfth elements is 0.395λ, and between the twelfth and thirteenth elements is 0.45λ. These values are given in bold style in Table 3.

In the second implementation, the following cost function is arranged to achieve the same objectives of [6]:

$$Fitness = 20\log\left\{AF(30^o)\right\} + 20\log\left\{AF(32.5^o)\right\} + 20\log\left\{AF(35^o)\right\} + 20\log\left\{max\left\{\left|AF(\varphi)\right|_{\varphi_l=4^o}^{\varphi_u=90^o}\right\}\right\}. \quad (5)$$

The cost function is optimized using both the GPS and GA algorithms but this time with the determined restrictions in (3.1). The optimized element positions are given in Table 4 and the radiation pattern obtained using these element positions is given in Fig. 5.

It is obvious from Fig. 5 that the null levels and directions are easily achieved with both GPS and GA algorithms. Besides, the close-in sidelobes are almost the same for both the GPS and the GA, but the far sidelobes are better for the GPS. As it is observed from Fig. 5, the resulted CST simulation pattern follows the features of the GPS pattern in the close-in sidelobes and the maximum level of -40 dB is occurred in the desired null directions. It can be said that, by our improvements in this paper, the disagreement between the desired pattern and the CST simulation pattern can be prevented, thus the obtained array geometries can achieve the desired radiation patterns also when used in practical applications.

Table 4: The excitation amplitudes and the perturbed element positions used to obtain Fig. 5

GPS	$d_n(\lambda)$	0.250 0.750 1.311 1.811 2.311 2.811 3.461 3.962 4.461 4.961 5.772 6.272 6.772 7.273
	$d_{n+1}-d_n$	0.500 0.500 0.566 0.500 0.500 0.500 0.650 0.501 0.499 0.500 0.811 0.500 0.500 0.501
GA	$d_n(\lambda)$	0.252 0.752 1.251 1.754 2.257 2.756 3.284 3.792 4.291 4.790 5.463 5.965 6.465 7.094
	$d_{n+1}-d_n$	0.504 0.500 0.499 0.503 0.503 0.499 0.528 0.508 0.499 0.499 0.673 0.502 0.500 0.629
Dolph-Cheb.	$d_n(\lambda)$	0.266 0.800 1.333 1.866 2.400 2.933 3.466 4.000 4.533 5.066 5.600 6.133 6.666 7.200
	$d_{n+1}-d_n$	0.532 0.534 0.533 0.533 0.534 0.533 0.533 0.534 0.533 0.533 0.534 0.533 0.533 0.534

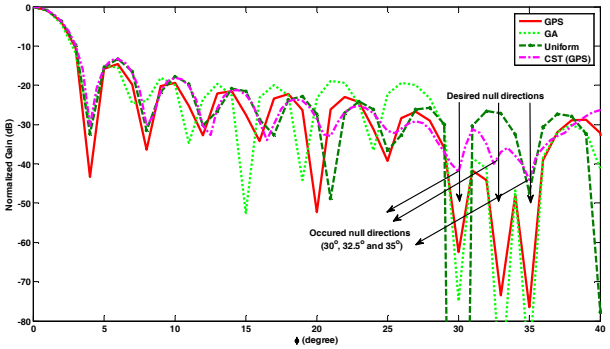

Fig. 5. Normalized radiation patterns optimized using the GPS and the GA algorithms with the CST simulation pattern of the optimized array.

VI. CONCLUSION

This paper illustrated the corruptions in the desired radiation patterns of non-uniform antenna arrays due to the mutual coupling effects between the array elements. Two examples from literature are utilized to demonstrate the disagreement between the desired and occurred radiation patterns. In our paper, it is confirmed that a non-uniform array geometry synthesized by neglecting the coupling effects cannot be used in real world applications.

We have achieved the same objectives of the selected papers with the determined inter-element spacing restrictions (3.1) using the GPS algorithm.

The GPS is a direct, efficient derivative-free algorithm for searching minima of the functions. By our improvements in this paper, we prevent the disagreement between desired pattern and the resulted pattern using the necessary restrictions for the inter-element spacings. Thus, the radiation patterns obtained using pattern multiplication can provide the desired radiation demands of practical applications. The verification of this approach is carried out by comparing the results of CST software.

REFERENCES

[1] K. K. Yan and Y. L. Lu, "Sidelobe Reduction in Array Pattern Synthesis using Genetic Algorithm," *IEEE Trans. Antennas Propagat.*, vol. 45, pp. 1117–1122, 1997.

[2] G. K. Mahanti, N. Pathak, and P. Mahanti, "Synthesis of Thinned Linear Antenna Arrays with Fixed Sidelobe Level Using Real-Coded Genetic Algorithm," *Progress In Electromagnetics Research,* vol. 75, pp. 319–328, 2007.

[3] G. K. Mahanti, A. Chakrabarty, and S. Das, "Phase-Only and Amplitude-Phase Only Synthesis of Dual-Beam Pattern Linear Antenna Arrays Using Floating-Point Genetic Algorithms," *Progress In Electromagnetics Research*, vol. 68, pp. 247–259, 2007.

[4] F. Gunes and F. Tokan, "Pattern Search Optimization with Applications on Synthesis of Linear Antenna Arrays," *Expert Systems with Applications*, vol. 37, pp. 4698–4705, 2010.

[5] T. H. Ismail and M. M. Dawoud, "Null Steering in Phased Arrays by Controlling the Element Positions," *IEEE Transactions on Antennas and Propagat*, vol. 39, pp. 1561–1566, 1991.

[6] M. M. Khodier and C. G. Christodoulou, "Linear Array Geometry Synthesis with Minimum Sidelobe Level and Null Control Using Particle Swarm Optimization," *IEEE Transactions on Antennas and Propagat*., vol. 53, pp. 2674–2679, 2005.

[7] V. Murino, A. Trucco, and C. S. Regazzoni, "Synthesis of Unequally Spaced Arrays by Simulated Annealing," *IEEE Transactions on Signal Processing*, vol. 44, pp. 119–127, 1996.

[8] D. W. Boeringer and D. H. Werner, "Particle Swarm Optimization Versus Genetic Algorithms for Phased Array Synthesis," *IEEE Transactions on Antennas and Propagat*., vol. 52, pp. 771–779, 2004.

[9] K. R. Mahmoud, M. I. Eladawy, R. Bansal, S. H. Zainud-Deen, and S. M. M. Ibrahem, "Analysis of Uniform Circular Arrays for Adaptive Beamforming Applications Using Particle Swarm Optimization Algorithm," *International Journal of RF and Microwave Computer-Aided Engineering*, vol. 18, pp. 42–52, 2008.

[10] K. Guney, B. Babayigit, and A. Akdagli, "Interference Suppression of Linear Antenna Arrays by Phase-Only Control Using a Clonal Selection Algorithm," *Journal of the Franklin Institute*, vol. 345, pp. 254–266, 2008.

[11] W. Choi, T. K. Sarkar, O. Allen, and J. Asvestas, "Approximate Compensation for Mutual Coupling in a Direct Data Domain Least Squares Approach using the In-situ Measured Element Patterns," *Applied Computational Electromagnetic Society (ACES) Journal*, vol. 21, no. 3, pp. 342–352, 2006.

[12] V. N. S. Kalaga and M. Hamid, "On The Optimum Directivity of Dipole Arrays Considering Mutual Coupling," *Applied Computational Electromagnetic Society (ACES) Journal*, vol. 23, no. 2, pp. 155–165, 2008.

[13] F. Hutu, S. Cauet, and P. Coirault, "Robust Synchronization of Different Coupled Oscillators: Application to Antenna Arrays," *Journal of the Franklin Institute*, vol. 346, pp. 413-430, 2009.

[14] K. Guney and A. Akdağlı, "Null Steering of Linear Antenna Arrays Using a Modified Tabu Search Algorithm," *Progress In Electromagnetics Research*, vol. 33, pp. 167-182, 2001.

[15] V. Torczon, "On the Convergence of Pattern Search Algorithms," *SIAM Journal on Optimization*, vol. 7, pp. 1–25, 1997.

[16] R. M. Lewis and V. Torczon, "Pattern Search Algorithms for Bound Constrained Minimization," *SIAM Journal on Optimization*, vol. 9, pp. 1082–1099, 1999.

[17] R. M. Lewis and V. Torczon, "Pattern Search Methods for Linearly Constrained Minimization," *SIAM Journal on Optimization*, vol. 10, pp. 917–941, 2000.

[18] R. M. Lewis and V. Torczon, "A Globally Convergent Augmented Lagrangian Pattern Search Algorithm for Optimization with General Constraints and Simple Bounds," *SIAM Journal on Optimization*, vol. 12, pp. 1075–1089, 2002.

[19] T. G. Kolda, R. M. Lewis, and V. Torczon, "Optimization by Direct Search: New Perspectives on Some Classical and Modern Methods," *SIAM Rev.*, vol. 45, pp. 385–482, 2003.

[20] C. Bogani, M. G. Gasparo, and A. Papini, "Generalized Pattern Search Methods for a Class of Nonsmooth Optimization Problems with Structure," *Journal of Computational and Applied Mathematics*, vol. 229, pp. 283–293, 2009.

[21] R. S. Elliott, Antenna Theory and Design, Prentice-Hall, 1981.

Fikret Tokan received the M.S. degree in Electronics and Communications Engineering from the Yıldız Technical University in 2005 and Ph.D. degree from the Yıldız Technical University, Istanbul, in Communications Engineering in 2010.

He has been currently working as a researcher in Yıldız Technical University. His current research interests are electromagnetic waves, propagation, antenna arrays, scattering, and numerical methods.

Filiz Güneş received her MSc degree in electronic and communication engineering from the Istanbul Technical University. She attained her PhD degree in communication engineering from the Bradford University in 1979.

She is currently a full professor in Yıldız Technical University. Her current research interests are in the areas of multivariable network theory, device modeling, computer-aided microwave circuit design, monolithic microwave integrated circuits, and antenna arrays.

Reduction of Sensitivity to Measurement Errors in the Derivation of Equivalent Models of Emission in Numerical Computation

Xin Tong, David W. P. Thomas, Angela Nothofer, Christos Christopoulos, and Phillip Sewell

George Green Institute for Electromagnetics Research
University of Nottingham, Nottingham, NG2 7RD, UK
vanppp@gmail.com, dave.thomas@nottingham.ac.uk, angela.nothofer@nottingham.ac.uk,
phillip.sewell@nottinham.ac.uk, christos.christopoulos@nottingham.ac.uk

Abstract ─ In this paper, the accuracy of an equivalent dipole model for representing electromagnetic emissions from printed circuit boards (PCB) is studied. The optimization of near-field measurement parameters and required PCB parameters for building a numerical model are discussed and their impact on the accuracy of emission predictions is examined.

Index Terms ─ Error analysis, near field scanning, numerical modelling, radiated fields.

I. INTRODUCTION

Predicting electromagnetic emissions from PCBs is an important topic in electromagnetic compatibility (EMC) studies and product designs. Simulation techniques based on equivalent models have many advantages compared to the full field simulations. The heavy task of modeling the complexity of PCBs and the huge computational costs to solve the model are alleviated. In addition, detailed information on circuit structure is not needed to model emissions from PCBs by equivalent sources. This ensures simplicity, confidentiality of designs and facilitates the task of design engineers.

A method to represent radiated emissions from a PCB using an equivalent dipole model deduced from a magnetic near-field scan was described in [1]. Modeling techniques in both open and closed environments were considered. A PCB is modeled with a set of equivalent magnetic dipoles placed on the component surface. The ground plane is also explicitly included in the model based on certain approximations in order to simulate the emissions in the whole space. In closed environments, the method is extended to include dipoles, dielectric, and conducting plane (DDC model) to explicitly represent the physical presence of the PCB. Thus, the major interactions between the PCB and enclosure are taken into account. The equivalent dipoles are identified by fitting the measured tangential magnetic near fields to the fields generated by the dipoles. The modeling process can then be described as:

1. Take a near field scan of the transverse magnetic fields emitted by the PCB.
2. Through solving the inverse problem (see equation (4)) find the equivalent dipoles for the PCB.
3. Model the PCB in the environments of interest (enclosures or free space) to predict its performance.

Figure 1 shows the simple test board used where comparisons with full 3D simulations are required. The configuration used for the basic test board is given in Table 1 and typical results are shown in Fig. 2.

For the near-field scanning based method, measurement parameters (scanning surface, sampling, distance, error analysis, etc.) have noticeable effects on the accuracy of associated modeling and simulation. Optimization of measurement parameters not only improves the efficiency of near-field scanning, but also reduces the modeling errors possibly introduced from

Submitted On: May 20, 2011
Accepted On: July 28, 2011

measurements. An early overview of determination of measurement parameters can be found in [2]. The sampling and scan-plane reduction techniques are developed from the electromagnetic propagation theory in [3] and [4], respectively. In [5, 6], extensive error analysis for near-field measurements is performed using measurement tests, simulation tests, and mathematical analysis. For the proposed method, it is essential to specifically optimize the parameters of the required planar near-field measurements based on the electromagnetic theory and measurement or simulation tests, as well as to have an error budget of the numerical modeling and associated measurements.

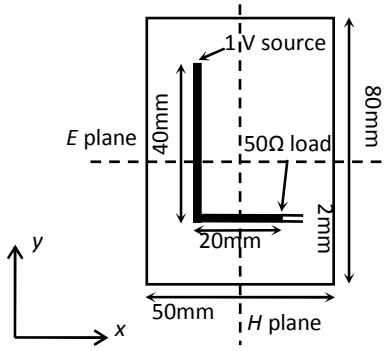

Fig. 1. Geometry of the basic test board (top view).

Table I: Configuration of near-field measurement with the test board

frequency (GHz)	1
scanning plane height (mm)	11.5 above the PCB
scanning plane size (mm)	120 × 75
scanning resolution (mm)	2.5
sampling points	49 × 31

In this paper, the optimization of the near-field measurement parameters for the model is discussed. Finally, error and uncertainty in the numerical modeling and associated measurements are examined. With these studies, the objective is to develop the methodology of modeling electromagnetic emissions using equivalent dipoles deduced from near-field scanning as completely as possible, and to show how the technique described here meets the needs for predictive work in EMC studies.

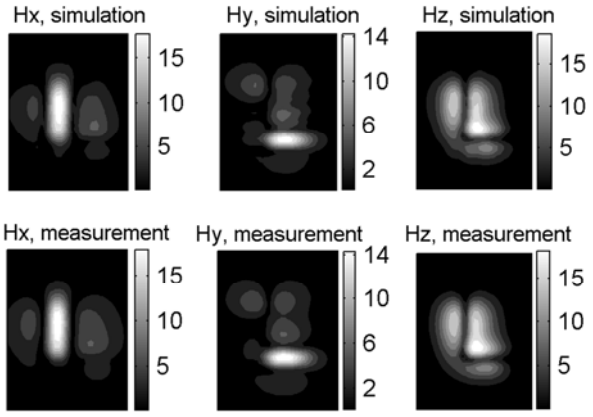

Fig. 2. Magnetic fields (mA/m) in the scanning plane at 1 GHz. Top row) simulation based on equivalent dipoles; bottom row) measurement.

II. EFFECTS OF MEASUREMENT PARAMETERS

For the near-field scanning based method, the measurement parameters have noticeable effects on the accuracy of modeling and simulation. Knowledge of these effects helps to determine the choice of measurement configuration. Scanning resolution, scanning plane area, and SNR are critical parameters in near-field sampling. To study this, a far-field simulation in the E plane for the basic test board is repeated using the equivalent dipole method with different measurement parameters, and the correlation coefficient between results obtained by the equivalent dipole simulation and the full field simulation is introduced as a measure of accuracy. The correlation coefficient is defined as:

$$\gamma = \frac{\sum_{i=1}^{N}(E_i-\bar{E})(E'_i-\overline{E'})}{\sqrt{\sum_{i=1}^{N}(E_i-\bar{E})^2 \sum_{i=1}^{N}(E'_i-\overline{E'})^2}}, \quad (1)$$

where E_i is the dipole equivalent result set, E'_i is the full field simulation result set, $\bar{E}_i$ and $\overline{E'_i}$ are the averages of E_i and E'_i, respectively, and N is the number of samples. All full field simulations are performed with a method of moment (MoM) based solver Concept – II 9.4 [7, 8].

A. Scanning resolution

According to the information theory, the scanning resolution is a key factor in acquiring sufficient near-field information. In the examples above, a 2.5 mm resolution is used for both PCBs. This is based on the sampling criterion recommended by Joy and Paris [3] which estimates the maximum spacing between sampling points (Δs) allowed to obtain sufficient information for planar near-field scanning as:

$$\Delta s = \frac{\lambda}{2\sqrt{1+(\lambda/d)^2}}, \qquad (2)$$

where λ is the wavelength and d is the separation distance between the EUT and the probe. The maximum spacing allowed for the test boards considered according to (2) is 5.7 mm and 6.0 mm, respectively. So the choice of 2.5 mm is reasonable. To validate this criterion, the far field prediction of the test board is repeated with the same set of near-field data but of different resolutions, and the correlation coefficient with full field simulation is shown in Fig. 3. The results from near-field data of 2.5 and 5 mm resolution make very little difference and are close to the direct simulation result, as they are within the range of maximum space allowed. But the data with a 10 mm resolution and above has obvious inaccuracies as indicated by the lower correlation. This confirms the criterion for the choice of sampling points that any space sampling less than the maximum spacing allowed in (2) is sufficient.

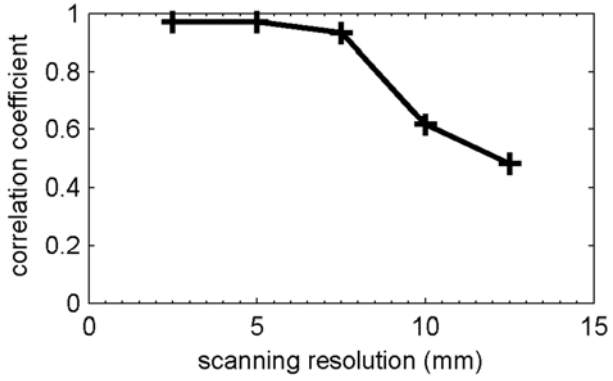

Fig. 3. Effects of scanning resolution.

B. Scanning plane area

Another important topic with regard to near-field sampling is the size of scanning plane. Unlike the modal expansion method, the method presented here does not assume the field outside the scanning area to be zero. The equivalent sources are established by fitting to the measured near-field data. Therefore if any significant field area is not covered in the near-field scanning plane, some information will be lost and the equivalent sources established from it would have a noticeable error. It is well known that magnetic near-field maps from a PCB are dominated by the fields vertically above the board and gradually become weaker as the sampling point extends outward to the perimeter of the PCB [9, 10]. This implies that the scanning area must at least cover the area of the PCB, and could possibly extend beyond it. Ideally, the scanning plane should extend until the field on the edges of the plane reaches the minimum measurable level (noise floor) of the equipment. But in practice it is not necessary to scan so widely in order to collect sufficient near-field information. Based on our studies, a near-field plane where the maximum field on the edges is approximately 20 dB lower than the overall maximum field is required. Figure 4 shows the effects of scanning the area size on the far field prediction for the test board. It is found that insufficient scanning information (when there is 5 and 10 dB maximum – edge difference) results in significant inaccuracies, but the far field is correctly predicted when the scanning plane reaches a large enough size (19 and 28 dB maximum – edge difference).

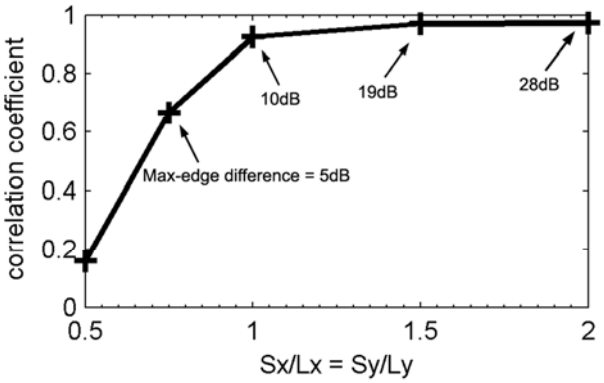

Fig. 4. Effects of scanning area. Sx, Sy: length of the scanning plane in x and y direction, respectively. Lx, Ly: length of the PCB in x and y direction, respectively.

Actually, the plane area required to satisfy this criterion is not very large. In the case above, a 19 dB maximum – edge difference corresponds to a plane which is 1.5 times of the PCB dimension (100 × 75 mm). This result also implies that when a scanning plane is large enough, further increasing its size does not significantly improve the accuracy of the equivalent source method.

C. Substrate permittivity

Knowledge of the permittivity of the PCB substrate is needed when constructing the complete DDC model for simulations in closed environments. The most accurate way is to measure it experimentally, but not every EMC lab has the required equipment. Normally, PCB manufacturers provide general information on the substrate. In practice, the actual value may differ due to manufacturing uncertainties, constructional details, etc. It is therefore necessary to establish how accurate the value of permittivity should be for inclusion in the model. As a quantitative study, the vertical electric field along two orthogonal lines within an enclosure at a non-resonant frequency (1 GHz) is predicted with equivalent models built with different values of permittivity, and the correlation coefficients with results obtained from full field simulation are shown in Fig. 5. The typical value of the substrate permittivity is 4.6 (FR4). The predicted field is in an acceptable range provided that the permittivity value used for modeling is within 20% of the actual value. This implies that an accurate enough model can be built for most EMC studies as long as the general type of the dielectric substrate is known.

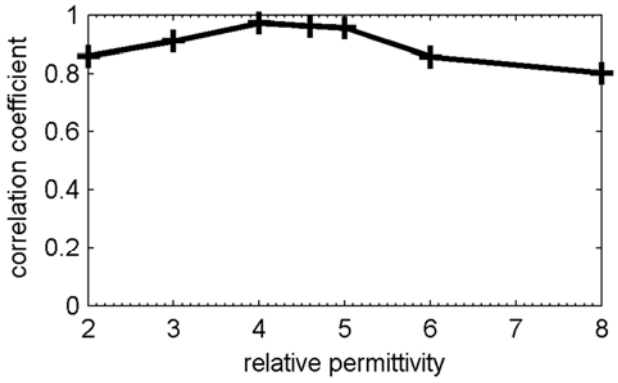

Fig. 5. Effects of modeled permittivity value.

III. ERROR AND UNCERTAINTY

A. Measurement errors

The errors due to the measurement system are recognized as the major error source of near-field techniques. Generally, there are three categories of error source, related to the probe δ_p, receiver δ_r, and test conditions δ_t. The probe related errors include positioning error, antenna factor error, and multiple reflection error. The 3D positioner in our scanning system has a mechanical precision of 10 μm in x, y, and z direction which is much smaller than the RF wavelength, so the probe positioning error can be considered negligible. The antenna factor error depends on the probe's polarization properties relative to those of the EUT. This error is examined by two methods: a) experiments where the ratio of the primary and cross-polar components of a known field coupled to the probe is measured [11], and b) simulations where a probe of typical dimensions and structure subject to an incident arbitrary but known field is modeled to find out its polarization properties. The two studies give similar results that a typical probe parameter error with our setup at RF frequencies is approximately $\delta_{p1} \leq 0.15$ dB. The errors due to multiple reflections between the scanned PCB and probe are examined from simulations. An infinite ground plane and a loop probe of typical dimensions are modeled to represent the possibly largest reflections. Based on the simulation, a typical upper bound of multiple reflections error at RF frequencies is approximately $\delta_{p2} \leq 0.1$ dB.

Errors related to the receiver (arising from dynamic range, nonlinearity, mismatch, systematic random errors, etc.) and test conditions have been extensively studied by other authors [5, 6]. Based on their studies and the performance of our equipment (HP E8362B [12]), the two categories of errors have upper bounds $\delta_r \leq 0.25$ dB and $\delta_t \leq 0.1$ dB. If the errors are assumed to be independent, according to the central limit theorem the total error budget in near-field scanning for PCBs with our measurement system can be estimated as

$$\delta = \sqrt{\sum \delta_i^2} \leq 0.35 \text{ dB}. \qquad (3)$$

B. Numerical accuracy

The effects of measurement errors on the calculated dipoles through the numerical computation are examined here. The moments of the equivalent dipoles are numerically determined from the inverse problem of a linear equation system

$$\xi.\bar{M}e^{i\bar{\theta}} = \bar{H}e^{i\bar{\phi}}, \tag{4}$$

where ξ is the coefficient matrix, $\bar{M}$ and $\bar{\theta}$ are vectors of the amplitude and phase of equivalent dipoles, and $\bar{H}$ and $\bar{\phi}$ are vectors of the amplitude and phase of measured magnetic fields. ξ has exact values but $\bar{H}e^{i\bar{\phi}}$ contains inevitable errors $\overline{\Delta H}$ and $\overline{\Delta\phi}$, leading to errors in the resulting dipole moments. The linear equation system becomes:

$$\xi.\left(\bar{M}e^{i\bar{\theta}} + \Delta\bar{M}\right) = (\bar{H} + \overline{\Delta \mathrm{H}})e^{i(\bar{\phi}+\overline{\Delta\phi})} = \left[\bar{H}e^{i\overline{\Delta\phi}} + \overline{\Delta H}e^{i\overline{\Delta\phi}}\right]e^{i\bar{\phi}}. \tag{5}$$

The right-hand side can be Taylor expanded with only terms of first and second order retained.

$$\xi.\left(\bar{M}e^{i\bar{\theta}} + \Delta\bar{M}\right) = \bar{H}e^{i\bar{\phi}} + \left(\overline{\Delta H} + i\bar{H}\overline{\Delta\phi} + \mathrm{i}\overline{\Delta H\Delta\phi} - \bar{H}\overline{\Delta\phi^2}/2\right)e^{i\bar{\phi}}. \tag{6}$$

From (4) and (6), we can obtain

$$\overline{\Delta M} = \xi^{-1}.\left(\overline{\Delta H} + i\bar{H}\overline{\Delta\phi} + \mathrm{i}\overline{\Delta H\Delta\phi} - \bar{H}\overline{\Delta\phi^2}/2\right)e^{i\bar{\phi}}, \tag{7}$$

$$\|\overline{\Delta M}\| = \|\xi^{-1}\|.\left\|\left(\overline{\Delta H} + i\bar{H}\overline{\Delta\phi} + \mathrm{i}\overline{\Delta H\Delta\phi} - \bar{H}\overline{\Delta\phi^2}/2\right)e^{i\bar{\phi}}\right\|. \tag{8}$$

From (4), we can also obtain

$$\|\xi\|.\left\|\bar{M}e^{i\bar{\theta}}\right\| \geq \left\|\bar{H}e^{i\bar{\phi}}\right\|. \tag{9}$$

Therefore, the upper bound of relative error in the equivalent dipoles due to measurement errors can be expressed by combining (8) and (9) as

$$\frac{\|\overline{\Delta M}\|}{\|\bar{M}\mathrm{e}^{\mathrm{i}\bar{\theta}}\|} \leq cond(\xi).\frac{\left\|\left(\overline{\Delta H} + i\bar{H}\overline{\Delta\phi} + \mathrm{i}\overline{\Delta H\Delta\phi} - \bar{H}\overline{\Delta\phi^2}/2\right)e^{i\bar{\phi}}\right\|}{\|\bar{H}\mathrm{e}^{\mathrm{i}\bar{\Phi}}\|}, \tag{10}$$

where $cond(\xi) = \|\xi^{-1}\|.\|\xi\|$ is the condition number of the matrix ξ [13]. $\overline{\Delta H}$ and $i\overline{H\Delta\phi}$ in the right hand side represent the dominant error terms in measured magnitude and phase, respectively. Due to the fact that the condition number of a matrix is always ≥1, the small errors in measurement may be magnified in the resulted equivalent dipole array. Mathematically this situation is called an ill-conditioned equation system. In order to keep a high numerical accuracy, numerical methods such as the L-curve method and singular valued decomposition [14] have to be applied to solve the equations.

C. Uncertainty tests

Efficient computational techniques are expected to avoid the measurement errors being magnified in the resulted equivalent dipole array. But it is still worth examining to what extent the measurement errors (with a typical upper bound 0.35 dB) would affect the accuracy of the model. To study this, the far field of the basic test board is predicted with near-field data with different levels of normally distributed noise as well as a reference with no intentionally added noise. As the noise is randomly generated, the results may differ from one time to another. Figure 6 shows an example illustrating the general idea. A standard deviation 0.35 dB of the measured near field leads to an uncertainty ±1 dB in the far field prediction. As a comparison, a greater error of a standard deviation 1 dB leads to a larger uncertainty (±2 dB). Particularly, most uncertainties occur in places where the field intensity is relatively weak. Measurement errors are magnified from near-field data to the predicted far fields.

Equation (10) links the possibly largest overall errors to a number of factors. Our tests suggest that experimental errors are of the order of 0.35 dB and that overall errors are of the order of 1 dB. This confirms the magnification of errors as indicated by (9) which in our case is a factor of the order of 0.7 dB (×1.2). This factor will vary depending on the choice of sampling points, the technique for numerically solving the equation system, etc. as indicated by the various terms in (9). The discussion following (9), gives some

guidance as to the impact of various solution techniques to the problem accuracy. Results published for predicted fields in enclosures [1] show similar accuracy although errors in the definition of the enclosure will also contribute to the error budget.

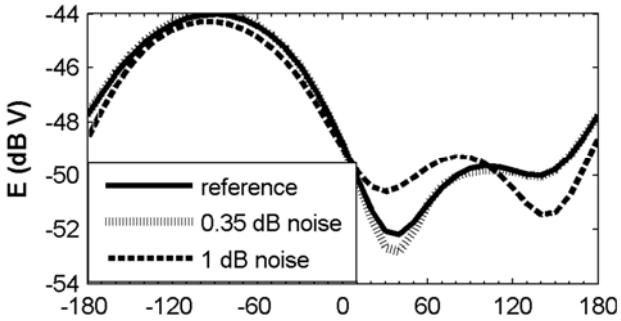

Fig. 6. Far-field patterns calculated from data with different levels of noise.

IV. CONCLUSION

Verification and validation studies of the equivalent dipole model for predicting electromagnetic emission from PCBs are presented. Case studies with two test boards show the validity of the model in both free space and enclosed environments. The optimization of near-field measurement parameters and their impact on prediction accuracy are demonstrated. It has been shown that the inclusion of basic structural details of ground plane and substrate in addition to the equivalent dipoles permit fairly accurate prediction of emitted fields to be made not only in free space but also in enclosures that have interactions with the PCBs inside.

Generally, the method has better performance in free space than in enclosed environments. This may be attributed to the greater degree of approximations made to the model in enclosed environments. The real current distribution of the PCB is also assumed to be the same in free space and enclosed environments. This may be true in most but not all cases. In a highly populated enclosure (several PCBs in close proximity), stronger interactions may be present and the model may display a lower accuracy. Nevertheless, we have demonstrated that the proposed techniques have the potential to characterize emissions from complex structures in realistic environments reducing computational effort significantly and making it possible to perform complete system EMC studies.

Future work will look at more complex multilayered and double sided PCBs where board resonance effects are more noticeable [15]. Evaluation of the application of these measurement uncertainties to other field solvers will also be investigated [16].

ACKNOWLEDGMENT

The work was supported by the EPSRC UK Grant No: EP/D048540/1.

REFERENCES

[1] X. Tong, D. W. P. Thomas, A. Nothofer, P. Sewell, and C. Christopoulos, “Modeling Electromagnetic Emissions From Printed Circuit Boards in Closed Environments Using Equivalent Dipoles,” *IEEE TRANS. ON EMC*, vol. 52, no. 2, pp. 462-470, May 2010.

[2] A. D. Yaghjian, "An Overview of Near-Field Antenna Measurement," *IEEE Trans. Antennas Propagat.*, vol. AP-34, pp. 30-45, Jan. 1986.

[3] E. B. Joy and D. T. Paris, "Spatial Sampling and Filtering in Near-Field Measurements," *IEEE Trans. Antennas Propagat*., vol. AP-20, pp. 253-261, May 1972.

[4] D. J. Van Rensburg, "Scan-Plane Reduction Techniques for Planar Near-Field Antenna Measurements," *IEEE Trans. Antennas Propagat.,* vol. 46, no. 6, pp. 179-184, Dec. 2004.

[5] A. C. Newell, "Error Analysis Techniques for Planar Near-Field Measurements," *IEEE Trans. Antennas Propagat.,* vol. 36, no. 6, pp. 754-768, Jun. 1988.

[6] A. C. Newell and C. F. Stubenrauch, "Effect of Random Errors in Planar Near-Field Measurement," *IEEE Trans. Antennas Propagat.,* vol. 36, no. 6, pp. 769-773, Jun. 1988.

[7] A. F. Peterson, S. L. Ray, and R. Mittra, “Computational Methods for Electromagnetics,” Wiley: IEEE Press, 1997.

[8] Concept - II homepage. [Online]. Available:http://www.tet.tu-harburg.de/concept/index.en.html (2009)

[9] R. G. Kaires, "Radiated Emissions from Printed Circuit Board Traces Including the Effect of Vias, as a Function of Source,

Termination, and Board Characteristics," *IEEE International Symposium on EMC*, pp. 872 – 877, 1988.

[10] R. Garg, P. Bhartia, I. Bahl, and A. Ittipiboon, Microstrip Antenna Design Handbook. Norwood, MA: Artech House, 2001.

[11] D. W. P. Thomas, K. Biwojno, X. Tong, A. Nothofer, P. Sewell, and C. Christopoulos, "Measurement and Simulation of the Near-Field Emissions from Microstrip Lines," *in Proc. EMC Europe* 2008, pp. 1-6, Sep. 2008.

[12] HP E8362B User's Guide, Hewlett-packard Co. Santa Rosa, CA, 2000.

[13] G. Allaire, S. M. Kaber, "Numerical Linear Algebra," New York: Springer, 2008.

[14] P. C. Hansen, "Numerical Tools for Analysis and Solution of Fredholm Integral Equations of the First Kind," Inverse Problem 8, pp. 849-872, 1992.

[15] S. Kahng, "Predicting and Mitigating Techniques of the PCB RectangularPower/Ground Planes' Resonance Modes," *Applied Computational Electromagnetic Society (ACES) Journal*, vol. 22, no. 3 pp. 15-23, Nov. 2007.

[16] J. Carlsson, P-S. Kildal, "User-Friendly Computer Code for Radiated Emission and Susceptibility Analysis of Printed Circuit Boards," *Applied Computational Electromagnetic Society (ACES) Journal*, vol. 14, no. 1, pp. 1-8, March 1999.

Xin Tong was born in Hunan, China, in December 1984. He received the B.Sc. degree in Engineering Physics from Tsinghua University, Beijing, China, in 2006. He is currently working toward the Ph.D. degree in Electronic Engineering at the University of Nottingham, Nottingham, UK.

His research interests include modeling and experimental methods in electromagnetic compatibility (EMC), more particularly the characterization of emissions.

David W. P. Thomas received the B.Sc. degree in Physics from Imperial College of Science and Technology, the M.Phil. degree in Space Physics from Sheffield University, and the Ph.D. degree in Electrical Engineering from Nottingham University, in 1981, 1987 and 1990, respectively. In 1990 he joined the Department of Electrical and Electronic Engineering at the University of Nottingham as a Lecturer where he is now an Associate Professor and Reader in Electromagnetic Applications. His research interests are in power system transients, power system protection, electromagnetic compatibility and electromagnetic simulation. He is a member of CIGRE and convenor for JWG 4.207

Angela Nothofer was born in Uelzen, Germany, in 1967. She received the Dipl.-Ing. degree in Electrical Engineering from the University of Hannover, Germany, in 1995, and the D.Phil. degree in Electronics from the University of York, U.K., in 2001.

In 2000, she joined the National Physical Laboratory, U.K., where she developed standards and methods for measuring electromagnetic field strength as a member of the RF & Microwave Team. Her main research was in EMC measurement methods above 1 GHz using GTEM cells and fully anechoic rooms (FAR).

In 2005, she joined the George Green Institute for Electromagnetics Research (GGIEMR) at the University of Nottingham as a Lecturer in Electromagnetic Applications. Her main research areas are electromagnetic compatibility (EMC), and RF and microwave measurements using TEM waveguides, fully anechoic rooms, and re-verberation chambers.

Christos Christopoulos was born in Patras, Greece in 1946. He received the Diploma in Electrical and Mechanical Engineering from the National Technical University of Athens in 1969 and the M.Sc. and

D.Phil. from the University of Sussex in 1979 and 1974, respectively.

In 1974, he joined the Arc Research Project of the University of Liverpool and spent two years working on vacuum arcs and breakdown while on attachments at the UKAEA, Culham Laboratory. In 1976, he joined the University of Durham as a Senior Demonstrator in Electrical Engineering Science. In October 1978, he joined the Department of Electrical and Electronic Engineering, University of Nottingham, where he is now Professor of Electrical Engineering and Director of the George Green Institute for Electromagnetics Research (GGIEMR).

His research interests are in Computational Electromagnetics, Electromagnetic Compatibility, Signal Integrity, Protection and Simulation of Power Networks, and Electrical Discharges and Plasmas. He is the author of over 400 research publications and seven books and seven chapter contributions in books. He has received the Electronics Letters, the Snell Premium and the Measurement and Technology Premium by the IET and several conference best paper awards. He is a member of the IET and an IEEE Fellow. He is past Executive Team Chairman of the IEE Professional Network in EMC and Associate Editor of the IEEE EMC Transactions. He is Chairman of URSI Commission E on the Electromagnetic Environment and Interference and Fellow of the Royal Academy of Engineering.

Phillip Sewell received the B.Sc. degree in Electrical and Electronic Engineering (first-class honors) and Ph.D. degree from the University of Bath in 1988 and 1991, respectively.

From 1991 to 1993, he was a Post-Doctoral Fellow with the University of Ancona, Ancona, Italy. In 1993, he became a Lecturer with the School of Electrical and Electronic Engineering, University of Nottingham, Nottingham, U.K. In 2001 and 2005, he became a Reader and Professor of Electromagnetics at the University of Nottingham.

Study on Coupling Characteristics of Electromagnetic Wave Penetrating Metallic Enclosure with Rectangular Aperture

Gang Wu, Zhi-Qiang Song, Xin-Gang Zhang, and Bo Liu

Xi'an division of China Academy of Space Technology
Xi'an 710100, Shaanxi, P. R. China
woogung@126.com, 17151320@qq.com, xinkou224@126.com, CAST504@yeah.net

Abstract ─ The coupling characteristics of the electromagnetic wave penetrating the metallic enclosure with a rectangular aperture are studied using the hybrid approach which applies the mode-matching technique and the mixed potential integral equation based on the method of moments. The aperture thickness, the polarization direction of incident wave, and high-order modes are all considered in the simulation. The calculated electric field at the centre of the enclosure is compared with data obtained by measurement and other numerical techniques to validate the accuracy and the efficiency of the proposed approach. The electric field distributions inside the metallic enclosure are also presented. Furthermore, this approach is extended to account for the effects of narrow aperture thicknesses and polarization directions. The results demonstrate that the electric field is enhanced around the aperture at the resonant frequency and the coupling electric field amplitude at the center point of the enclosure is also higher than that in the ambient area. It is also noted that the variation of the narrow aperture thicknesses and the different polarization directions act on the coupling characteristics significantly.

Index Terms ─ Electric field distribution, electromagnetic coupling, mixed potential integral equation, mode matching, resonance.

I. INTRODUCTION

Electromagnetic shielding by the aid of metallic enclosures is frequently used to reduce emissions from electromagnetic interferences (EMI). At the same time, apertures perforated in the enclosure will compromise its shielding effectiveness. In order to take some measures to limit the influence of the interference energy, it is extremely important to analyze the coupling characteristics of the electromagnetic wave penetrating the metallic enclosures with apertures.

The electromagnetic coupling characteristics can be analyzed using numerical or analytical methods. Numerical methods, such as the finite difference time domain (FDTD) method [1-7], the method of moments (MoM) [8-11], the finite element method (FEM) [12], and the hybrid methods [13-14], can model enclosures with sufficient detail but often requires large computing time and memory, and the analytical approaches based on various simplifying assumptions [15-16] are also subject to many severe limitations even though providing a much faster means.

This paper presents a rigorous full-wave solution which combines the mode-matching technique and the mixed potential integral equation based on MOM to study the coupling characteristics of electromagnetic wave penetrating a metallic enclosure with a rectangular aperture. Some influencing factors, such as the aperture thickness, the polarization direction of the incident wave and high-order modes, are considered in the numerical simulation. Finally, the simulation results are compared with data obtained by measurement and other numerical techniques thus showing the accuracy and the efficiency of the proposed approach.

Submitted On: May 23, 2011
Accepted On: August 24, 2011

II. MATHEMATICAL FORMULATION

A metallic enclosure with dimensions $a \times b \times h$ (inner face) illuminated by the electromagnetic wave is shown in Figure 1, having a rectangular aperture with dimensions $w \times l$ in the front wall. The walls whose thicknesses are t are assumed to be perfectly conducting.

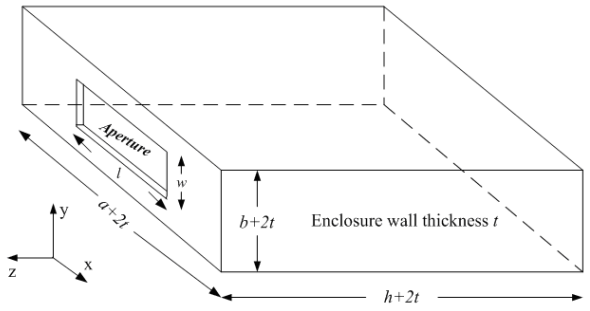

Fig. 1. Geometry of the rectangular enclosure with aperture.

As shown in Figure 2, the entire equivalent model of EMI coupling into a rectangular enclosure through a non-zero thickness aperture can be separated into two sub-problems by employing Schelkunoff's field equivalent principle: the interior problem and the exterior problem. The interior problem is composed of region I and region II which can be regarded as the rectangular waveguides, while the exterior problem is considered as a half free space (region III) with an equivalent magnetic current and an incident electromagnetic wave. It should be noted that the plane z=t where the aperture is perforated is regarded as an infinite conductive plane [17].

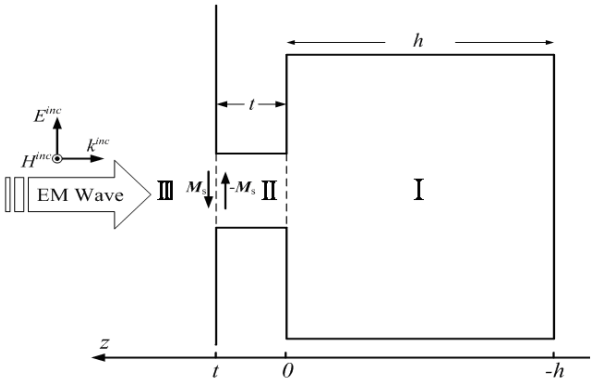

Fig. 2. Equivalent model for aperture replaced by magnetic current.

A. Interior problem

From Maxwell's equations, the tangential electric field and the tangential magnetic field in the waveguides can be represented by

$$\boldsymbol{E}_t = -\frac{j\omega\mu}{k_c^2}\nabla_t H_z \times \boldsymbol{z} + \frac{1}{k_c^2}\nabla_t \frac{\partial E_z}{\partial z} \quad , \tag{1}$$

$$\boldsymbol{H}_t = \frac{j\omega\varepsilon}{k_c^2}\nabla_t E_z \times \boldsymbol{z} + \frac{1}{k_c^2}\nabla_t \frac{\partial H_z}{\partial z} \quad . \tag{2}$$

In order to solve Maxwell's equations conveniently, the electric and the magnetic vector potentials are introduced whose z-direction components are A_{ez} and A_{hz}, respectively. Then z-direction components of the electric field and the magnetic field are given by

$$E_z = \frac{k_c^2}{j\omega\varepsilon} A_{ez} \quad , \tag{3}$$

$$H_z = \frac{k_c^2}{j\omega\mu} A_{hz} \quad . \tag{4}$$

Region I and Region II can be regarded as the rectangular waveguides, the aperture waveguide-to-rectangular enclosure junction can be modeled by the mode-matching technique. And then substituting (3) and (4) into (1) and (2), the tangential electromagnetic fields in Region i (i=I,II) can be expressed as follows [18]:

$$\boldsymbol{E}_t^i = -\nabla_t A_{hz}^i \times \boldsymbol{z} + \frac{1}{j\omega\varepsilon}\nabla_t \frac{\partial A_{ez}^i}{\partial z} \tag{5}$$

$$\boldsymbol{H}_t^i = \nabla_t A_{ez}^i \times \boldsymbol{z} + \frac{1}{j\omega\mu}\nabla_t \frac{\partial A_{hz}^i}{\partial z} \tag{6}$$

$$A_{hz}^i(x,y,z) = \sum_{q=1}^{N} Q_{hq}^i T_{hq}^i \left[A_{hq}^{i+} e^{-\Gamma_{hq}^i z} + A_{hq}^{i-} e^{\Gamma_{hq}^i z} \right] \tag{7}$$

$$A_{ez}^i(x,y,z) = \sum_{q=1}^{N} Q_{eq}^i T_{eq}^i \left[A_{eq}^{i+} e^{-\Gamma_{eq}^i z} - A_{eq}^{-} e^{\Gamma_{eq}^i z} \right], \tag{8}$$

where ε is permittivity of free space and μ is magnetic permeability of free space, T_e and T_h is the eigenfunction of the TM (e) and TE (h) modes, respectively. In the same way, A_e and A_h □are the modal amplitude coefficients, □e and □h are the propagation constants, Q_e and Q_h are the normalized factors such that the power carried by each mode is 1 Watt. q is the mode index.

On the assumption that there are N TM modes and N TE modes propagating in the waveguides, the $2N \times 1$ modal amplitude coefficients matrix of the positive and negative z-direction modes in the

waveguide Region i, $\boldsymbol{A}^{i+}$ and $\boldsymbol{A}^{i-}$ can be described as:

$$A^{i+}=\begin{bmatrix}A_e^{i+}\\A_h^{i+}\end{bmatrix}\qquad A^{i-}=\begin{bmatrix}A_e^{i-}\\A_h^{i-}\end{bmatrix}\ . \tag{9}$$

In terms of the tangential electric field and the tangential magnetic field components matching at the boundary between Region I and Region II, respectively, the coupling matrix $\boldsymbol{M}$ whose size is $2N\times 2N$ is obtained [19]. Therefore, the relationship between the modal amplitude coefficients in Region I and II can be expressed as:

$$A^{I+}+A^{I-}=M\left(A^{II+}+A^{II-}\right)\ , \tag{10}$$

$$M^T\left(A^{I+}-A^{I-}\right)=A^{II+}-A^{II-}\ . \tag{11}$$

On account of the region I is considered as an end-shorted waveguide, what can be obtained is written as:

$$A^{I+}=-L^I A^{I-} \tag{12}$$

where $L^I=diag\left\{e^{-2\Gamma_j^I h}\right\},\ j=e,h$.

Substituting (12) into (10) and (11) gives a matrix equation describing the relationship of the modal amplitude coefficients in Region II:

$$A^{II+}=\rho A^{II-} \tag{13}$$

where $\rho=(U+P)^{-1}(U-P)$

$$P=M^T\left(L^I+U\right)\left(U-L^I\right)^{-1}M\ .$$

U is the $2N\times 2N$ unit matrix.

Substituting (12) and (13) into (10) and (11) gives a matrix equation:

$$A^{I-}=\left(U-L^I\right)^{-1}M\left(\rho+U\right)A^{II-}\ . \tag{14}$$

B. Exterior problem

According to the equivalence principle, the aperture on the plane z=t can be replaced by the equivalent surface magnetic current $\mathbf{M}_s$ as shown in Figure 2, given by

$$\boldsymbol{M}_s=-\boldsymbol{n}\times\boldsymbol{E}_t^{II}(t)\ , \tag{15}$$

with $\boldsymbol{n}$ being the normal unit vector pointing outwards.

By means of image theory, the equivalent magnetic current $2\mathbf{M}_s$ substitutes as the equivalent source for the half-space. Mathematically, the magnetic field $\mathbf{H}^{Ms}$ due to $2\mathbf{M}_s$ in Region III can be written as follows [20]:

$$\boldsymbol{H}^{M_S}=-j\omega\boldsymbol{F}(\boldsymbol{r})-\nabla\phi_m(\boldsymbol{r})\ . \tag{16}$$

To simplify the notation, the inner product can be defined:

$$\langle A,B\rangle=\iint_{sa}A\cdot B dS\ , \tag{17}$$

where the integration extends over the aperture on the plane z=t for the 2D case. Then, the electric vector potential **F** and the magnetic scalar potential ϕ_m at a field point **r** are obtained [21]:

$$\boldsymbol{F}(\boldsymbol{r})=2\varepsilon\left\langle\boldsymbol{M}_s(\boldsymbol{r}'),\bar{\bar{\boldsymbol{G}}}_{free}^{F}(\boldsymbol{r}\,|\,\boldsymbol{r}')\right\rangle\ , \tag{18}$$

$$\phi_m(\boldsymbol{r})=\frac{2j}{\omega\mu}\left\langle\nabla_t'\cdot\boldsymbol{M}_s(\boldsymbol{r}'),G_{free}^{\phi_m}(\boldsymbol{r}\,|\,\boldsymbol{r}')\right\rangle\ . \tag{19}$$

$\bar{\bar{\boldsymbol{G}}}_{free}^{F}$ and $G_{free}^{\phi_m}$ are the dyadic and the scalar Green's function for the half free space respectively.

C. Final matrix equation

According to the continuity of the tangential magnetic field through the aperture on the plane z=t, the magnetic formulation can be accomplished by enforcing:

$$\boldsymbol{H}_t^{M_S}+2\boldsymbol{H}_t^{inc}=\boldsymbol{H}_t^{II}(t)\ . \tag{20}$$

The equation (20) can be solved by MoM, and then the equivalent magnetic current $\mathbf{M}_s$ is expanded by a set of vector basis functions $\mathbf{W}_n$ with unknown coefficients K_n as:

$$\boldsymbol{M}_s=\sum_{n=1}^{2N}K_n\cdot\boldsymbol{W}_n\ . \tag{21}$$

Moreover, the Galerkin procedure is applied. Setting the weighting function **W** ($2N\times 1$) equal to the basis function as:

$$\boldsymbol{W}=\begin{bmatrix}\boldsymbol{W}_e\\\boldsymbol{W}_h\end{bmatrix}=\begin{bmatrix}\dfrac{\Gamma_e^{II}}{j\omega\varepsilon}Q_e^{II}\left(\nabla_t T_e^{II}\right)\times\boldsymbol{z}\\-Q_h^{II}\left(\nabla_t T_h^{II}\right)\end{bmatrix}\ . \tag{22}$$

In terms of the orthogonality of expansion functions, the mixed potential integral equation (20) can be shown as the following matrix equation:

$$TK+I^{inc}=Z\ , \tag{23}$$

where

$$\begin{aligned}TK&=-j\omega\langle\boldsymbol{W},\boldsymbol{F}\rangle-\langle\boldsymbol{W},\nabla\phi_m\rangle\\&=-j\omega\langle\boldsymbol{W},\boldsymbol{F}\rangle+\langle\nabla_t\boldsymbol{W},\phi_m\rangle\\K&=L^{II}A^{II+}+\left(L^{II}\right)^{-1}A^{II-}\\I^{inc}&=\left\langle\boldsymbol{W},2\boldsymbol{H}_t^{inc}\right\rangle\end{aligned}$$

$$Z = \left\langle \boldsymbol{W}, \boldsymbol{H}_t^{II} \right\rangle = L^{II} A^{II+} - \left(L^{II}\right)^{-1} A^{II-}$$

$$L^{II} = diag\left\{ e^{-\Gamma_j^{II} t} \right\} \qquad j = e, h$$

It is worth noting that the matrix $\mathbf{I}^{inc}$ relates to the polarization direction of the incident wave. Furthermore, putting (20) together with (13), the unknown modal coefficients $\mathbf{A}^{II-}$ are readily obtained if the incident plane wave has been given:

$$A^{II-} = \left[\left(L^{II} \rho - (L^{II})^{-1} \right) - T \left(L^{II} \rho + (L^{II})^{-1} \right) \right]^{-1} I^{inc} \cdot \tag{24}$$

Finally, introducing (24) into the matrix equations (12) and (14), all the modes propagating in the enclosure can be calculated. The electromagnetic fields at any point in the enclosure with non-zero thickness aperture can be calculated consequently.

III. MEASUREMENT SETUPS

In the measurement setup of Figure 3, a semi anechoic chamber of 11.37m× 4.6m× 3.0m is used, where the walls are covered with absorbing cones except for the conducting floor. The log periodic antenna—TX in Figure 3— is connected via a RF amplifier to an Agilent E8157D signal generator as the source of the field. The enclosure indicated by EUT is constructed of five pieces of aluminum and one plate of aluminum for the face containing the aperture. Measurements are made by placing the R&S HZ-15 probe in the centre of the enclosure and the output is shown on an Agilent E4440A spectrum analyzer. The effect of the ground plane and the attenuation of cables are accounted for by a suitable calibration procedure.

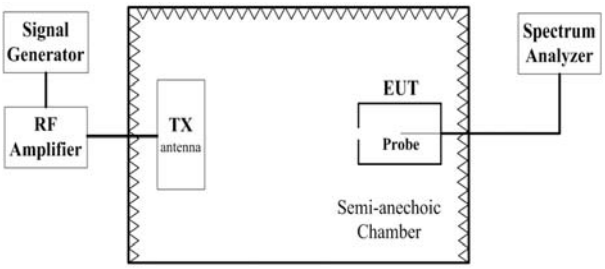

Fig. 3. Measurement setups in a semi-anechoic chamber.

IV. NUMERICAL EXAMPLES

For the analysis of electromagnetic coupling characteristics, a typical rectangular enclosure with inner dimensions 30cm×12cm×30cm is considered, having a narrow aperture of size 10cm×0.5cm with thickness t=1.5mm located at the center of the front wall. In addition, the incident wave is propagating along negative z-direction with an intensity of 377 V/m; and its polarization direction is parallel to the short edge of the aperture (y-axis), which goes by the name of vertical polarization.

A. Validation of proposed method

In this paper, the observation point is located at the center of the enclosure. For the whole model, there are 50 TM modes and 50 TE modes introduced to obtain high accuracy results.

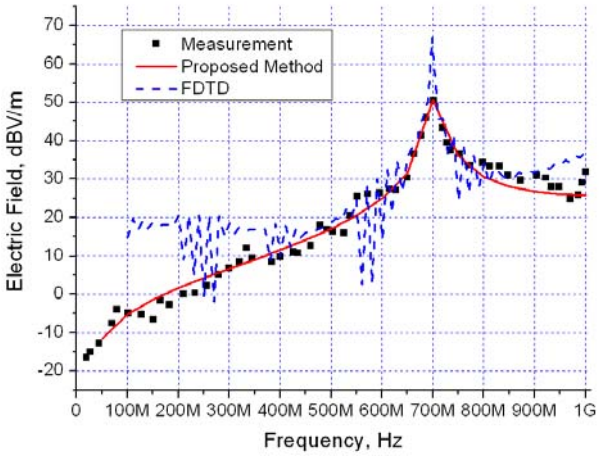

Fig. 4. Simulated and measured electric field amplitude varies with frequency at center of the enclosure.

From Figure 4, it can be seen that the results obtained by the proposed approach are in good agreement with the measurement data. The first resonant frequency 700MHz is predicted accurately at which TE_{101} mode is excited in this metallic enclosure and the coupling energy reaches its maximum over the frequency from 100MHz up to 1.0GHz. This can be very useful in optimizing the shielding devices to get some resonant frequencies filtered and minimize the EMI. In addition, the results are compared with the data obtained by FDTD. It should be mentioned that it only takes about 12 minutes and 200MByte

memory for the proposed approach to calculate the coupling electric field for 20 frequencies, while it takes 55 minutes and 350MByte memory for FDTD on the same business PC. Furthermore, taking this structure all the same, it requires more than 1 hour and 1.2GByte memory for FEM to obtain the results at 20 frequencies in [22]. This illustrates the efficiency of the proposed approach.

B. Electric field distributions inside enclosure

The metallic enclosure itself possesses a set of characteristic resonance behavior excited by external interference signals. What is more, the presence of apertures cut in the enclosure complicates resonant characteristics of the enclosure. So the electric field distributions inside the enclosure with an aperture at the resonant frequency are expected. It is useful for designers laying out the electronic components to avoid the damage caused by the external interference signals. In the following simulation figures, the incident-wave frequency is chosen to be the first resonant frequency 700 MHz, and the coupling electric field distributions inside the aforementioned enclosure are presented.

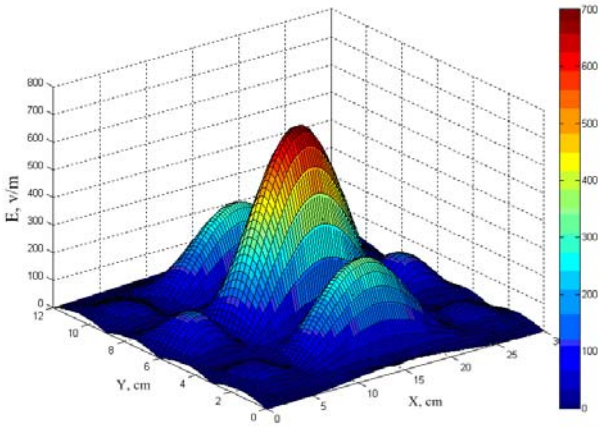

Fig. 5. Electric field distributions on the XOY plane of the enclosure at z=0cm (700MHz).

Figures 5 and 6 depict the coupling electric field distributions on the XOY plane of the enclosure at z=0cm and z=–15cm respectively. In Figure 5, it can be seen that the coupled electric field amplitude adjacent to the aperture is much higher than the incident, namely, the electric field amplitude is enhanced around the aperture. This is owing to additional enclosure-aperture interactions and the influence of high-order modes.

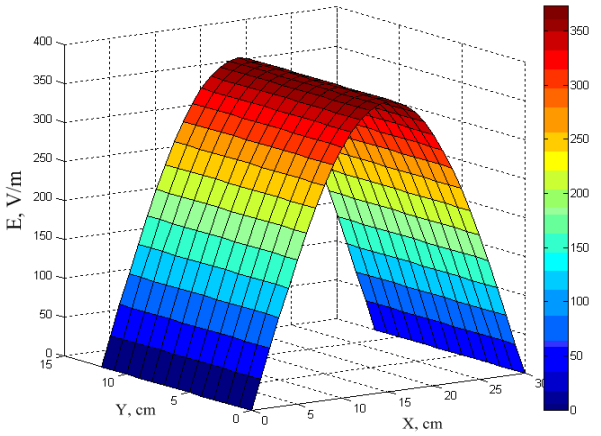

Fig. 6. Electric field distributions on the XOY plane of the enclosure at z=-15cm (700MHz).

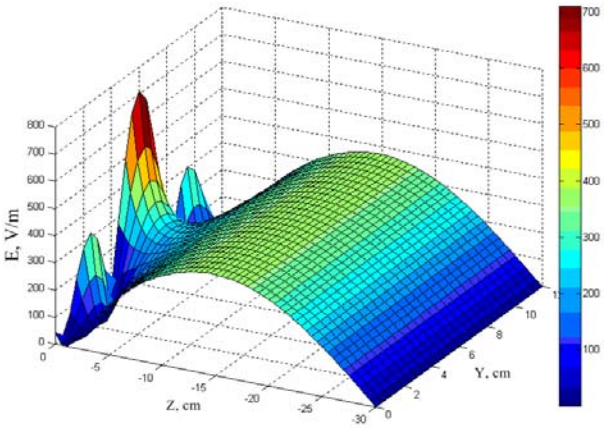

Fig. 7. Electric field distributions on the YOZ planes in the middle of the enclosure (700MHz).

The distributions of the coupled electric field on the YOZ and XOZ planes in the middle of the enclosure are shown in Figs. 7 and 8, respectively. The fact that the coupling electric field amplitude is the highest in the small area adjacent to the aperture validates the electric field amplitude being enhanced around the aperture. Furthermore, from Fig. 6 to Fig. 8, it is obvious that the coupling electric field amplitude at the center point of the enclosure is also higher than that in the ambient area.

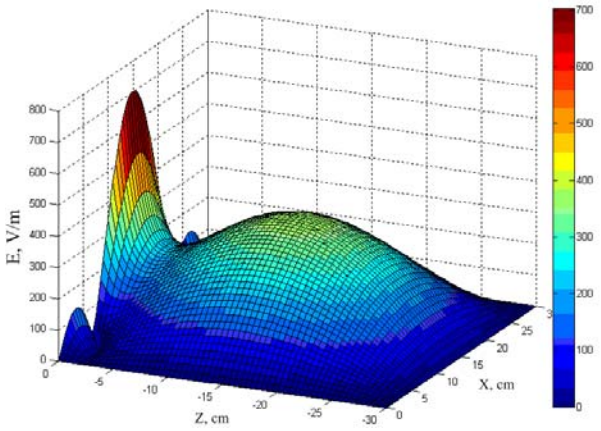

Fig. 8. Electric field distributions on the XOZ planes in the middle of the enclosure (700MHz).

C. Effect of narrow aperture thicknesses

In order to study the effect of various aperture thicknesses on coupling characteristics of electromagnetic wave penetrating a metallic enclosure through a narrow aperture, the coupling electric field at the center of the enclosure varying with the thicknesses of the aperture is considered. The narrow aperture thicknesses considered cover commonly used values: 0.5, 1.5, 3, 5, 8, and 10mm. Simulation results are displayed as a function of aperture thickness in Fig. 9. It is found that with the narrow aperture thickness increasing, the amplitude of the coupling electric field is decreasing, i.e., electromagnetic shielding of the enclosure is improved.

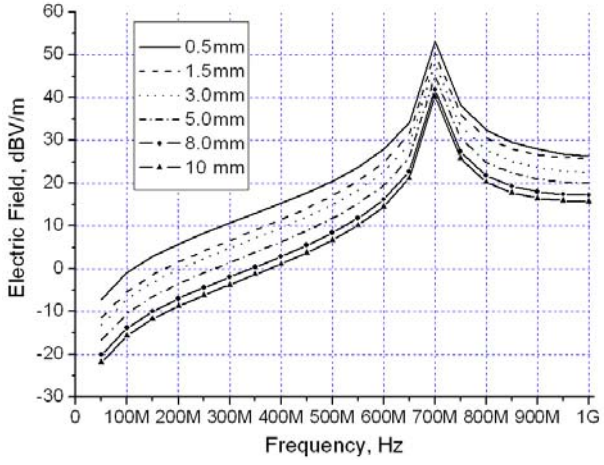

Fig. 9. Comparison of Electric fields at center of the rectangular enclosure with various narrow aperture thicknesses.

D. Effect of different polarizations

In this part, the effect of the polarization directions of the incident wave to the coupling characteristics is investigated. Compared with the vertical polarization, the horizontally polarized incident wave whose electric field polarization direction is parallel to the long edge of the aperture (x-axis) is introduced. The coupling electric field at the center of the enclosure with regard to different polarizations is shown in Fig. 10. It should be noted that the coupling electric field amplitude of the vertically polarized incident wave is higher than that of the horizontally polarized one at the center of the rectangular enclosure.

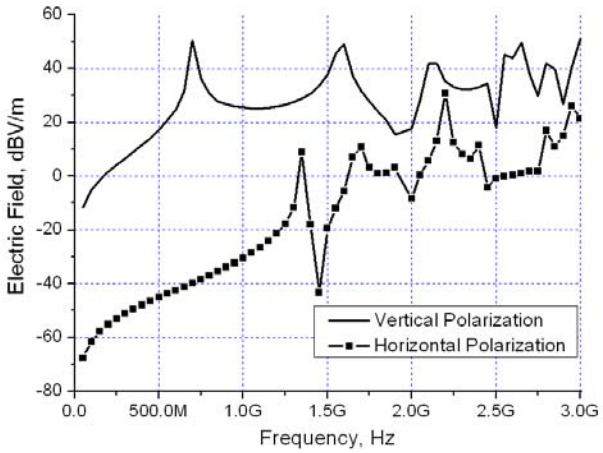

Fig. 10. Electric field at center of the rectangular enclosure with different polarizations.

V. CONCLUSIONS

The coupling characteristics of the electromagnetic wave penetrating the metallic enclosures with non-zero thickness apertures are hot issues. By matching the continuity condition of tangential electromagnetic field components across the aperture surface and the boundary between the aperture waveguide and the rectangular enclosure, the unknown modal amplitude coefficients are calculated and the electromagnetic fields inside the rectangular enclosure are determined in this paper. Usage of the proposed approach to evaluate the field distributions inside the enclosure should be helpful for laying out the vulnerable semiconductor components to limit the influence of external

electromagnetic radiation. Furthermore, the numerical simulations are directly related to the design of efficient shielding enclosures that are commonly used to protect inside components.

REFERENCES

[1] J. Z. Lei, C. H. Liang, and Y. Zhang, "Study on Shielding Effectiveness of Metallic Cavities with Apertures by Combining Parallel FDTD Method with Windowing Technique," *Progress in Electromagnetics Research*, PIER 74, pp. 85–112, 2007.

[2] J. Chen and A. Zhang, "A Subgridding Scheme Based on the FDTD Method and HIE-FDTD Method," *Applied Computational Electromagnetic Society (ACES) Journal*, vol. 26, no. 1, pp. 1–7, 2011.

[3] X. Li, J.-H. Yu, Q.-Di Wang, and Y.-M. Li, "Extension of the 2-D CP-FDTD Thin Slot Algorithm to 3-D for Shielding Analysis," *Applied Computational Electromagnetic Society (ACES) Journal*, vol. 24, no. 1, pp. 16–20, 2009.

[4] R. I. Macpherson, N. J. Ryan, R. I. Macpherson, and N. J. Ryan, "Reducing Electromagnetic Coupling in Shielded Enclosures using a Genetic Algorithm -- Finite-Difference Time-Domain Solver," *Applied Computational Electromagnetic Society (ACES) Journal*, vol. 18, no. 3, pp. 144–150, 2003.

[5] M. Li, J. Nuebel, J. L. Drewniak, R. E. DuBroff, T. H. Hubing, and T. P. Van Doren, "EMI from Airflow Aperture Arrays in Shielding Enclosures – Experiments, FDTD, and MoM Modeling," *IEEE Trans. Electromagn. Compat.*, vol. 42, no. 3, pp. 265–275, 2000.

[6] W. H. Yu, R. Mittra, and S. Chakravarty, "Stability Characteristics of Absorbing Boundary Conditions in Microwave Circuit Simulations," *IEEE Trans. Antennas Propagat.*, vol. 49, no. 9, pp. 1347–1349, 2001.

[7] N. Kantartzis and T. Tsiboukis, "A Higher-Order Non-Standard FDTD-PML Method for the Advanced Modeling of Complex EMC Problems in Generalized 3-D Curvilinear Coordinates," *IEEE Trans. Electromagn Compat.*, vol. 46, no. 1, pp. 2-11, 2004.

[8] R. Araneo and G. Lovat, "Analysis of the Shielding Effectiveness of Metallic Enclosures Excited by Internal Sources Through an Efficient Method of Moment Approach," *Applied Computational Electromagnetic Society (ACES) Journal*, vol. 25, no. 7, pp. 600–611, 2010.

[9] R. Araneo and G. Lovat, "Fast MoM Analysis of the Shielding Effectiveness of Rectangular Enclosures with Apertures, Metal Plates, and Conducting Objects," *IEEE Trans. Electromagn. Compat.*, vol. 51, no. 2, pp. 274-283, 2009.

[10] R. Araneo and G. Lovat, "An Efficient MoM Formulation for the Evaluation of the Shielding Effectiveness of Rectangular Enclosures with Thin and Thick Apertures," *IEEE Trans. Electromagn. Compat.*, vol. 50, no. 2, pp. 294-304, 2008.

[11] F. Olyslager, E. Laermans, D. De Zutter, S. Criel, R. De Smedt, N. Lietaert, and A. De Clercq, "Numerical and Experimental Study of the Shielding Effectiveness of a Metallic Enclosure," *IEEE Trans Electromagn Compat.*, vol. 41, no. 3, pp. 202-213, 1999.

[12] S. Benhassine, L. Pichon, and W. Tabbara, "An Efficient Finite-Element Time-Domain Method for the Analysis of the Coupling between Wave and Shielded Enclosure," *IEEE Trans. Magn.*, vol. 38, no. 2, pp. 709–712, 2002.

[13] C. Feng and Z. Shen, "A Hybrid FD-MoM Technique for Predicting Shielding Effectiveness of Metallic Enclosures with Apertures," *IEEE Trans. Electromagn. Compat.*, vol. 47, no. 3, pp. 456–462, 2005.

[14] S. Yenikaya and A. Akman, "Hybrid MoM/FEM Modeling of Loaded Enclosure with Aperture in EMC Problems," *Int. J. RF and Microwave CAE.*, vol. 19, pp. 204–210, 2009.

[15] M. P. Robinson, T. M. Benson, C. Christopoulos, J. F. Dawson, M. D. Ganley, A. C. Marvin, S. J. Porter, and D. W. P. Thomas, "Analytical Formulation for the Shielding Effectiveness of Enclosures with Apertures," *IEEE Trans. Electromagn. Compat.*, vol. 40, no. 3, pp. 240–247, 1998.

[16] T. Konefal, J. F. Dawson, A. Marvin, M. P. Robinson, and S. J. Porter, "A Fast Multiple Mode Intermediate Level Circuit Model for

the Prediction of Shielding Effectiveness of a Rectangular Box Containing a Rectangular Aperture," *IEEE Trans. Electromagn. Compat.*, vol. 47, no. 4, pp. 678–691, 2005.

[17] J. R. Mosig, "Scattering by Arbitrarily-Shaped Slots in Thick Conducting Screen: An Approximate Solution," *IEEE Trans. Antennas Propagat.*, vol. 52, no. 8, pp. 2109–2117, 2004.

[18] B. Q. Zhang, *Research on Mode-Matching Method in Microwave Passive Component Design*, Ph.D. Thesis, University of Electronic Science and Technology of China, 2004.

[19] G. Wu, X. G. Zhang, and B. Liu, "A Hybrid Method for Predicting the Shielding Effectiveness of Rectangular Metallic Enclosures with Thickness Apertures," *J. of Electromagn. Waves and Appl.*, vol. 24, no. 8–9, pp. 1157–1169, 2010.

[20] R. F. Harrington, *Time-Harmonic Electromagnetic Fields*, IEEE Press, 2001, 2nd edn.

[21] W. Wallyn , D. D. Zutter, and H. Rogire, "Prediction of the Shielding and Resonant Behavior of Multisection Enclosures Based on Magnetic Current Modeling," *IEEE Trans. Electromagn. Compat.*, vol. 44, no. 1, pp. 130–138, 2002.

[22] S. Celozzi, R. Araneo, and G. Lovat, *Electromagnetic Shielding*, Wiley-IEEE, New Jersey, 2008.

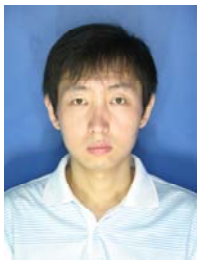

Gang Wu was born in Xi'an, Shaanxi, China, in 1981. He received his M.Sc. degree in Electronic Engineering from Xidian University, Xi'an, China in 2007. From 2008 to now, he is a doctor degree candidate in Xi'an division of China academy of space technology. His study direction is the theory and technology on electromagnetic protection.

Zhi-Qiang Song was born in Ya'an, Sichuang, China, in 1972. He received his M.S. degree in Electrical and Electronics Engineering from Xidian University, in 2005. He is currently working as a senior engineer at Xi'an division of China academy of space technology, Xi'an, China. His research interests are RF and microwave design, microwave measurements.

Xin-Gang Zhang was born in Shijiazhuang, Hebei, China, in 1980. He received his M.S. degree from Chongqing University, in 2007, in Electrical and Electronics Engineering. He is currently working as a doctor degree candidate at Xi'an division of China academy of space technology, Xi'an, China. His research interests are the theory of antenna, numerical studies of electromagnetic fields and waves.

Bo Liu was born in Changsha, Hunan, China, in 1962. He is currently working as a senior researcher at Xi'an division of China academy of space technology, Xi'an, China. His research interests are microwaves, radio wave propagation, and antennas.

Design of a Novel Dual-Beam Scanning Leaky-Wave Antenna

Jian-Chao Liu, Wei Shao, and Bing-Zhong Wang

Institute of Applied Physics
University of Electronic Science and Technology of China, Chengdu, Sichuan, 610054, China
ljc_221@126.com, weishao@uestc.edu.cn, bzwang@uestc.edu.cn

Abstract ─ In this article, a novel dual-beam scanning leaky-wave antenna is proposed and investigated. Antenna parameters, such as return loss, radiation patterns, gain, efficiency and scanning angles, are provided and discussed. Besides its low profile and miniaturized size, the proposed antenna can realize dual-beam scanning and quasi-omnidirectional radiation. Moreover, it provides much design flexibility for real applications. Different simulation software are adopted to verify the accuracy of our design.

Index Terms ─ CRLH TL, dual-beam scanning, LWA, SIW.

I. INTRODUCTION

Over the past decade, novel metamaterial structures, and in particular composite right/left (CRLH) transmission line (TL) metamaterial structures, have led to efficient and more versatile leaky-wave antennas (LWAs). The first papers based on a TL approach of metamaterial dealt specifically with left-handed (LH) TL metamaterials and were published by three different groups [1-3]. This concept matured quickly and led to the first backfire-to-endfire CRLH LWA [4], which exhibits important advantages over conventional LWAs [5]. The conventional LWAs require complex narrow-band feeding circuits due to the harmonic operation, and cannot radiate a true broadside radiation pattern with scanning. The CRLH LWAs offer full scanning capability in its fundamental harmonic with a simple feeding TL. Recently, a CRLH structure based on substrate integrated waveguide (SIW) has been proposed and shown its advantages [6-9].

The developed antenna in this article not only retains the advantages mentioned above but demonstrates a new feature of dual-beam scanning. In this design, the spatial scanning range $(-60^\circ, +60^\circ)$ can be achieved when f varies in the range from 8.8 to 10 GHz in LH region, and $(-60^\circ, +55^\circ)$ can be achieved when f varies from 10 to 12.8GHz in RH region. Thus this antenna realizes the same function as the conventional leaky-wave antennas, but it uses only part of the frequency spectrum. This performance is confirmed by comparing the radiation patterns at different frequencies in the following section.

II. ANTENNA DESIGN

In this design, the prototype is built on the normally used substrate of Rogers 5880 with a relative permittivity of 2.2, a loss tangent of 0.001 and a thickness of 0.508 mm.

A. Unit cell structure and dispersion relation

The balanced CRLH SIW unit cell and its dispersion diagram are shown in Fig. 1(a) and (b), respectively. The dispersion relation for the unit cell is investigated by using Ansoft's HFSS software package and calculated based on the S-parameters from driven mode simulation [10-11]. From Fig. 1 (b), the dispersion curve traverses four distinct regions as frequency increases, where the radiation regions are characterized by a phase velocity larger than the speed of the light. By applying the inter-digital structure and moving the LH region far below the waveguide cut-off frequency, miniaturization can be obtained. It has been shown that the group velocity is nonzero when f=10 GHz despite infinite phase velocity, which allows leaky-wave broadside radiation.

Submitted On: June 21, 2011
Accepted On: September 16, 2011

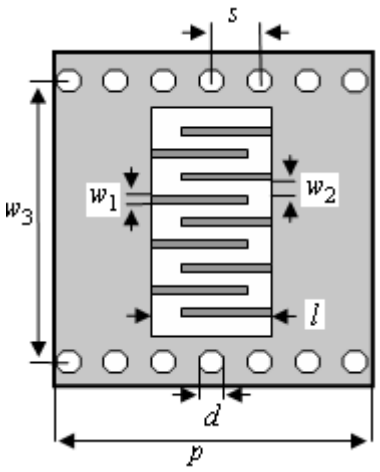

(a)

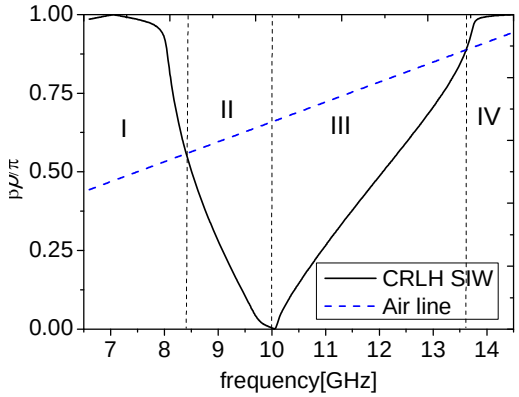

(b)

Fig. 1. (a) CRLH unit cell. The parameters are: w_1=0.33mm, w_2=0.45mm, w_3=9.2mm, p=8.2mm, l=3.3mm, d=0.8mm, s=1.45mm, and n=9 (number of fingers). (b) Dispersion diagram of the unit cell (I. LH guided wave region, II. LH radiation region, III. RH radiation region and IV. RH guided wave region).

B. The prototype of CRLH SIW antenna

The prototype of CRLH SIW antenna shown in Fig. 2(a) has two paths and each path has eight identical elementary cells. As indicated in Fig. 2(b), the radiation angle of the main beam is straightforward determined by

$$\theta(\omega) = \text{acos}(\beta(\omega)/k_0), \quad (1)$$

where β is the phase constant and k_0 is the wave number in free space. The two paths in the opposite direction result in two opposite main beams for a special frequency ($\beta(\omega) < 0$), as shown in Fig. 2 (b). A similar phenomenon will appear when $\beta(\omega) > 0$. It is also shown that a full space scanning can be achieved twice if $\beta(\omega)$ varies in the range of $(-k_0, +k_0)$.

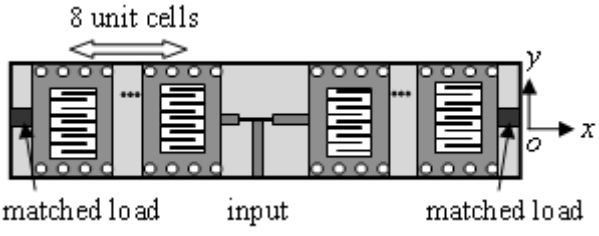

(a)

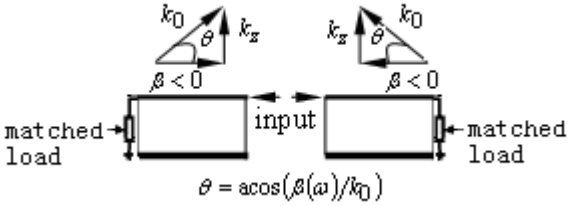

(b)

Fig. 2. Configuration of CRLH SIW leaky-wave antenna, (a) overall antenna prototype, (b) working principle of the antenna.

The broadside radiation cannot be achieved if two paths are absolutely symmetrical about the feeding strip. Figure 3 plots the electric field distribution on metal surfaces when f=10 GHz. Since the amplitudes of electric fields along the two paths are identical and the phase difference between them is 180 degrees, their radiation cancels out each other in the broadside direction. To get the broadside radiation, the length of one path in Fig. 4 is extended to eliminate the phase difference, and a T-junction used as a power divider is adjusted to obtain impedance matching, where Z_0 is the input impedance of the antenna, λ_g is the medium wavelength when f=10 GHz, and $\Delta L_T = \lambda_g/2$.

III. RESULTS AND DISCUSSION

Figure 5 shows the simulated S-parameters of this antenna with using Ansoft's HFSS and CST Microwave Studio. The data from the two softwares are in a good agreement from Fig. 5. A satisfactory return loss below -10 dB in the band of interest is achieved. The curves of S_{21} and S_{31}

also show that the radiation in the LH region is more effective than that in the RH region.

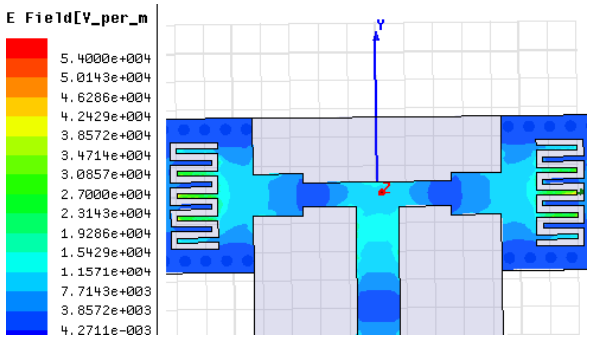

Fig. 3. Electric field distribution on the metal surface at 10 GHz.

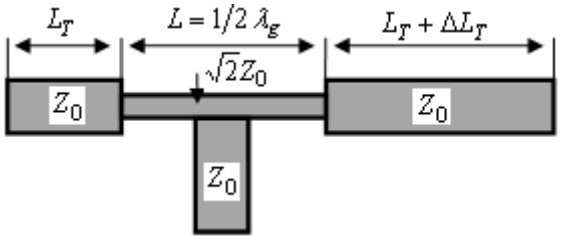

Fig. 4. T-junction feeding port.

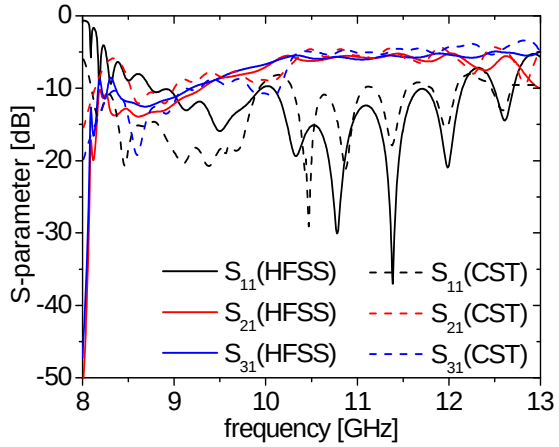

Fig. 5. Simulated S-parameters for the antenna.

Here the performance of dual-beam scanning is presented by comparing radiation patterns at different frequencies in Fig. (6). Figure 6 (a) displays the broadside radiation pattern at 10GHz. The E-plane (*xoz* plane) radiation patterns at 8.8 and 9.1 GHz in the LH region are given in Fig. 6(b). It is found that at 8.8 GHz the two beam angles θ are about -60° and $+60^\circ$, respectively.

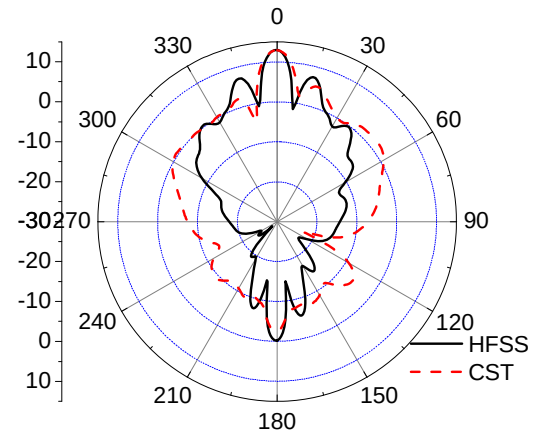

(a)

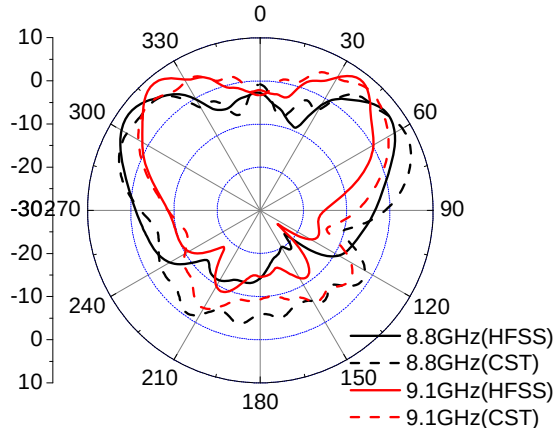

(b)

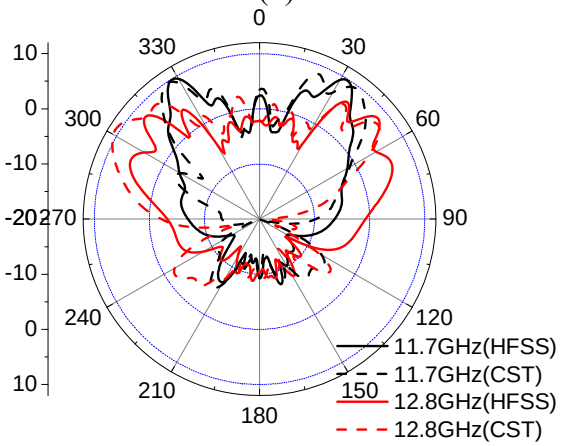

(c)

Fig. 6. Simulated radiation patterns at different frequencies. (a) 10 GHz at the transition point, (b) 8.8 and 9.1 GHz in LH region, (c) 11.7 and 12.8 GHz in RH region.

Figure 6(c) presents the E-plane radiation patterns at 11.7 and 12.8 GHz in the RH region.

The main beams at 12.8 GHz are about -60° and $+55^\circ$, respectively. Numerical results show a reasonably good agreement between the two commercial softwares. Based on the radiation principle shown in Fig. 2 (b) for the studied frequency region, the proposed antenna can realize pattern scanning towards two opposite directions synchronously.

Figure 7 shows the antenna gain and radiation efficiency responses from the simulation (Ansoft HFSS). The antenna has an average radiation efficiency of 74%.

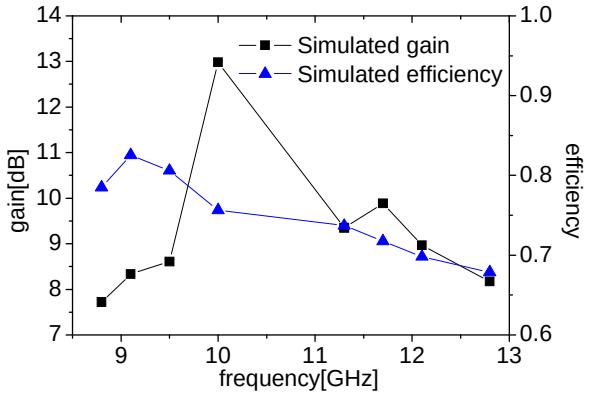

Fig. 7. Simulated gain and radiation efficiency of the antenna.

IV. CONCLUSION

A novel dual-beam scanning leaky-wave antenna is presented. Its dispersion relation and radiation mechanism are discussed, and dual-beam scanning performance is confirmed by simulation results. This antenna also exhibits advantages in low fabrication complexity, low profile, and easy integration with other planar circuits.

ACKNOWLEDGMENT

This work is supported in part by the National Natural Science Foundation of China (60901023), the DPR Foundation (9140A03011210DZ02) and the Fundamental Research Funds for the Central Universities (ZYGX2010J043).

REFERENCES

[1] C. Caloz and T. Itoh, "Application of the Transmission Line Theory of Left-Handed (LH) Materials to the Realization of a Microstrip LH Line," in *Proc. IEEE Antennas Propagat. Soc. int. Symp. Dig.*, vol. 2, pp. 412-415, Jun. 2002.

[2] A. K. Iyer and G. V. Eleftheriades, "Negative Refractive Index Metamaterials Supporting 2-D Waves," in *Proc. IEEE MTT-S int. Symp. Dig.*, vol. 2, pp. 1067-1070, Jun. 2002.

[3] A. A. Oliner, "A Planar Negative-Refractive-Index Medium without Resonant Elements," in *Proc. IEEE MTT-S Int. Symp. Dig.*, vol. 1, pp. 191-194, Jun. 2003.

[4] L. Lei, C. Caloz, and T. Itoh, "Dominant Mode Leaky-Wave Antenna with Backfire-To-Endfire Scanning Capability," *Electron. Lett.*, vol. 38, no. 23, pp. 1414-1416, Nov. 2002.

[5] A. Oliner, "Chapter Leaky-Wave Antennas," in *Antenna Engineering Handbook*, R. C. Johnson, 3rd. Ed., New York: McGraw-Hill, 1993.

[6] H. Zhao, T. J. Cui, X. Q. Lin, and H. F. Ma, "The Study of Composite Right/Left Handed Structure in Substrate Integrated Waveguide," in *Proc. Int. Symp. Bisphotonics, Nanophotonics Metamaterials*, pp. 547-549, Oct. 2006.

[7] T. Cui, X. Lin, Q. Chen, H. Ma, and X. Yang, "Experiments on Evanescent-Wave Amplification and Transmission using Metamaterial Structures," *Phys. Rev. B*, vol. 73, pp. 2451191-2451198, Jun. 2006.

[8] Y. Dong and T. Itoh, "Composite Right/Left-Handed Substrate Integrated Waveguide and Half-Mode Substrate Integrated Waveguide," in *IEEE MTT-S Int. Microw, Symp. Dig.*, pp. 49-52. Boston, 2009.

[9] K. Okubo, M. Kishihara, A. Yamamoto, J. Yamakita, and I. Ohta, "New Composite Right/Left-Handed Transmission Line using Substrate Integrated Waveguide and Metal-Patches," in *IEEE MTT-S Int. Microw. Symp. Dig.*, pp. 41-44, Boston, 2009.

[10] D. M. Pozar, "Microwave Filters," in *Microwave Engineering*, 3rd. Ed., Hoboken, NJ: Wiley, 2005.

[11] "*Left-Handed Metamaterial Design Guide*," Ansoft Corporation, 2007.

Jian Chao Liu received the B.E. degree in Information Engineering form Henan Institute of Science and Technology, Xinxiang, China, in 2009.

From September 2009 to now, he is pursuing the M. Sc. degree in Institute of Applied Physics in University of Electronic Science and Technology of China (UESTC), Chengdu, China. His current research interests include metamaterials and their applications.

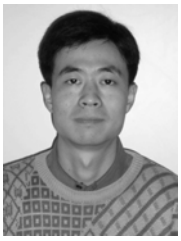

Wei Shao received the M. Sc. and Ph. D. degrees in Radio Physics from the UESTC, Chengdu, China, in 2004 and 2006, respectively.

He joined the UESTC and is now an associate professor there. He has been a Visiting Scholar in the Electromagnetic Communication Laboratory, Pennsylvania State University in 2010. His research interests include the computational electromagnetics and antenna technique.

Bing-Zhong Wang received the Ph.D. degree in Electrical Engineering from UESTC, Chengdu, China, in 1988.

He joined the UESTC in 1984 and is currently a Professor there. He has been a Visiting Scholar at the University of Wisconsin-Milwaukee, a Research Fellow at the City University of Hong Kong, and a Visiting Professor in the Electromagnetic Communication Laboratory, Pennsylvania State University. His current research interests are in the areas of computational electromagnetics, antenna theory, and computer-aided design for microwave circuits.

Compact Bandpass Filters with Bandwidth Control using Defected Ground Structure (DGS)

Sajjad Ur Rehman, Abdel Fattah A. Sheta, and Majeed A. S. Alkanhal

Department of Electrical Engineering
King Saud University, P.O.Box 800, Riyadh 11421, Kingdom of Saudi Arabia
engr.sajjadrehman@gmail.com, asheta@ksu.edu.sa, majeed@ksu.edu.sa

Abstract ─This paper presents new compact microstrip bandpass filters with bandwidth control by employing DGS resonators. The proposed bandpass filters consists of two coupled DGS resonators with a microstrip excitation. The bandwidth can be controlled by choosing the coupling structure between the two DGS resonators. The wider bandwidth can be achieved by adding a strip conductor between the two DGS resonators. However, the narrow bandwidth can be obtained by etching a slot in the strip conductor placed between the DGS resonators. The widths of the strip conductor and the etched slot control the filter bandwidth. Fractional bandwidth (*FBW*) from about 2.5% or less to more than 22% can be achieved by this design approach. The concept has been validated through the design and implementation of two filters with *FBW* of 6% and 12.9%. Measurements agree well with theoretical results.

Index Terms ─ Bandpass filter, DGS filter, microstrip filters.

I. INTRODUCTION

Recent advances in wireless communications demand high performance and compact RF subsystems. Almost all wireless communication systems require compact microwave filters, which can suppress unwanted out-of-band signals. The inherent advantages of defected ground structures (DGS) make it one of the most important techniques to meet compact high performance microwave filters. DGS is an etched periodic or non-periodic cascaded configuration defect in the ground of microstrip and coplanar lines. DGS disturbs the shield current distribution in the ground plane. This disturbance will change the characteristics of a transmission line such as line capacitance and inductance [1]. DGS have interesting properties such as size miniaturization, suppression of surface waves and arbitrary stop bands [2-4]. Since DGS cells have inherently resonant properties, many of them have been used in filtering circuits to improve the stop and pass band characteristics [5].

Many filters have been investigated which controls the center frequency and bandwidth [5-11]. DGS based patterns that can be considered the dual of the open-loop microstrip resonators is proposed in [5] and used to design coupled resonator filters with different external coupling arrangements. The same concept has also been used to design a multilayer coupled resonator DGS filter [6]. This approach introduces various coupling mechanisms to achieve a wider class of filtering functions. Dual-band bandpass filters featuring compact size and flexible frequency choice are demonstrated in [7] using resonators based on slotted ground structures. Two resonators based on slotted ground structures form the basis of the filter design. The resonators allow the back-to-back and face-to-face embedding configuration, hence, greatly reduces the physical size of the filters. The work reported in [8] proposed bandpass filter design based on coupled DGS and microstrip resonators. The combination of DGS and microstrip resonators allows use of the top and bottom side of the microwave substrate, therefore the resonators can partially overlap and desired coupling coefficient can be achieved. In [9],

Submitted On: July 13, 2011
Accepted On: August 21, 2011

second and third order bandpass filters have been designed for fractional bandwidth from 7% to 17% through various feeding arrangements. In [10], a study of some planar microwave bandpass filters composed of defected ground resonators using electric and magnetic coupling are proposed. The proposed DGS microstrip resonator presented in [11] has the resonant and anti-resonant characteristic that is very similar to those of a SAW resonator or a FBAR.

In this paper, we propose new compact microstrip bandpass filters based on coupled DGS resonators. A strip conductor placed between the DGS resonator and etched slot in this strip conductor adjust the coupling between the resonators and then the filter bandwidth. The bandwidth of the proposed filter is controlled by changing the slot and strip widths. The proposed DGS resonator is presented in Section II where in the effect of the resonator size on the resonator resonance frequency is discussed. Bandpass filters based on coupled DGS resonators are investigated in Section III followed by concluding remarks in Section IV.

II. DGS RESONATORS

In the past years, various slotted ground resonators were proposed such as open-loop DGS resonators [5, 7], dumbbell [12], spiral [13], H-shaped [14], and cross-H shaped [15]. The proposed DGS resonators shown in Figs. 1(b) and 1(c) are developed from the conventional DGS resonator shown in Fig. 1(a) [7]. The self resonance frequency (f_0) of the resonator depends on its physical dimensions.

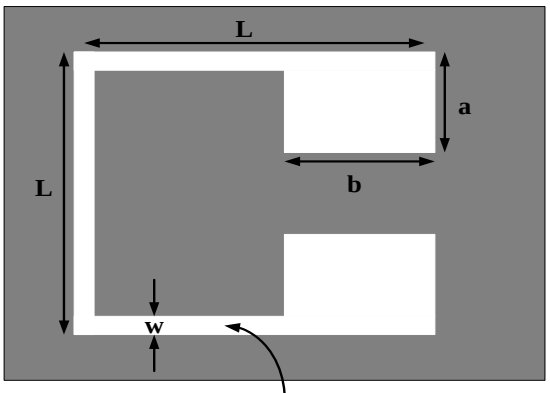

(a)

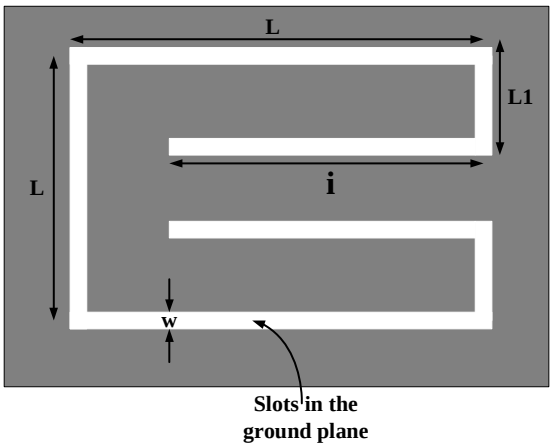

(b)

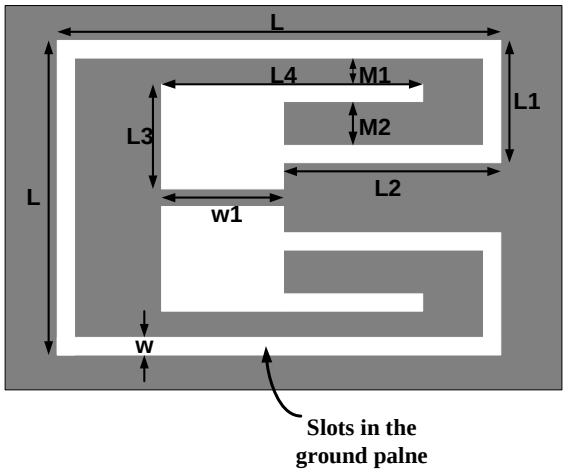

(c)

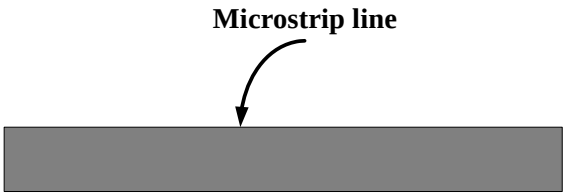

(d)

Fig. 1. Schematic layout of various DGS resonators: (a) backside of the DGS resonator proposed in [7], (b) backside of our proposed DGS resonator, Type A, (c) backside of our proposed DGS resonator, Type B, (d) front side of the DGS resonators.

All resonators are excited by 50 Ω microstrip line shown in Fig. 1(d). Duroid material with 2.2 dielectric constant and 0.78mm thickness is used. The length *L* of the square cell is 10mm and *W* is 0.5mm for all three resonators. *a* and *b* in Fig. 1(a) are 4mm and 5mm, respectively. *L1* is 4mm and *i* is 8mm for resonator in Fig. 1(b). Whereas, *L1* is

4mm, *L2* is 5.5mm, *L3* is 3.5mm, *L4* is 6mm, *M1* is 0.9 mm, *M2* is 1.6mm, and *W1* is 2.5mm for the proposed resonator shown in Fig. 1(c). For the same square size $L \times L$ the structure shown in Fig. 1(c) is the most compact structure (i.e the lowest resonance frequency) compared to those shown in Figs. 1(a) and 1(b). Based on the dimensions mentioned above, the simulated S_{21} of the three configurations is shown in Fig. 2. It can be shown that the resonance frequency is reduced from 2.92 GHz for the structure in Fig. 1(a) to 2.37 GHz and 1.8GHz for the structures given in Figs. 1(b) and 1(c), respectively. For this reason, the filter analyzed and designed in this paper is based on the structure given in Fig. 1(c).

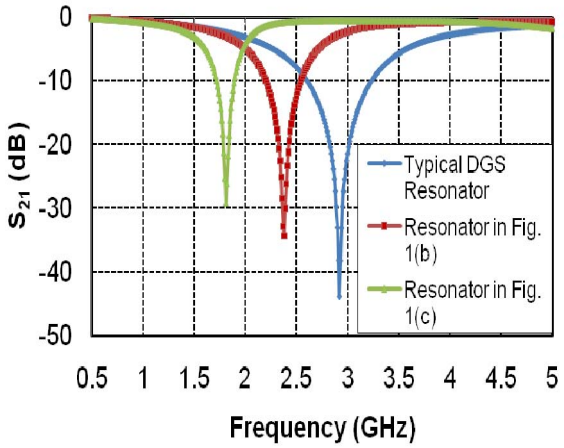

Fig. 2. Simulated S_{21} of the three resonators shown in Figs 1(a), 1(b), and 1(c).

The resonant frequency f_0 of the proposed resonator in Fig. 1(c) is determined by the width and the length *L* of the DGS cell. Scaling up and down the physical size of the DGS cell can control the resonance frequency f_0. Denoting *L'* as the new lengths compared to the dimensions given above. *L'* represents all the lengths including *L, L1, L2, and L4.* The resonator resonance frequency is inversely proportional to the cell size *L'*. Figure 3 shows the simulation f_0 for different values of *L'*. It is seen that by increasing *L'* by 1mm (*L'*+1), f_0 is reduced to 1.42 GHz. While decreasing the *L'* by 2mm (*L'*-2), f_0 is increased to 3.62 GHz. The result shown in Fig. 3 is helpful in designing a filter with a specific center frequency.

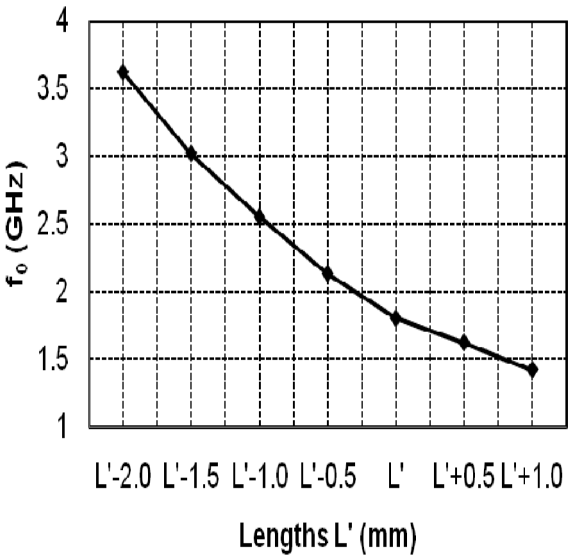

Fig. 3. Resonator resonance frequency (f_0)against its cell size. *L'* represents the lengths *L, L1, L2, L3,* and *L4* of the resonator shown in Fig. 1(c).

III. BANDPASS DGS FILTER

Bandpass filter can be designed by cascading several bandpass resonators and adjusting the coupling between these resonators to achieve a specific bandwidth. The coupling between the resonators is controlled by the strip conductor width *S* separating the two resonators as shown in Fig. 4(a). The effect of the strip thickness *S* on the fractional bandwidth (*FBW*) is shown in Fig. 5. It can be seen that as *S* increases, the bandwidths decreases. In other words, increasing *S* between the two resonators will decrease coupling and so decrease the bandwidth. The *FBW* that can be obtained using this structure is limited from about 13% to 23%. Figure 6 shows the simulated frequency response of two filters designed for *S*=0.1mm and *S*=0.5mm. The structure is simulated using IE3D package. The same dimensions presented in the above section are used in this case (*L* = 10mm, *L1* = 4mm, *L2* = 5.5mm, *L3* = 3.5mm, *L4* = 6mm, *W1* = 2.5mm, *M1* = 0.9mm, and *M2* = 1.6mm).

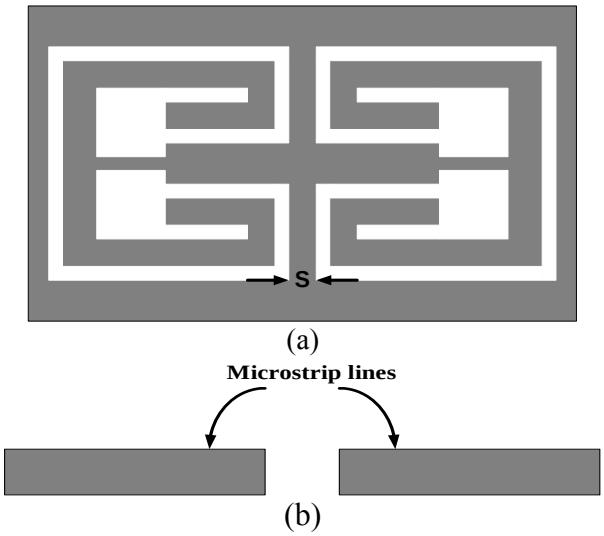

Fig. 4. (a) Schematics of backside of BPF, (b) front side of BPF.

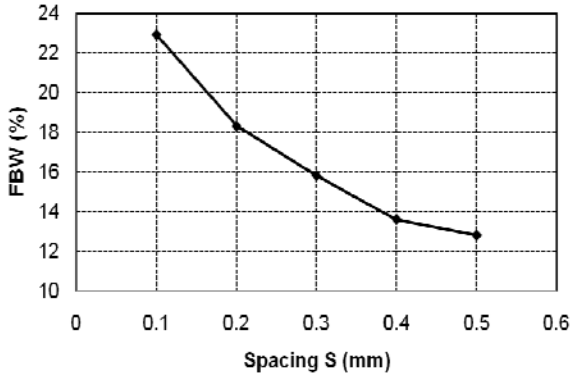

Fig. 5. Computed fractional bandwidths (*FBW*) for different spacing *S*.

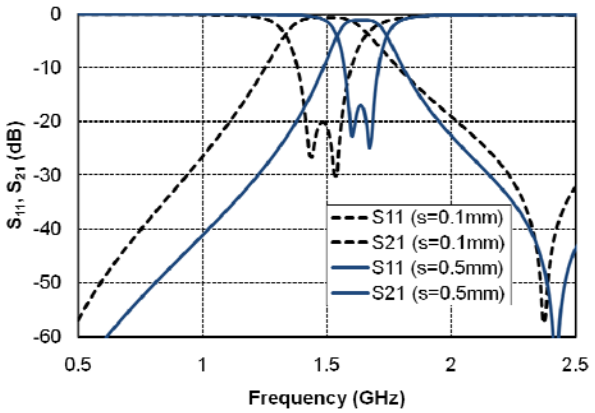

Fig. 6. Simulated frequency responses for different spacing *S*.

The filter with *S*=0.5 mm is fabricated and tested using Anritsu 37396C Network Analyzer. The photographs of the top and bottom sides are shown in Fig. 7. The universal test fixture (Gigalane) is used to allow accurate measurements without soldering. The filter bandwidth is about 210 MHz centered at 1.63 GHz. A little shift in the center frequency with respect to Fig. 3 is observed since the resonator arrangement in Fig. 1(c) is slightly different on that used in the cascading form in Fig. 4 (a).

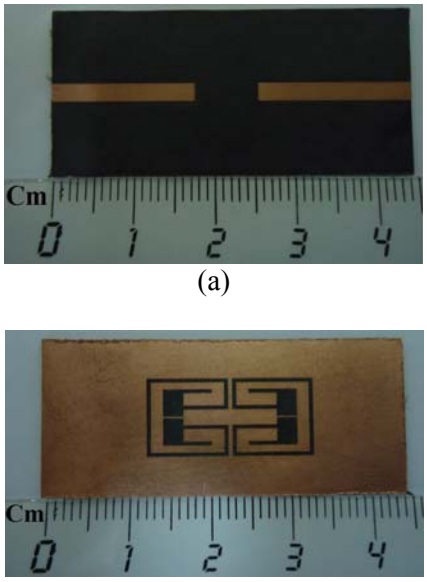

Fig. 7. Photographs of the bandpass filter (a) front side of the filter, (b) back side of the filter.

Figure 8 shows the measured and simulated frequency response of the filter. Very good matching is observed in both simulations and measurements. The simulated and measured insertion losses are 1 dB and 1.4 dB, respectively.

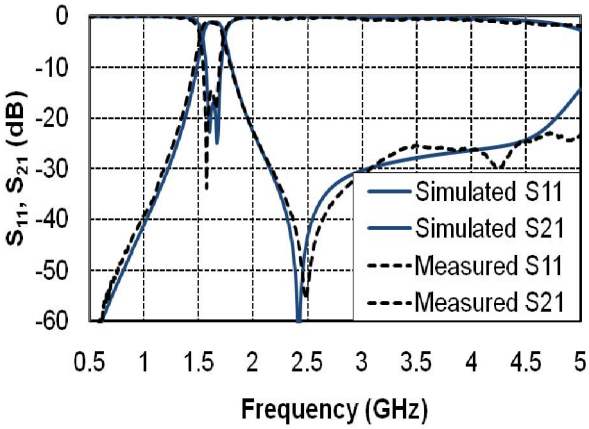

Fig. 8. Simulated and measured results of BPF with space *S*=0.5mm.

A. Effect of slot etched in the coupled conductor strip

As shown in Fig. 5, filter *FBW* from 13% to 23% can be achieved by a coupled conductor strip of width from 0.5 mm to 0.1 mm, respectively. However, narrower bandwidth can be achieved by etching a slot of width *d* in the coupling strip as shown in Fig. 9.

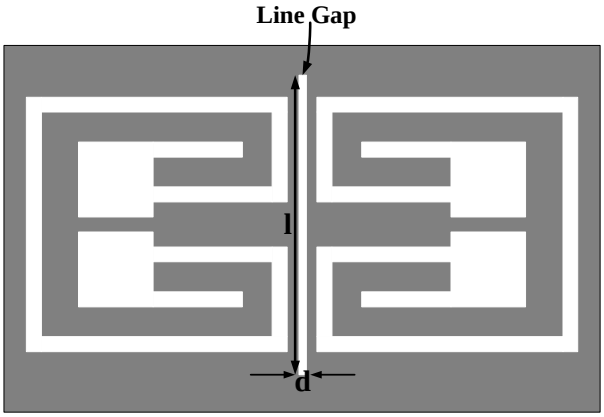

Fig. 9. Schematics of backside of BPF with etched slot of width *d* in the coupled conductor strip.

The strip conductor width is fixed to be 0.5 mm. The effect of the slot width on the *FBW* is shown in Fig. 10. It can be seen that the *FBW* decreases as the slot width increases. *FBW* of about 2.5% can be reached as the slot width *d* =0.4 mm. Figure 11 shows the simulated frequency response of two filters for *d*=0 mm and *d*=0.4 mm. The length *l* of the etched slot is 11mm in all the cases. The same physical dimensions of the resonator discussed in the previous sections are used.

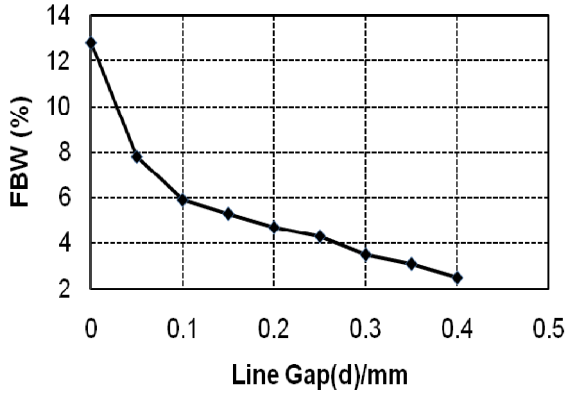

Fig. 10. Computed *FBW* for different slot widths *d*.

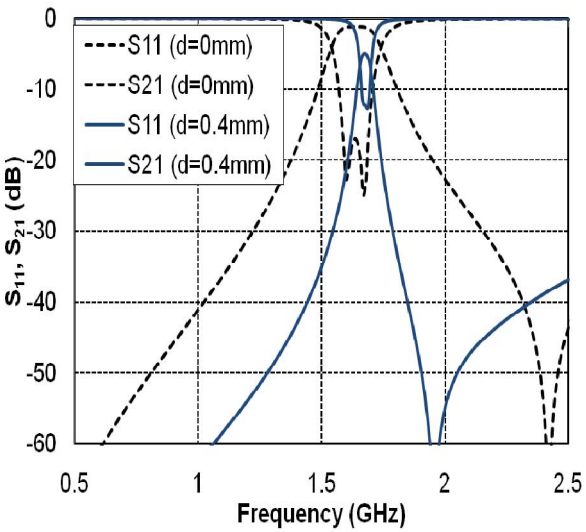

Fig. 11. Simulated frequency responses for different line gap width *d*.

As mentioned in Fig.10, to achieve about 6% *FBW* the slot width *d* should be 0.1mm and length *l* is 11mm. The coupled conductor strip width *S* is 0.5mm. For experimental validation a BPF with *d*=0.1mm, *l*=11mm, and *S*=0.5mm is fabricated and tested. The back-side photograph of the fabricated filter is shown in Fig. 12. The experimental results are compared with the simulations as shown in Fig. 13.

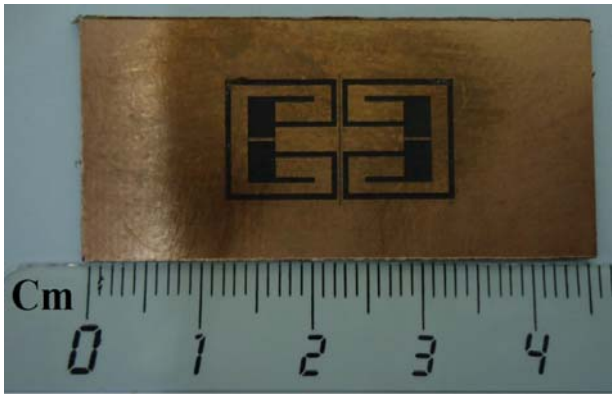

Fig. 12. Photograph of back side of the fabricated bandpass filter (*S*=0.5mm, *d*=0.1mm).

The results of the two fabricated filters with coupled conductor strip width *S*=0.5mm are summarized in Table 1. The measured fractional bandwidths (*FBW*) are 13% for the filter with no etched slot and 6.5% with etched slot of width = 0.1 mm in the conductor strip.

Table 1: Performance of the filters (S=0.5)

	***S*=0.5mm *d*=0mm**	***S*=0.5mm, *d*=0.1mm**
Simulated	12.5 %	6 %
Measured	13 %	6.5 %
Simulated f_o	1.61 GHz	1.67 GHz
Measured f_o	1.63 GHz	1.67 GHz
Simulated Insertion	1.0 dB	2.3 dB
Measured Insertion	1.46 dB	2.1 dB

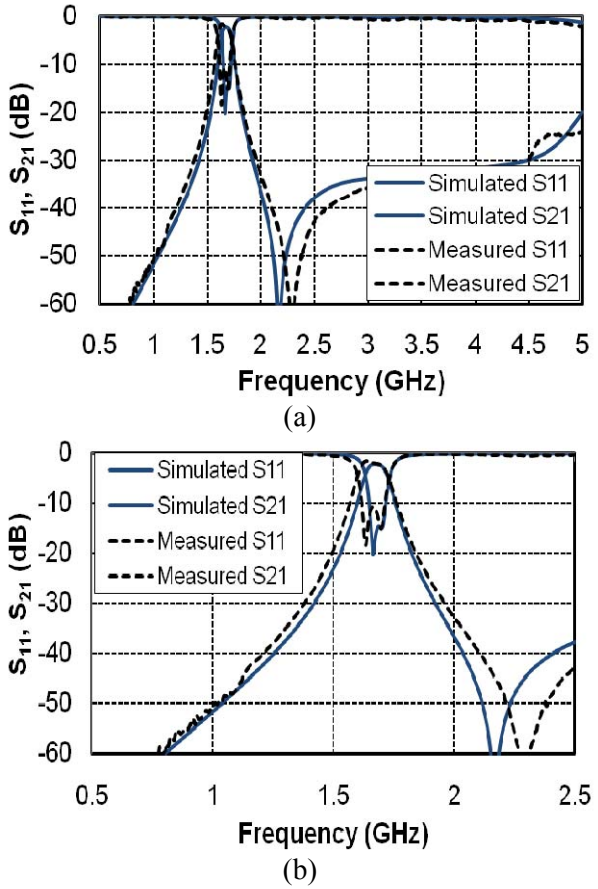

Fig. 13. Simulated and measured results of BPF with slot width d=0.1mm, (a) wide range plot, (b) narrow range plot.

IV. CONCLUSION

New compact DGS resonators are proposed and used to design bandpass filter with fractional bandwidth from about 2.5% to 23%. The DGS resonators are placed back-to-back and coupled with a conductor strip. It has been shown that the width of the strip-conductor controls the filter bandwidth by controlling the coupling between the resonators. Etching a slot in the coupled strip reduces the filter bandwidth more. Two bandpass filters with fractional bandwidth of 6%, and 13% have been designed and fabricated. The simulated and measured results of the proposed bandpass filter exhibit good agreement.

ACKNOWLEDGMENT

This work is supported by the National Plan for Science and Technology Program, Kingdom of Saudi Arabia, Research Grant: 08-ADV210-2.

REFERENCES

[1] L. H. Weng, Y. C. Guo, X. W. Shi, and X. Q. Chen, "An Overview on Defected Ground Structure," *Progress In Electromagnetics Research B (PIER B)*, vol. 7, pp. 173-189, 2008.

[2] F. Karshenas, A. R. Mallahzadeh, and J. Rashed-Mohassel, "Size Reduction and Harmonic Suppression of Parallel Coupled-Line Bandpass Filters Using Defected Ground Structure," *Applied Computational Electromagnetic Society (ACES) Journal*, vol. 25, no. 2, pp. 149-155, Feb. 2010.

[3] M. Al Sharkawy, A. Boutejdar, F. Alhefnawi, and O. Luxor, "Improvement of Compactness of Lowpass/Bandpass Filter using a New Electromagnetic Coupled Crescent Defected Ground Structure Resonators," *Applied Computational Electromagnetic Society (ACES) Journal*, vol. 25, no. 7, pp. 570 – 577, July 2010.

[4] N. M. Garmjani and N. Komjani, "Improved Microstrip Folded Tri-Section Stepped Impedance Resonator Bandpass Filter using Defected Ground Structure," *Applied Computational Electromagnetic Society (ACES) Journal*, vol. 25, no. 11, pp. 975-983, November 2010.

[5] A. Abdel-Rahman, A. R. Ali, S. Amari, and A. S. Omar, "Compact Bandpass Filters using Defected Ground Structure (DGS) Coupled Resonators," *IEEE MTT-S Int. Microwave Symp. Dig.*, pp. 12-17, 2005.

[6] A. R. Ali., A. Abdel-Rahman, S. Amari, and A. S. Omar, "Direct and Cross-Coupled Resonator Filters using Defected Ground Structure (DGS) Resonators," *European Microwave Conference*, vol. 2, pp. 4-6, 2005.

[7] X. H. Wang and B. Z. Wang, "Compact Broadband Dual-Band Bandpass Filters using Slotted Ground Structures," *Progress In Electromagnetics Research (PIER)*, vol. 82, pp. 151-166, 2008.

[8] P. Vagner, and M. Kasal, "Bandpass Filter Design using an Open-Loop Defected Ground Structure Resonator," *15th Int. Conference on Microwave Tech.*, pp. 77-80, 2010.

[9] A. Mohan and A. Biswas, "A Novel Defected Ground Structure (DGS) Resonator for Bandpass Filters Applications," *Asia-Pacific Microwave Conference*, pp. 1-4, 2007.

[10] N. Militaru, G. Lojewski, and M. G. Banciu, "Planar Microwave Bandpass Filters with Defected Ground Resonators," *Int. Semiconductor Conference*, vol. 1, pp. 101-104, 2006.

[11] J. S. Yoon, J. G. Kim, J. S. Park, C. S. Park, J. B. Lim, H. G. Cho, and K. Y. Kang, "A New DGS Resonator and its Application to Bandpass Filter Design," *IEEE MTT-S Int. Microwave Symp. Dig.*, vol. 3, pp. 1605-1608, 2004.

[12] D. Ahn, J. S. Park, C.-S. Kim, J. Kim, Y. Qian, and T. Itoh, "A Design of the Low-Pass Filter using the Novel Microstrip Defected Ground Structure," *IEEE Transactions on Microwave Theory and Tech.*, vol. 49, no. 1, pp. 86-93, Jan 2001.

[13] J. S. Lim, C. S. Kim, Y. T. Lee, D. Ahn, and S. Nam, "A Spiral-Shaped Defected Ground Structure for Coplanar Waveguide," *IEEE Microwave and Wireless Components Letters*, vol. 12, no. 9, pp. 330- 332, Sep 2002.

[14] M. K. Mandal, and S. Sanyal, "A Novel Defected Ground Structure for Planar Circuits," *IEEE Microwave and Wireless Components Letters*, vol. 16, no. 2 , pp. 93-95, Feb. 2006.

[15] A. F. Sheta, "A Novel Compact Degenerate Dual-Mode Square Patch Filter using Cross H-Shaped Defected Ground Structure," *Journal of Electromagnetic Waves and Applications*, vol. 22, pp. 1913-1923, 2008.

Sajjad Ur Rehman graduated from Engineering Dept., Iqra University Pakistan in 2006. He worked as a lecturer at the Iqra University (Peshawar Campus) Electrical Engineering Dept., during 2007-2008. Currently, Engr. Sajjad Ur Rehman is M.Sc. student and research assistant at the Electrical Engineering Department, King Saud University, Saudi Arabia. His research interests include microstrip filters and reconfigurable RF filters.

Abdel Fattah Sheta graduated from the Communications and Electro-Physics Dept., Alexandria University, Egypt in 1985. He received the M.Sc. degree in Electrical Engineering, Cairo University, in 1991. In 1996, he received the Ph.D. degree in Microwave Circuits Analysis and Design from ENST, Université de Bretagne Occidentale, France. During 1996-1998, he worked as a researcher at the National Telecommunication Institute, Cairo, Egypt. In 1998, he joined Electrical Engineering Department, Fayoum University. Currently, Dr. Sheta is a Professor at EE Department, King Saud University, Saudi Arabia. His current research interests include reconfigurable RF systems, UWB systems, microstrip antennas, microstrip filters, and planar and uniplanar MIC's and MMIC's.

Majeed Majeed A. S. Alkanhal received the B.S. and M.S. degrees from King Saud University, Riyadh, Saudi Arabia, in 1984 and 1986, respectively, and the Ph.D. degree from Syracuse University, Syracuse, NY, in 1994, all in Electrical Engineering. He is presently a Professor and Chairman of the Electrical Engineering Department at King Saud University, Riyadh, Saudi Arabia. His research interests are in antennas and propagation, computational electromagnetics, and microwave engineering.

2011 INSTITUTIONAL MEMBERS

DTIC-OCP LIBRARY
8725 John J. Kingman Rd, Ste 0944
Fort Belvoir, VA 22060-6218

AUSTRALIAN DEFENCE LIBRARY
Northcott Drive
Canberra, A.C.T. 2600 Australia

BEIJING BOOK CO, INC
701 E Linden Avenue
Linden, NJ 07036-2495

DARTMOUTH COLLEGE
6025 Baker/Berry Library
Hanover, NH 03755-3560

DSTO EDINBURGH
AU/33851-AP, PO Box 830470
Birmingham, AL 35283

SIMEON J. EARL – BAE SYSTEMS
W432A, Warton Aerodome
Preston, Lancs., UK PR4 1AX

ENGINEERING INFORMATION, INC
PO Box 543
Amsterdam, Netherlands 1000 Am

ETSE TELECOMUNICACION
Biblioteca, Campus Lagoas
Vigo, 36200 Spain

GA INSTITUTE OF TECHNOLOGY
EBS-Lib Mail code 0900
74 Cherry Street
Atlanta, GA 30332

TIMOTHY HOLZHEIMER
Raytheon
PO Box 1044
Rockwall, TX 75087

HRL LABS, RESEARCH LIBRARY
3011 Malibu Canyon
Malibu, CA 90265

IEE INSPEC
Michael Faraday House
6 Hills Way
Stevenage, Herts UK SG1 2AY

INSTITUTE FOR SCIENTIFIC INFO.
Publication Processing Dept.
3501 Market St.
Philadelphia, PA 19104-3302

LIBRARY – DRDC OTTAWA
3701 Carling Avenue
Ottawa, Ontario, Canada K1A OZ4

LIBRARY of CONGRESS
Reg. Of Copyrights
Attn: 407 Deposits
Washington DC, 20559

LINDA HALL LIBRARY
5109 Cherry Street
Kansas City, MO 64110-2498

MISSOURI S&T
400 W 14th Street
Rolla, MO 56409

MIT LINCOLN LABORATORY
Periodicals Library
244 Wood Street
Lexington, MA 02420

NATIONAL CHI NAN UNIVERSITY
Lily Journal & Book Co, Ltd
20920 Glenbrook Drive
Walnut, CA 91789-3809

JOHN NORGARD
UCCS
20340 Pine Shadow Drive
Colorado Springs, CO 80908

OSAMA MOHAMMED
Florida International University
10555 W Flagler Street
Miami, FL 33174

NAVAL POSTGRADUATE SCHOOL
Attn:J. Rozdal/411 Dyer Rd./ Rm 111
Monterey, CA 93943-5101

NDL KAGAKU
C/0 KWE-ACCESS
PO Box 300613 (JFK A/P)
Jamaica, NY 11430-0613

OVIEDO LIBRARY
PO BOX 830679
Birmingham, AL 35283

DAVID PAULSEN
E3Compliance
1523 North Joe Wilson Road
Cedr Hill, TX 75104-1437

PENN STATE UNIVERSITY
126 Paterno Library
University Park, PA 16802-1808

DAVID J. PINION
1122 E Pike Street #1217
SEATTLE, WA 98122

KATHERINE SIAKAVARA
Gymnasiou 8
Thessaloniki, Greece 55236

SWETS INFORMATION SERVICES
160 Ninth Avenue, Suite A
Runnemede, NJ 08078

YUTAKA TANGE
Maizuru Natl College of Technology
234 Shiroya
Maizuru, Kyoto, Japan 625-8511

TIB & UNIV. BIB. HANNOVER
DE/5100/G1/0001
Welfengarten 1B
Hannover, Germany 30167

UEKAE
PO Box 830470
Birmingham, AL 35283

UNIV OF CENTRAL FLORIDA
4000 Central Florida Boulevard
Orlando, FL 32816-8005

UNIVERSITY OF COLORADO
1720 Pleasant Street, 184 UCB
Boulder, CO 80309-0184

UNIVERSITY OF KANSAS – WATSON
1425 Jayhawk Blvd 210S
Lawrence, KS 66045-7594

UNIVERSITY OF MISSISSIPPI
JD Williams Library
University, MS 38677-1848

UNIVERSITY LIBRARY/HKUST
Clear Water Bay Road
Kowloon, Honk Kong

CHUAN CHENG WANG
8F, No. 31, Lane 546
MingCheng 2nd Road, Zuoying Dist
Kaoshiung City, Taiwan 813

THOMAS WEILAND
TU Darmstadt
Schlossgartenstrasse 8
Darmstadt, Hessen, Germany 64289

STEVEN WEISS
US Army Research Lab
2800 Powder Mill Road
Adelphi, MD 20783

YOSHIHIDE YAMADA
NATIONAL DEFENSE ACADEMY
1-10-20 Hashirimizu
Yokosuka, Kanagawa,
Japan 239-8686

APPLIED COMPUTATIONAL ELECTROMAGNETICS SOCIETY JOURNAL
http://aces.ee.olemiss.edu

INFORMATION FOR AUTHORS

PUBLICATION CRITERIA

Each paper is required to manifest some relation to applied computational electromagnetics. **Papers may address general issues in applied computational electromagnetics, or they may focus on specific applications, techniques, codes, or computational issues.** While the following list is not exhaustive, each paper will generally relate to at least one of these areas:

1. **Code validation.** This is done using internal checks or experimental, analytical or other computational data. Measured data of potential utility to code validation efforts will also be considered for publication.

2. **Code performance analysis.** This usually involves identification of numerical accuracy or other limitations, solution convergence, numerical and physical modeling error, and parameter tradeoffs. However, it is also permissible to address issues such as ease-of-use, set-up time, run time, special outputs, or other special features.

3. **Computational studies of basic physics.** This involves using a code, algorithm, or computational technique to simulate reality in such a way that better, or new physical insight or understanding, is achieved.

4. **New computational techniques** or new applications for existing computational techniques or codes.

5. **"Tricks of the trade"** in selecting and applying codes and techniques.

6. **New codes, algorithms, code enhancement, and code fixes.** This category is self-explanatory, but includes significant changes to existing codes, such as applicability extensions, algorithm optimization, problem correction, limitation removal, or other performance improvement. **Note: Code (or algorithm) capability descriptions are not acceptable, unless they contain sufficient technical material to justify consideration.**

7. **Code input/output issues.** This normally involves innovations in input (such as input geometry standardization, automatic mesh generation, or computer-aided design) or in output (whether it be tabular, graphical, statistical, Fourier-transformed, or otherwise signal-processed). Material dealing with input/output database management, output interpretation, or other input/output issues will also be considered for publication.

8. **Computer hardware issues.** This is the category for analysis of hardware capabilities and limitations of various types of electromagnetics computational requirements. Vector and parallel computational techniques and implementation are of particular interest.

Applications of interest include, but are not limited to, antennas (and their electromagnetic environments), networks, static fields, radar cross section, inverse scattering, shielding, radiation hazards, biological effects, biomedical applications, electromagnetic pulse (EMP), electromagnetic interference (EMI), electromagnetic compatibility (EMC), power transmission, charge transport, dielectric, magnetic and nonlinear materials, microwave components, MEMS, RFID, and MMIC technologies, remote sensing and geometrical and physical optics, radar and communications systems, sensors, fiber optics, plasmas, particle accelerators, generators and motors, electromagnetic wave propagation, non-destructive evaluation, eddy currents, and inverse scattering.

Techniques of interest include but not limited to frequency-domain and time-domain techniques, integral equation and differential equation techniques, diffraction theories, physical and geometrical optics, method of moments, finite differences and finite element techniques, transmission line method, modal expansions, perturbation methods, and hybrid methods.

Where possible and appropriate, authors are required to provide statements of quantitative accuracy for measured and/or computed data. This issue is discussed in "Accuracy & Publication: Requiring, quantitative accuracy statements to accompany data," by E. K. Miller, *ACES Newsletter*, Vol. 9, No. 3, pp. 23-29, 1994, ISBN 1056-9170.

SUBMITTAL PROCEDURE

All submissions should be uploaded to ACES server through ACES web site (http://aces.ee.olemiss.edu) by using the upload button, journal section. Only pdf files are accepted for submission. The file size should not be larger than 5MB, otherwise permission from the Editor-in-Chief should be obtained first. Automated acknowledgment of the electronic submission, after the upload process is successfully completed, will be sent to the corresponding author only. It is the responsibility of the corresponding author to keep the remaining authors, if applicable, informed. Email submission is not accepted and will not be processed.

EDITORIAL REVIEW

In order to ensure an appropriate level of quality control, papers are peer reviewed. They are reviewed both for technical correctness and for adherence to the listed guidelines regarding information content and format.

PAPER FORMAT

Only camera-ready electronic files are accepted for publication. The term **"camera-ready" means that the material is neat, legible, reproducible, and in accordance with the final version format listed below.**

The following requirements are in effect for the final version of an ACES Journal paper:

1. The paper title should not be placed on a separate page.

The title, author(s), abstract, and (space permitting) beginning of the paper itself should all be on the first page. The title, author(s), and author affiliations should be centered (center-justified) on the first page. The title should be of font size 16 and bolded, the author names should be of font size 12 and bolded, and the author affiliation should be of font size 12 (regular font, neither italic nor bolded).

2. An abstract is required. The abstract should be a brief summary of the work described in the paper. It should state the computer codes, computational techniques, and applications discussed in the paper (as applicable) and should otherwise be usable by technical abstracting and indexing services. The word "Abstract" has to be placed at the left margin of the paper, and should be bolded and italic. It also should be followed by a hyphen (—) with the main text of the abstract starting on the same line.

3. All section titles have to be centered and all the title letters should be written in caps. The section titles need to be numbered using roman numbering (I. II. ….)

4. Either British English or American English spellings may be used, provided that each word is spelled consistently throughout the paper.

5. Internal consistency of references format should be maintained. As a guideline for authors, we recommend that references be given using numerical numbering in the body of the paper (with numerical listing of all references at the end of the paper). The first letter of the authors' first name should be listed followed by a period, which in turn, followed by the authors' complete last name. Use a coma (,) to separate between the authors' names. Titles of papers or articles should be in quotation marks (" "), followed by the title of journal, which should be in italic font. The journal volume (vol.), issue number (no.), page numbering (pp.), month and year of publication should come after the journal title in the sequence listed here.

6. Internal consistency shall also be maintained for other elements of style, such as equation numbering. Equation numbers should be placed in parentheses at the right column margin. All symbols in any equation have to be defined before the equation appears or right immediately following the equation.

7. The use of SI units is strongly encouraged. English units may be used as secondary units (in parentheses).

8. Figures and tables should be formatted appropriately (centered within the column, side-by-side, etc.) on the page such that the presented data appears close to and after it is being referenced in the text. When including figures and tables, all care should be taken so that they will appear appropriately when printed in black and white. For better visibility of paper on computer screen, it is good to make color figures with different line styles for figures with multiple curves. Colors should also be tested to insure their ability to be distinguished after black and white printing. Avoid the use of large symbols with curves in a figure. It is always better to use different line styles such as solid, dotted, dashed, etc.

9. A figure caption should be located directly beneath the corresponding figure, and should be fully justified.

10. The intent and meaning of all text must be clear. For authors who are not masters of the English language, the ACES Editorial Staff will provide assistance with grammar (subject to clarity of intent and meaning). However, this may delay the scheduled publication date.

11. Unused space should be minimized. Sections and subsections should not normally begin on a new page.

ACES reserves the right to edit any uploaded material, however, this is not generally done. It is the author(s) responsibility to provide acceptable camera-ready files in pdf and MSWord formats. Incompatible or incomplete files will not be processed for publication, and authors will be requested to re-upload a revised acceptable version.

COPYRIGHTS AND RELEASES

Each primary author must execute the online copyright form and obtain a release from his/her organization vesting the copyright with ACES. Both the author(s) and affiliated organization(s) are allowed to use the copyrighted material freely for their own private purposes.

Permission is granted to quote short passages and reproduce figures and tables from and ACES Journal issue provided the source is cited. Copies of ACES Journal articles may be made in accordance with usage permitted by Sections 107 or 108 of the U.S. Copyright Law. This consent does not extend to other kinds of copying, such as for general distribution, for advertising or promotional purposes, for creating new collective works, or for resale. The reproduction of multiple copies and the use of articles or extracts for commercial purposes require the consent of the author and specific permission from ACES. Institutional members are allowed to copy any ACES Journal issue for their internal distribution only.

PUBLICATION CHARGES

All authors are allowed for 8 printed pages per paper without charge. Mandatory page charges of $75 a page apply to all pages in excess of 8 printed pages. Authors are entitled to one, free of charge, copy of the printed journal issue in which their paper was published. Additional reprints are available for $ 50. Requests for additional re-prints should be submitted to the managing editor or ACES Secretary.

Corresponding author is required to complete the online form for the over page charge payment right after the initial acceptance of the paper is conveyed to the corresponding author by email.

ACES Journal is abstracted in INSPEC, in Engineering Index, DTIC, Science Citation Index Expanded, the Research Alert, and to Current Contents/Engineering, Computing & Technology.